Charged Particle Lithography for the Fabrication of Nanostructured Optical Elements

Ranveig Flatabø

Avhandling for graden philosophiae doctor (ph.d.)
Universitetet i Bergen
2018

UNIVERSITETET I BERGEN

Charged Particle Lithography for the Fabrication of Nanostructured Optical Elements

Ranveig Flatabø

Avhandling for graden philosophiae doctor (ph.d.)
ved Universitetet i Bergen

2018

Dato for disputas: 31.08.2018

År: 2018

Tittel: Charged Particle Lithography for the Fabrication of Nanostructured Optical Elements

Navn: Ranveig Flatabø

Trykk: Skipnes Kommunikasjon / Universitetet i Bergen

Acknowledgements

First and foremost, I would like to thank my supervisors Bodil Holst and Martin M. Greve – for your guidance and motivating words, for your belief in me, for providing me with the greatest amount of freedom in my research and for always keeping your door open for questions and discussions. The list can go on, as one cannot ask for a better supervisor team! I would also like to thank the rest of the Nanophysics group: Sabrina for being a good friend and being able to fix any instrument in a heartbeat, Bjørn for sharing extraordinary knowledge on instrumentation and life, Vårin for being a great office mate, Justas, Naureen, Arivuu and Matina you all made the Nanophysics group a fun, productive and good workplace. I also acknowledge the great work of the master students I co-supervised: Håkon, Erik and Håvard.

I was lucky to be able to exchange to the quantum nanostructure and nanofabrication group (QNN) at Massachusetts Institute of Technology (MIT). First, I would like to express my sincere gratitude to Karl K. Berggren for welcoming me in his group. Thank you for sharing your intellectual curiosity, your philosophy on how to organize a lab-book, and for truly making me feel like a part of QNN. I aslo thank Hank I. Smith for sharing his knowledge on focusing via diffraction and for his open and friendly nature. Thanks to Emily and Navid for your friendship and for keeping me grounded, and thanks to the rest of the Muddy-group. I also acknowledge everyone that worked at QNN during my time at MIT, thank you for all the help and advice. I would like to thank Jim Daley, Mark Mondol and Tim Savas for their exceptional expertise in instrumentation and nanofabrication. Thanks to Lewis Stern, David Ferranti and Fouzia Khanom for introducing me to neon ion beam fabrication and for fruitful discussions through my multiple visits at Zeiss, Ion Microscopy group in Peabody, Boston.

This work was made possible through the generous support of Bergen Research Foundation [1]. I express my gratitude to the Norway-America Association and the American-Scandinavian Foundation's The Stolt-Nilsen Fund for Education for awarding me with a scholarship for my stay at MIT.

Last but not least, to my family and friends; you are a source with brightness higher than any described in this thesis - thank you.

[1] https://www.bfstiftelse.no/

List of papers

I **R. Flatabø**, A. Agarwal, R. Hobbs, M.M Greve, B. Holst and K.K Berggren, Exploring proximity effects and large depth of field in helium ion beam lithography: large-area dense patterns and tilted surface exposure, *Nanotechnology*, **29**, 275301 (7 pp), (2018)

II **R. Flatabø**, A Coste and M.M Greve, A systematic investigation of the charging effect in scanning electron microscopy for metal nanostructures on insulating substrates, *Journal of Microscopy*, **265**, 287-297, (2017)

III **R. Flatabø**, V.R.A Holm, H. Eidsvåg, B. Holst and M.M Greve, Light absorption and scattering of 40-170 nm gold nanoparticles on glass substrates, *Journal of Vacuum Science & Technology B, Nanotechnology and Microelectronics: Materials, Processing, Measurement and Phenomena*, **35**, 06G403 (5 pp), (2017)

IV **R. Flatabø**, M.M Greve, S.D Eder, M. Kalläne, A. Salvador Palau, K.K Berggren and B. Holst, Atom sieve for nanometer resolution neutral helium microscopy, *Journal of Vacuum Science & Technology B, Nanotechnology and Microelectronics: Materials, Processing, Measurement and Phenomena*, **35**, 06G502 (6 pp), (2017)

V **R. Flatabø**, S.D Eder, A.K Ravn, B. Samelin, M.M Greve, T. Reisinger and B. Holst, Fast resolution change in neutral helium atom microscopy, *Review of Scientific Instruments*, **89**, 053702 (4 pp), (2018), Shared first authorship with S.D Eder, **Selected as editor's choice**

Author contribution statement

- **Paper I**: The thesis defender is the first author. She designed the experiment, fabricated the gratings and wrote the manuscript under the guidance of Holst and Berggren. Agarwal contributed with the calculation of the depth of field based on helium ion beam images. Hobbs and Greve contributed with discussion and Hobbs did the initial teaching on how to use the instrument.

- **Paper II**: The thesis defender is the first author. She designed the experiment, fabricated the nanostructures, performed the measurements and wrote the manuscript under the guidance of Greve. Coste is included as author because he did preliminary experiments on the effect.

- **Paper III**: The thesis defender is first author. She fabricated two of the arrays; the rest were fabricated by Eidsvåg under the daily supervision of the thesis defender. The thesis defender did most of the optical measurements and data analysis. Holm wrote the theoretical part of the manuscript and the thesis defender wrote the remainder of the manuscript, under the guidance of Holst and Greve.

- **Paper IV**: The thesis defender is the first author. She fabricated the atom sieve in the laboratory of Berggren who contributed with discussion. The thesis defender wrote the manuscript under the guidance of Holst and Greve. Eder tested the transmissivity of the atom sieve in the helium microscope; Palau calculated the optimum system geometry and on the basis of this Kalläne calculated the sieve design.

- **Paper V**: Shared first authorship with Eder. The thesis defender fabricated the apertures and wrote the manuscript together with Eder, supervised by Holst and Greve. Reisinger is included as author because he made the zoneplate used in the experiments. Ravn performed preliminary simulations. Samelin has built the helium microscope instrument together with Eder.

List of Presentations

1. *Helium ion beam lithography*, Oral presentation, June 12 - 14 2017, 8th annual workshop for Norwegian PhD Network on Nanotechnology for Microsystems, Bergen, Norway

2. *Large-area scanning helium ion beam lithography*, Oral presentation, May 30 – June 2 2017, The 61st International conference on electron, ion, photon beam technology and nanofabrication (EIPBN), Orlando, Florida, USA

3. *Atomsieve for nanometer resolution neutral helium microscopy*, Oral presentation, May 30 – June 2 2017, The 61st International conference on electron, ion, photon beam technology and nanofabrication (EIPBN), Orlando, Florida, USA

4. *A systematic investigation of charging effects in scanning electron microscopy for metal nanostructures on insulating substrates*, Poster presentation, May 31 – June 3 2016, The 60th International conference on electron, ion, photon beam technology and nanofabrication (EIPBN), Pittsburgh, Pennsylvania, USA

5. *Charging effects in metal nanoparticles on insulating substrates*, Oral presentation, June 15-17 2015, 6th annual workshop for Norwegian PhD Network on Nanotechnology for Microsystems, Oslo, Norway. **Awarded best student talk**

6. *Optical properties of metal nanoparticles studied using an integrating sphere set-up*, Poster presentation, October 13-14 2014, NorTeX Nano Summit, Rice University, Houston, Texas, USA

Abstract

This thesis work focuses on nanostructured optical elements for light and matter waves that have been fabricated using helium ion beam lithography and electron beam lithography. The motivation of this thesis has been to develop new optical elements and to contribute with foundational work to instrumentation and characterization of nanostructures. The work has been carried out at the University of Bergen, Nanostructure Laboratory and at the Massachusetts Institute of Technology, Nanostructure Laboratory.

The thesis is based on five papers published in international, peer reviewed, Web of science journals. The thesis defender is sole first author on paper I-IV and shared first author on paper V. Paper I presents the first helium ion beam lithography patterning on a non-horizontal surface. Such patterning is possible because of the large field of depth in a helium ion beam instrument. Comparable writing cannot be performed with standard electron beam lithography. Patterning on curved or tilted surfaces is potentially very useful in a range of devices e.g. optical lenses, and is fundamentally an attractive property. Paper II presents a systematic scanning-electron-microscopy study of the charging effect in metal nanostructures on insulating surfaces. Negative charging is found to induce a measurement error in the measured dimensions of the nanostructures comparable to a de-magnified image. In paper III, the optical response of metal nanoparticles mediated by the localized surface plasmon resonance effect are studied using integrating spheres, and the influence of the fabrication method on the optical properties is discussed. Paper IV and V describe optical elements for matter waves. In Paper IV a high-transmission atom sieve for focusing neutral helium atoms is fabricated, showing that focusing below 10 nm should in principle be possible. Paper V demonstrates fast resolution change in the focusing neutral helium microscope by inserting collimating apertures. Without changing the properties of the neutral helium beam and without breaking the vacuum a resolution change by a factor of 4.4 is demonstrated.

Contents

Part I

Overview and summary

Chapter 1

Introduction

1.1 Thesis structure

This thesis is divided into three parts. Part 1 “Overview and Summary” consists of 3 chapters. Chapter 1 introduces the thesis work and summarizes and connects the results presented in the five published papers. Instruments, fabrication procedures and characterization techniques are discussed in Chapter 2. Part 1 finishes with a conclusion and outlook (Chapter 3). Part 2 comprises the papers that have been published during this thesis work. Finally, Part 3 contains the appendices. Unless explicitly mentioned all images in this thesis were made by the thesis defender.

1.2 Motivation and background

Nanofabrication is the manufacturing of structures with at least one dimension on the nanoscale (1 nm = 1×10^{-9} m) [1]. One may ask, why pursue nanofabrication? This is a question with many answers. Firstly, reducing the dimension of functional structures towards or to the nanoscale increases the density of the device. This is manifested in the scaling of integrated circuits described by Moore’s law [2]. Secondly, nanofabrication enables the study and exploitation of physical and chemical phenomena that occurs when material dimensions reach the nanoscale [3]. For example, the catalytic activity of a material can change completely on the nanoscale [4]. Another prominent example of behavior change on the nanoscale, which is of particular importance for this thesis work is the change in optical properties. The optical response of metal nanostructures are related to the size and shape of the structures as well as to the surrounding environment [5].

Nanofabrication can be categorized into two paradigms; bottom-up and top-down. Bottom-up processes use individual particles (such as atoms or molecules) as building blocks to form functional structures [1], e.g. sol-gel synthesis, atomic vapor deposition and self-assembly. In a sol-gel synthesis, the particles are typically suspended in a liquid (the *sol*) and acts as pre-

cursors to form a three dimensional network structure (the *gel*). Using metal alkoxides as precursors, metal oxide nanoparticles are often synthesized by the sol-gel process [6]. In atomic layer deposition, films with thickness control at the Ångström (monolayer) level are deposited onto a surface. A precursor reacts with and saturates the surface, depositing a monolayer onto it. If multiple precursors are used, the precursors react with the surface in a sequential manner, separated by a purging or evacuation step [7]. Self-assembly is the organization of components into a structure or pattern. It is typically considered to be spontaneous and reversible, and can be divided into three categories, static -, dynamic -, and templated self-assembly. The formation of molecular crystals is an example of static self-assembly. In static self-assembly the structures are in an (local) energy minimum ((quasi) equilibrium). Dynamic self-assembly rely on the dissipation of energy as this allows the interactions responsible for pattern formation to occur [8]. Finally, an example of templated self-assembly is one that employs top-down and bottom-up techniques. The template consists of posts written using electron beam lithography. These posts control a subsequent self-assembly and guide the structures into an energy-favorable design [9].

In top-down processes bulk materials are broken down to nanostructures [1]. It is largely dominated by nanolithography, where a pattern is written in a serial fashion on a substrate (serial lithography) or transferred to the substrate via a mask (mask lithography). The substrate is typically, but not always, coated with a thin-film called resist that changes chemically upon exposure. Exposure can be done using photons (visible light, UV – EUV light, X-rays), neutral atoms, electrons and ions [10]. Additionally, mechanical probes such as an atomic force microscopy (AFM) tip can be used to pattern a surface. In the so-called dip-pen lithography in positive printing mode, the AFM-tip is coated with specific molecules, which are transferred to the substrate via capillary action [11].

Mask lithography allows for instant exposure, but it is limited by the lack of pattern design flexibility. The trend in optical lithography, often considered the key to the age of micro- and nano-based semiconductor devices, has been to expose using shorter wavelengths of radiation (13.5 nm for EUV, and less than 1 nm for X-rays) to improve the diffraction-limited pattern resolution [12]. In nanoimprint lithography a pre-fabricated mask is imprinted in a resist which is later cured by heat or light. The pattern resolution is in principle limited by the mask (or put in other words the ability to fabricate the mask) [10], and as an example 4-nm half-pitch gratings have been realized in a UV-curable resist [13]. In atom lithography, the table is somewhat turned as light fields typically acts as a mask. Atoms can be deposited onto the surface by using a so-called light force mask that changes the atom flux by a spatially varying force. Alternatively, excited atoms (metastable) can expose resists. In this case, the pattern is determined by an absorptive light mask that optically force atoms to their ground state [14]. Finally, solid masks approximating binary holographs have been used to manipulate atom beams and create arbitrary patterns in the far-field regime [15]. It has recently been shown that by moving to the near-field regime it should be possible to make also nm-resolution pattern

with this method [16].

In serial lithography, electron beam lithography (EBL) is considered to be the work horse and is generally the method of choice for high-resolution mask-fabrication. The pattern is written in a resist using a focused probe of electrons and isolated dots with a diameter of 1.7 nm has been written in a conventional resist (negative-tone PMMA) [17], and structures with a half-pitch of 4.5 nm have been fabricated (in HSQ) [18]. Serial lithography with light ions (helium or neon) is an emerging fabrication technique, and neon ion beam lithography has demonstrated 7 nm lines with 14 nm pitch [19].

1.2.1 Thesis Objectives

The objective of this thesis has been to explore state of the art charged particle lithography to develop new optical elements for light and matter waves. The main focus has been on the fabrication of (a) metal nanoparticles as plasmonic structures, (b) nanostructured optical elements (atom sieves and collimating apertures) for neutral helium microscopy and c) nano-gratings for future generation of Smith-Purcell radiation. In all cases, a well-functioning device requires accurate fabrication. To ensure this, precise characterization is crucial. Precise characterization of metal nanostructures on insulating substrates (particular relevant for (a)) is a major challenge and paper II has been dedicated to this theme. Finally, as a general contribution to instrumental development, the thesis presents the first experiment demonstrating resist-based helium ion lithography on a tilted surface, an aspect that is important for a large range of devices.

This work has been carried out at the University of Bergen, Nanostructure Laboratory (paper II, III and V) and at the Massachusetts Institute of Technology, Nanostructure Laboratory (paper I and IV). The thesis is based on five published papers, all of which have been published in peer-reviewed journals accessible through the Web of Science or PubMed. The thesis defender is first author on all of the published papers (shared first-authorship in paper V).

1.3 Summary of the published papers

1.3.1 Paper I: Exploring proximity effects and large depth of field in helium ion beam lithography: large-area dense patterns and tilted surface exposure

Helium ion beam lithography (HIL), described in greater detail in Chapter 2, benefits from a reduced interaction volume to that of an electron beam of similar energy. Figure 1.1 shows the trajectories of (a) 30 keV electrons and (b) 30 keV helium ions into silicon. The calculations are done using the free software Casino (electrons) [20] and SRIM (helium ions) [21].

For lithography purposes, the effective results of a reduced interaction volume are a reduction in unwanted exposure (proximity effects), higher resist sensitivity and possibly higher resolution [22, 23].

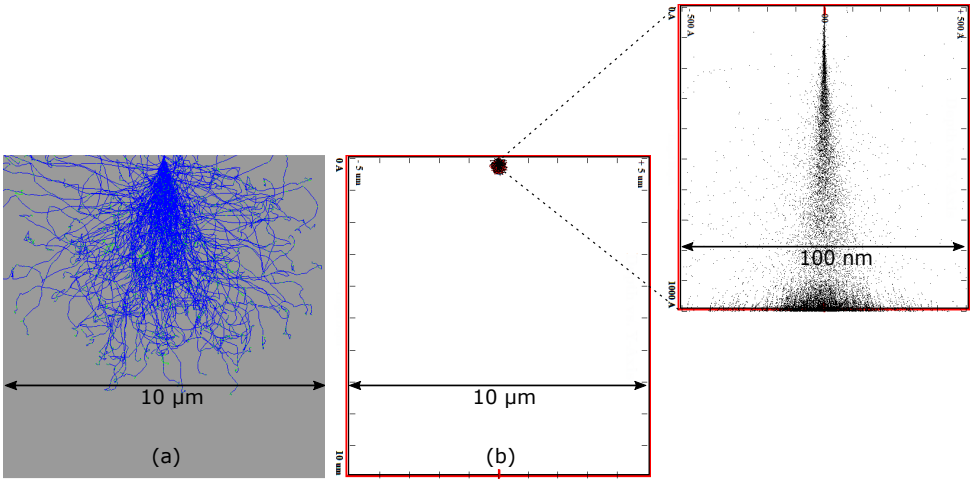

Figure 1.1: (a) Electron and (b) helium ion beam trajectories into silicon. 1000 helium ions/electrons enters the material, and as can be seen the total interaction volume of the helium ions is much smaller than the interaction volume of the electron beam. Also note the narrow helium ion beam profile for depths smaller than 50 nm, shown in the inset of figure (b).

High-resolution helium ion beam microscopy is becoming a well-established technique [24, 25, 26], as is high-resolution milling with helium ions [25, 27, 28]. So far the work done on resist-based helium ion beam lithography has been focused on reaching sub-10 nm resolution, and hence has mostly been single-pixel exposures over small areas, see e.g. [29, 13, 22, 23].

The short wavelength and the small angular spread of the helium ion beam gives rise to a large depth of field. Depth of field is defined as the region above and below the focus plane where the beam is acceptably sharp, and depends upon the aperture, the working distance and in the case of HIL the spot control number (the spot control number dictates the position of the beam crossover above the aperture). The large depth of field has been demonstrated in helium ion beam images [24, 30], but has not been exploited in lithography before this thesis work. It should enable patterning on tilted and curved surfaces without the need for any additional instrument adjustments, such as the use of laser auto focus in EBL. This is of relevance for the patterning of e.g. optical fibers and lenses [31], and a fundamentally attractive property as it provides a large focus tolerance.

In paper I, two new areas of application in HIL are studied. Firstly, the reduced proximity effects are demonstrated and large area grating are patterned using an area dose (see Chapter 2 for a more detailed description of dose). An area-dose exposure (in units of: $\mu C/cm^2$ or ions/nm^2) requires in theory less dose than a single-pixel exposure (in units of: pC/cm or

ions/nm), because in a single-pixel exposure much of the dose is wasted in overexposing the pixel. Here, the design consists of 16 nm wide lines patterned using a 2 nm pixel size and exposure areas up to 100 μm × 100 μm with pitches down to 35 nm. A helium ion beam image of the 40 nm-pitch grating is shown in Figure 1.2. Secondly, 100 μm long lines are patterned while having the sample stage tilted 45 degrees to exploit the large depth of field and demonstrate for the first time helium ion beam lithography on a non-horizontal surface. The depth of field scales with the working distance i.e. the larger the working distance, the larger the depth of field (due to decrease of the angular spread of the beam). Therefore, the beam was focused at a working distance of (a) $\sim$ 15 mm and (b) $\sim$ 27 mm. An increase in working distance is equivalent to an increase in spot size. To accommodate this, single-pixel lines were exposed with an increased pixel size (8 nm for 15 mm working distance and 10 nm for 27 mm working distance). Variation in linewidth, or the lack of variation, serves as an estimation of the depth of field. The grating shown in Figure 1.3(a)-(c) is written using a working distance of $\sim$ 15 mm. The variation in linewidth along the first 50 μm indicates that the depth of field is smaller than 50 μm for this resolution. Figure 1.3 (d)-(f) shows SEM images of the grating written at a working distance of $\sim$ 27 mm. In this case, the width of the single pixel line is found to be 26 $\pm$ 1.5 nm, which demonstrates that the depth of field at this resolution is at least 100 μm. This illustrates HIL's potential to pattern on tilted and curved surfaces. Zhang et al. estimated that the depth of field of an electron beam is on the order of 10 μm [32], and hence the length scale presented here would be hard to realize using an EBL without a dynamic focus correction.

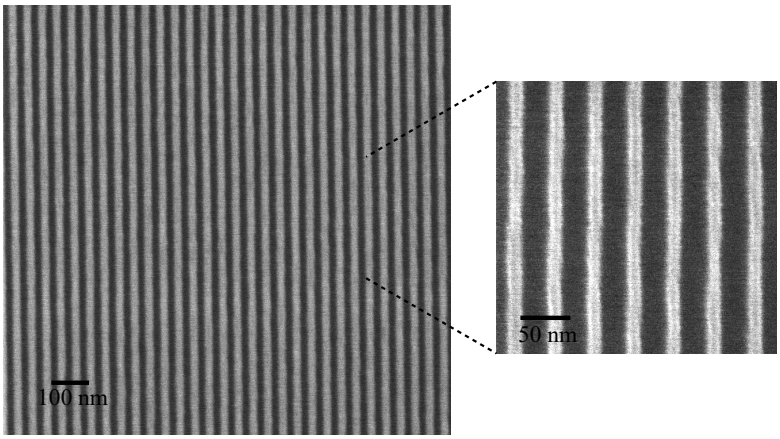

Figure 1.2: HIM image of HSQ grating patterning using HIL. The lines are defined as rectangles with a width of 16 nm and a length 50 μm. The measured width was 17 $\pm$ 1 nm, and the pitch was 40 $\pm$ 1 nm.

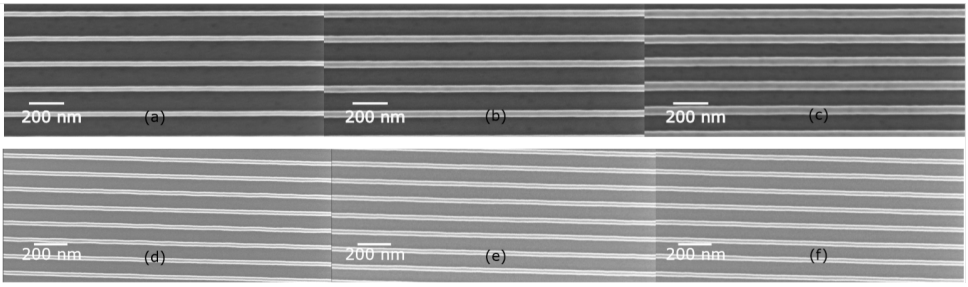

Figure 1.3: (a)-(f) SEM images along the diagonal of the 100 μm HSQ grating, written while having the sample stage tilted 45 °. In (a)-(c) the working distance was 15 mm. (a) Lower left sample area, line width 26 nm. (b) Middle sample are 39 nm. (c) Upper right sample area, line width 52 nm. The working distance used in (d)-(f) was 27 mm. (d) Lower left sample area (e) middle sample area (f) upper sample area. The width of the lines remains the same across the patterned area, 26 ± 1.5 nm, and hence the depht of field for this resolution is at least 100 μm [33].

Smith-Purcell Radiation

Though not discussed in the paper, a main motivation of this work was to make gratings that can be used for the generation of Smith-Purcell radiation [34]. Although Smith-Purcell radiation was not actually produced as part of this thesis work, a brief introduction is included here. A beam of electrons that elongate parallel to a periodic structure can generate electromagnetic radiation, so-called Smith-Purcell radiation. The basic principle behind Smith-Purcell radiation is illustrated in Figure 1.4. The electron is incident parallel to, and at a height b above the grating with periodicity p. The charges at the surface arrange themselves to screen the electric field of the moving electron. The screening charges follow the grating topography and appear to accelerate from a peak to a groove in the grating, and this acceleration results in the emission of light with a wavelength λ_{SP}. Based on a Huygens construction, the wavelength of the Smith-Purcell radiation can, according to the notation in Figure 1.4, be written as [34]:

$$\lambda_{SP} = \frac{p}{m}\left(\frac{1}{\beta} - \cos\theta\right) \tag{1.1}$$

where $\beta = v/c$ in which v is the speed of the electron beam and c is the speed of light and p is the grating pitch. λ_{SP} can thus be tuned by varying the electron velocity and/or the pitch of the periodic structure. Radiation ranging from the far-infrared to the mm regime has been generated using large-pitch gratings and low-energy electron beams [35, 36]. Advances in nanofabrication techniques have enabled the fabrication of Smith-Purcell sources in the visible and UV-regime [37, 38]. Traditionally, the electron beam energy has been increased to reach shorter wavelength of radiation. For example, Smith and Purcell [34] used a 1.67 μm pitch grating and an electron beam with a speed of 0.8 of the speed of light to excite visible light. However, as seen in Equation 1.1 shorter wavelengths of radiation can also be reached by

decreasing the pitch of the grating. The goal of this work was to produce light spanning from the visible to the UV regime powered by a standard electron microscope beam. Based on Equation 1.1, at normal emission (the light is to be collected by an objective with a numerical aperture of 0.3, as described by Massuda et al. [39]) a 10 keV electron beam ($\beta \sim 0.2$) will produce λ_{SP} = 200 nm in the 40 nm-pitch grating.

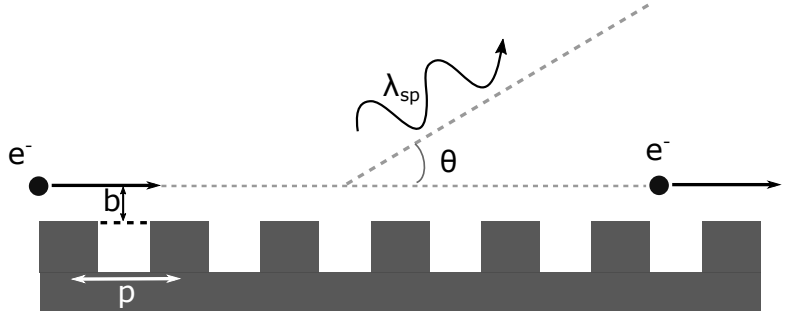

Figure 1.4: The basic principle of the generation of Smith-Purcell radiation. An eletron beam passes the surface of the grating with pitch p at a height b above the surface, generating radiation with a wavelength λ_{SP}, with an angle θ relative to the surface.

1.3.2 Paper II: A systematic investigation of the charging effect in scanning electron microscopy for metal nanostructures on insulating substrates

Reliable characterization of nanostructures by the means of microscopy is of key importance in order to make functional devices, as the physical and chemical properties of nanostructures may depend upon particle size, shape and surrounding environment. Moreover, characterization is crucial for a nanofabrication process, as the way to success is often careful optimization of correlated sub-procedures. Among others, atomic force microscopy (AFM), transmission electron microscopy (TEM) and scanning electron microscopy (SEM) can be used to characterize nanostructures. Whereas AFM uses a physical probe to scan the surface, TEM and SEM use a beam of high-energy electrons (typically greater than 50 keV for a TEM and smaller than 30 keV for an SEM) to look at transmitted or reflected signals, respectively [40]. SEM is possibly the main method of characterization due to the microscope resolution, simplicity in operation, image quality and promptness of the microscope [41].

A well-known challenge in SEM is the characterization of insulating (non-conductive) materials, see e.g [42, 43, 44]. An SEM image is generated by raster-scanning the beam across the sample. The incident electrons interact with the sample and generate signals that can be detected e.g. backscattered electrons, characteristic or continuum X-rays, Auger electrons, cathodoluminescence and secondary electrons (SEs). Out of these, SEs are widely used for imaging. SEs are generated via inelastic interactions and generally have energies below 50 eV.

They are detected either by an InLens detector that collects secondaries generated within the sample (i.e. SE1 and SE2) or by an Everhart-Thornely detector that, when positively biased, additionally collects SEs generated in the chamber (i.e. SE3) [41].

The charging in insulating materials in SEM causes magnification variations, image drift and abnormal contrast [45], and qualitatively it can be described as follows: a fraction of the incident electrons are trapped in the material which generates a surface potential. This potential can change the energy and trajectory of the subsequent incident electrons in two ways. A negative potential will repell and de-accelerate the incident electrons, decreasing the penetration depth of the beam. A positive potential will attract and accelerate the incident electrons, increasing the penetration depth of the beam. As a result a negative potential will increase the number of secondary electrons generated, and vice versa for a positive potential. The trapped incident electrons are responsible for negative charging, while the emission of SEs causes positive charging. Charge balance is achieved when the arrival of one incident electron is accompanied by the emission of another electron (either as a SE or a backscattered electron). As shown in Figure 1.5, there are two cross-over energies where charge-balance can be reached. E_1 is usually in the range between 50 and 200 eV and hence not reachable in conventional SEMs. E_2 on the other hand is located in the range 500 eV – a couple of keV, suitable for SEM-imaging [43].

In paper II, we systematically investigate gold nanostructures on a glass substrate. Specifically, we find that the measured dimensions of the structures appear smaller than the dimensions measured in a conductive environment and using an AFM. The measurement error is caused by the build-up of negative charge in the sample and is comparable to a de-magnified image. We study the measurement error as a function of various microscope settings, and find it to depend on acceleration voltage and secondary-electron detector used for imaging. It is found to be independent of the scan-direction of the electron beam, working distance and the probe current at a given acceleration voltage. Additionally, we find that it should in principle be possible to fit three normalized measurements to a single exponential function to estimate the (second) cross-over where charge balance is reached, thus extracting the true sample dimensions.

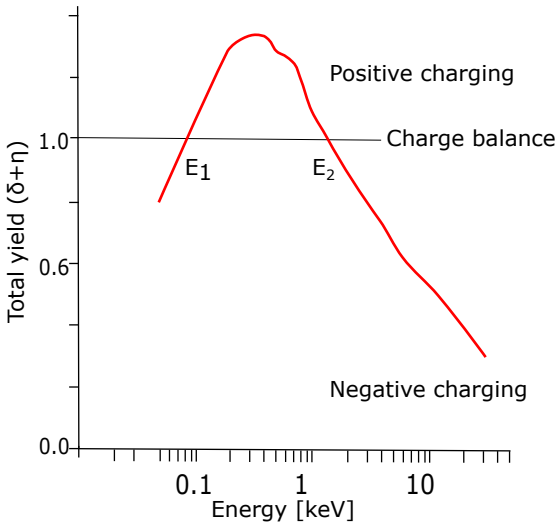

Figure 1.5: The total emitted electron yield from a non-conductive material versus incoming electron beam energy. Charge balance is obatined at two cross-over energies, E_1 and E_2. The figure is redrawn from [43] and presented in [46].

1.3.3 Paper III: Optical elements for light waves - nanoplasmonics

Sub-wavelength optics

Nanoplasmonics is the study of the interaction of light and metal nanostructures, mediated by the collective oscillation of conduction electrons in the nanostructures. Nanoplasmonics makes it possible to confine light into volumes smaller than about half of the wavelength of light; the classical diffraction limit. This opens a wide range of applications in e.g. optical sensing, photovoltaics and cancer therapy [47, 48, 49].

The metal nanoparticle can in its simplest form be described as an oscillator, see Figure 1.6. A collective displacement of the conduction electrons relative to the ion core is induced when light couples to the nanoparticle. This generates a restoring force. A state of resonance arises when the frequency of light matches the eigenfrequency of the oscillator, known as the localized surface plasmon resonance (LSPR). The LSPR wavelength (frequency) of the nanoparticle depends on the constituent metal, the size and shape of the structure, as well as on the surrounding medium. The resonant response of the metal nanostructures can be described by different approaches. The simplest is Rayleigh scattering, an approach that is valid when the structure is much smaller than the wavelength of incoming light. Within this limit, the electric field is spatially static over the nanostructure, and the nanostructure is described as an ideal dipole. At resonance, the well-known Fröhlich condition expresses the LSPR-dependency on

the surrounding medium [50]:

$$\mathrm{Re}[\varepsilon(\omega)] = -2\varepsilon_m \tag{1.2}$$

where $\varepsilon(\omega)$ is the dielectric function of the metal and ε_m the dielectric constant of the surrounding medium. Assuming that the metal nanoparticle is a Drude metal with negligible damping and has the shape of a sphere, the resonance frequency is reached when $\omega = \frac{\omega_p}{\sqrt{(3)}}$ in air. By placing this sphere in glass ($\varepsilon_m \sim \sqrt{1.5}$) , the Fröhlich condition is met at $\omega = \frac{\omega_p}{2}$. Hence, increasing the dielectric constant (or the refractive index) of the surrounding medium redshifts the spectral position of the LSPR [50].

The electrostatic approach breaks down when the size of the nanostructure gets comparable to the wavelength of the electric field, so that retardation effects need to be included. Mie theory is a complete analytical theory of the scattering and absorption of light by an arbitrary sized sphere. Retardation effects indicates the existence of higher order resonances, and indeed as the nanostructure size increases, higher order resonances becomes more important, and the oscillations of the electrons can no longer be described as one collective motion. Moreover, Mie theory predicts a redshift when the particle size increases, which in the simple picture of an oscillator is caused by a smaller restoring force [50, 51].

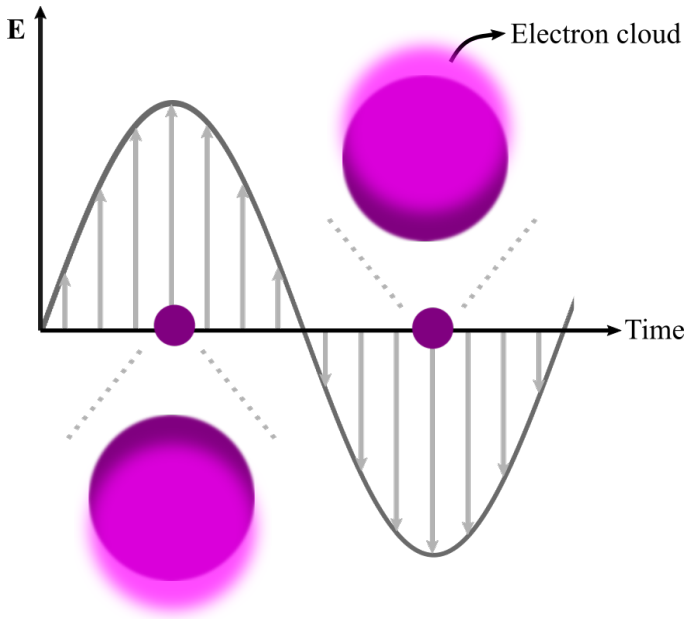

Figure 1.6: Illustration of a spherical nanoparticle in an electric field (light). The electric field displaces the electron cloud.

Paper III: Light absorption and scattering of 40 - 170 nm gold nanoparticles on glass substrates

In paper III we study light absorption and scattering in large periodic arrays (3 mm $\times$ 3 mm) of gold nanostructures on glass substrates. The diameters of particles range from 39 ± 4 nm to 167 ± 5 nm, and their height is 25 ± 1 nm. The arrays were fabricated by the means of EBL followed by metal deposition and a lift-off procedure. The gold was deposited directly on the glass substrate, which has been assumed challenging due to the poor adhesion [52]. However, possibly due to the fact that nanoparticles can release strain more easily than a film and the assumed roughness of the glass substrate, the gold particles adhered well to the glass substrate [53]. The optical response is measured using integrating spheres. An integrating sphere is a spherical cavity coated with an ideal diffusely reflecting surface (a Lambertian surface), and the sample (i.e. gold nanoparticles and glass substrate) and glass reflectance and transmittance can be extracted from the raw data, see Figure 1.7. The integrating spheres are described in greater detail in Chapter 2. The portion of light being extinct (i.e. removed from the directly transmitted beam) by the particles are found using an extinction measurement set-up. As the light scattered in all spatial directions is collected in an integrating sphere, it is possible to find the light absorbed by the nanoparticle once their extinction spectra is known. The scattering Q_{sca}- and absorption efficiencies Q_{abs} of the nanoparticle arrays are defined as [51]

$$Q_{sca} = S_{NP}/(N\pi(d/2)^2) \tag{1.3}$$

$$Q_{abs} = A_{NP}/(N\pi(d/2)^2) \tag{1.4}$$

where N is the normalized unit cell coverage, and $\pi(d/2)^2$ the cross-sectional area of the disk-shaped nanoparticle where d is the diameter. The efficiencies are dimension-less numbers and because metal nanoparticles absorb/scatter more light than expected from their geometrical cross-sections they can exceed unity.

The scattering and absorption efficiencies are tuned by controlling the shape and size of the gold nanostructures and/or array geometry, and are hence largely determined by the method of fabrication. An integrating sphere set-up requires a large-area sample and has, to the best of our knowledge, not been used to study the optical response of metal nanoparticles fabricated using EBL prior to this thesis work. The optical response of our EBL-fabricated samples are compared to that of Langhammer et al. [54], where a similar set-up was used but the samples were fabricated by the means of hole-mask colloidal lithography (HCL). In HCL, a thin polymer film and a charged polyelectrolyte (an adhesion layer) is deposited onto the sample surface, followed by the deposition of colloidal polystyrene beads. The polystyrene beads and the polyelectrolyte are charged oppositely, and the attraction between the two alongside with the repulsion between the neighboring colloids defines a pattern of short-range order. An oxygen-resistant etch mask is then evaporated onto the surface and the polystyrene beads are

removed, leaving nano-holes in a plasma-resistant film, the so-called hole-mask. To create gold nano-discs, the underlying polymer film is removed in an oxygen etch, finalized by metal deposition and lift-off. The pitch and the shape are determined by the colloidal particles. The size distribution is found to be less than 5 % for colloids with average diameters greater than 100 nm, and about 10 % for smaller colloids [55]. The EBL and HCL fabricated samples show similar optical response taken into account the small difference in particle parameters and their size distribution. The spectral position of the LSPR fits well with the simulations done using the software Lumerical.

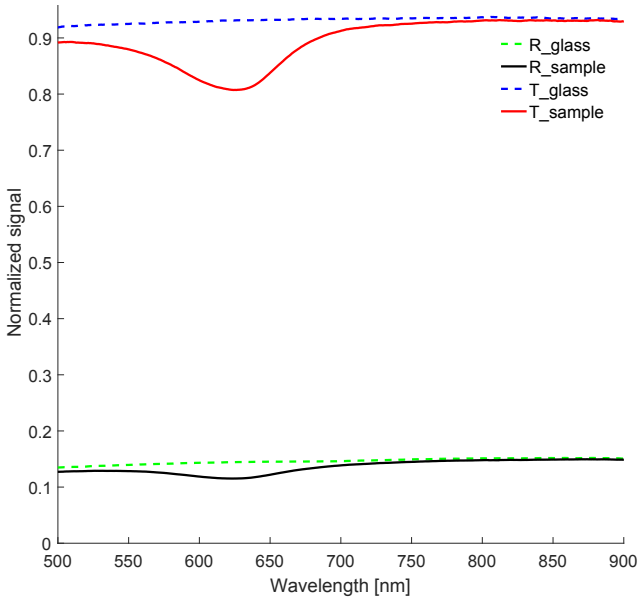

Figure 1.7: Normalized reflectance and transmittance for sample and glass. The sample is an gold nanoparticle array with average diameter of 80 nm and a particle pitch of 400 nm (sample E in Paper III) [56]).

The EBL-fabricated arrays were made such that the particle-pitch was equal to or greater than three times the particle diameter to avoid near-field coupling. That being said, for increasing particle pitches (and hence increasing particle diameters), diffraction effects should become increasingly evident. At a certain pitch (or grating constant) the scattered light fields from neighboring nanoparticles almost constructive interfere, and this has been shown to change the spectral position of the LSPR and its amplitude in extinction [57, 58]. In the EBL fabricated samples, we see a splitting of the spectral position of the LSPR for the scattering efficiency and the absorption efficiency for increasing particle pitches, which could be caused by diffraction effects. This splitting is not observed in the hole-mask colloidal lithography fabricated samples, possibly due to the lack of long-range order [54].

1.3.4 Paper IV and V: Optical elements for matter waves

The Neutral Helium Microcsope

The neutral helium microscope (NeMi), housed at the University of Bergen, is a focusing microscope where a beam of neutral helium atoms are scanned across the sample surface. Ground state helium is inert and has a very low polarizability and no permanent magnetic moment (and hence are the images not readily affected by magnetic or electric stray fields). Additionally, the helium atoms have a very low energy compared to other particle probes, such as the electron and the photon, as illustrated in Figure 1.8. Hence, neutral helium microscopy is strictly a surface technique that maps the outermost electron density distribution of the sample being imaged [59, 60].

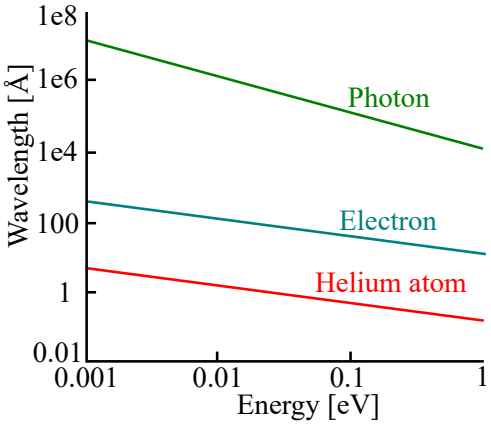

Figure 1.8: (Non-relativistic) energy versus wavelength for common probes used in microscopy. Note the small energy of the helium atom, less than 0.1 eV for a wavelength of about 1 Å.

The basic principle behind NeMi is illustrated in Figure 1.9(a). The neutral helium beam expands from a high pressure gas reservoir through a small aperture nozzle intro high-vacuum conditions (i.e. a free-jet expansion or a supersonic source). A set of apertures collimated the beam, before it meets the focusing element, i.e. the zone plate or the atom sieve. The microscope can be used in transmission (shadow) mode for porous samples, and in reflection mode, quite similar to an SEM [59]. Note that in a helium atom microscope in reflection mode, the signal is generated by the backscattered atoms and there are no enhancement at edges such as is the case for SEM. Hence, in principle helium atom microscopy has the potential to become a very precise metrology instrument. Figure 1.9(b) shows the first image ever taken with a neutral helium beam; a shadow image of a copper TEM grid [61]. This particular image was taken using a predecessor of the present instrument [59]. It should be noted that another configuration also exists, where simply the two apertures (the skimmer and a pinhole) collimates

the beam onto the sample surface. Recently, using such a pinhole microscope chemical contrast coming from inelastic effects was demonstrated [62]. Research on contrast mechanisms is ongoing.

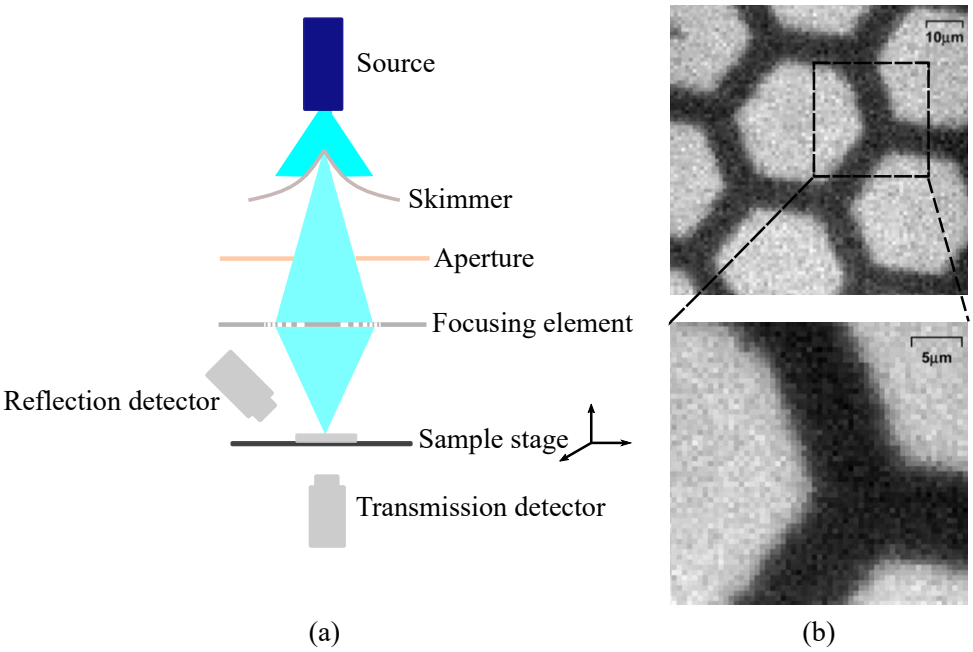

Figure 1.9: (a) Shematic of the main components of NeMi. The instrument can work in reflection mode similar to a scanning electron microscope or for porous samples in transmission mode to obtain shadow images. The figure is redrawn from Ref. [59]. (b) Neutral helium atom image of a copper TEM grid obtained in transmission mode (shadow image). This is the first 2D image obtained with a neutral helium beam and is taken using a predecesssor of the current instrument. The figure is reproduced with premission from [61].

Paper IV: Atom sieve for nanometer resolution neutral helium microscopy

One typically considers two different routes to focus a beam. Option one is to use magnetic or electric fields, while option two is based on exploiting the wave nature of the beam using techniques analogous to classical optics. As mentioned above, ground state helium has a very weak polarization coefficient and no permanent magnetic moment, and thus has to be focused via its wave nature [63]. As such, one is again left with two options; either to use a mirror or to focus via diffraction. Mirrors have been used to focus atoms [64]. They rely on specular scattering and hence do not suffer from chromatic aberrations, but there are some signal loss through diffraction and scattering from defects. Unfortunately for matter waves, up till now, it has been challenging to control the curvature of mirrors with high enough precision to achieve

a highly focused beam [64, 65, 66] and in NeMi the beam is thus focused by diffraction optics [67, 68].

A Fresnel zone plate is a circular diffraction grating consisting of rings with decreasing widths for increasing radii. The construction of this diffractive element is based on the concept of Fresnel zones. Basically, a monochromatic spherical wave emitted from a point source can be divided into a series of circular regions separated by $\lambda/2$ centered at the point P, see Figure 1.10. Radiation from adjacent zones will destructively interfere, and by blocking every other zone the irradiance at P will be increased [69].

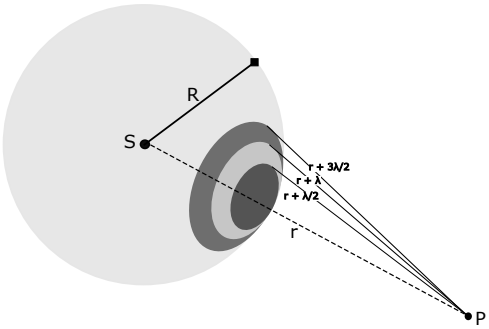

Figure 1.10: Illustration of the propagation of spherical wavefronts separated by $\lambda/2$. The figure is redrawn from [69].

In a zone plate the various diffraction orders creates different focal points with different diffraction efficiency, see Fig 1.11(a). The diffraction efficiency can be written as

$$\eta_m = \frac{I_m}{I_{total}} = \left(\frac{\sin(\frac{a}{d} m\pi)}{m\pi} \right)^2 \tag{1.5}$$

where m is the diffraction order, and $\frac{a}{d}$ the ratio of transparent zones to that of opaque zones. An opening area of 50% corresponds to a design where half of the zones are opaque and half of the zones are transparent. In this case, the zero-order beam takes up 25% of the incident intensity, while the $\pm$ 1 each get about 10.1% each. Only 1.1 % goes to $\pm$ 3 [70]. In NeMi, the first-order beam is focused onto the sample, while the overlapping zero-order beam is blocked by removing the innermost zones of the zone plate and including an order-sorting aperture behind the focusing element [71].

The focusing properties of the zone plate is approximated to that of a thin refractive lens, given that the number of zones, $N > 100$ [70]. In this case, the focal length of the first order focus, f is given by

$$\frac{1}{f} = \frac{1}{g} + \frac{1}{b} = \frac{N\lambda}{r_N^2} \tag{1.6}$$

where g is the object distance, b is the image distance (or working distance), r_N the radius of

the zone plate. The resolution δ of the zone plate based on the Rayleigh criterion is given by

$$\delta = 1.22 d_{rN} \tag{1.7}$$

where d_{rN} is the width of the outermost zone. It should be noted that higher orders of diffraction will increase the resolution by a factor $\frac{1}{m}$, although with reduced intensity. This ultimate resoluiton neglects chromatic aberrations due to the energy spread of the beam [72].

The helium atom do not penetrate solid materials (their typical energy in NeMi is less than 0.1 eV for a de Broglie wavelength of about 0.1 nm), and hence the Fresnel zone plate has to be a free-standing, suspended structure (i.e. binary) as illustrated in Figure 1.11(b). This imposes certain fabrication challenges. An attractive alternative is the Fresnel photon sieve, where pinholes are distributed along the Fresnel zones. Holes are easier to fabricate than free-standing rings aligned to the underlying support structure. Kipp et al. [73] used a photon sieve to focus X-rays to a spot smaller than the smallest pinhole. Focusing below the smallest pinhole is possible because the resolution is limited by the underlying Fresnel zone, which was smaller than the smallest pinhole. The pinholes in the original design were distributed randomly across the Fresnel zones to reduce the efficiency of higher orders, although this limits the intensity in the first order fucus. In 2015, the Nanophysics group at the University of Bergen fabricated and tested the very first atom sieve, and focused helium atoms to a few μm (the smallest hole was 150 nm) [74] with a design similar to that of the original photon sieve.

In paper IV, we designed an atom sieve with holes distributed along the Fresnel zones with a fixed gap to increase the transmitted signal (opening ratio 22.6 %). Based on Equation 1.5, the diffraction efficiency of the first order focus is 4.57 %. The smallest hole is 35 nm, and the ultimate resolution is given by Equation 1.7. The atom sieve was fabricated using EBL and reactive ion etching. The correct dose was found by iteration, see Figure 1.12, and in the final design it was increased linearly from the innermost to the outermost zones. A functional atom sieve relies on successful pattern transfer, which was found to cause additional broadening of the holes. This fact made numerical optimization of the design challenging, and therefore the process was optimized by iteration. A potential one-step fabrication procedure using neon ion beam milling is discussed in Appendix A. An SEM image of the (free-standing) atom sieve is also shown in Figure 1.12. In addition, smaller holes with a diameter down to 15 nm were fabricated in a separate experiment. Here the holes were randomly distributed showing that a sub-10 nm spot size in principle should be possible.

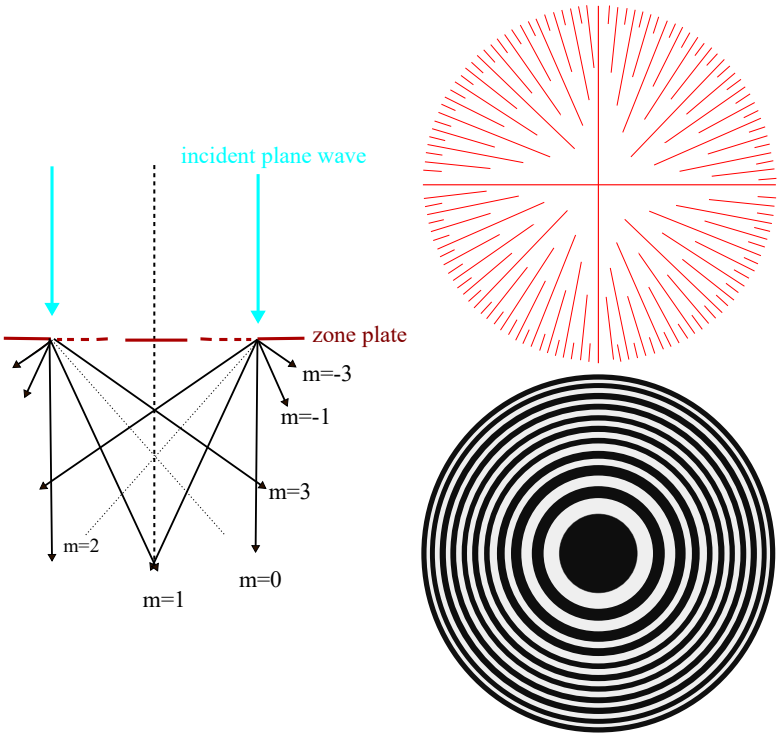

Figure 1.11: Left panel: Illstratation of the various diffraction orders when a plane wave interacts with a zone plate. Right panel: Illustration of the support structure and zone plate currently used to focus the neutral helium beam. The figures are redrawn from [75].

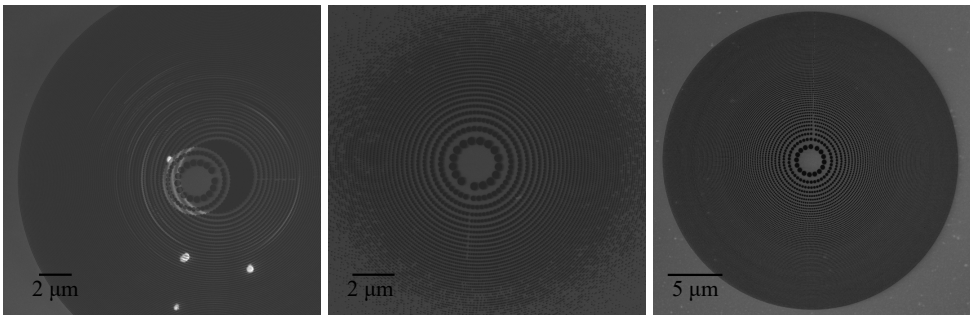

Figure 1.12: SEM images of atom sieves. Iterative exposures of atom sieves with a single exposure dose followed by reactive ion etching was used to find the correct dose. Hence, all atom sieves are free-standing. In the left image the innermost zones are over-exposed/over-etched, while in the middle image the outer-most zones are under-exposed and do not receive enough dose to print. The final atom sieve is shown to the right were the dose was increased linearly from the innermost to the outermost zones. The innermost hole is 377 nm $\pm$ 3 nm and outermost hole is 38 $\pm$ 4 nm.

Paper V: Fast resolution change in neutral helium atom microscopy

Being able to perform a fast change of resolution in a microscope is an attractive property, as this allows different aspects and features of the sample to be investigated. In NeMi the resolution can in principle be changed by changing the temperature of the beam, thereby changing the de Broglie wavelength and hence the focal length of the focusing element. However, by changing the wavelength of the helium atoms, the fundamental properties of the beam is changed, which could affect e.g. image contrast. Furthermore, it is a slow procedure, because the beam needs to stabilize at the new temperature. In paper V we present a solution to this. We show that inserting collimating apertures of various diameters in the neutral helium microscope allows us to perform fast resolution changes in the microscope. Effectively, this is done by changing the source size and hence the spot size on the sample. The experimental set-up is shown in Figure 1.13(a). The collimating aperture is placed as close as possible (28 $\pm$ 1 mm) to the skimmer to maximize the beam flow and avoid any reduction in intensity due to backscattering. Note that the design also include an order-sorting aperture that filters out the zero-order beam, as well as many higher orders of diffraction [71]. This basic design idea allows for a resolution change without breaking the vacuum. Figure 1.13(b) shows the scan results of a 10 μm slit over the varying spot diameters form different collimating apertures (10 μm, 20 μm and 50 μm). The spot sizes were found by fitting an error function to the presented data, and a resolution change by a factor of 4.4 was demonstrated.

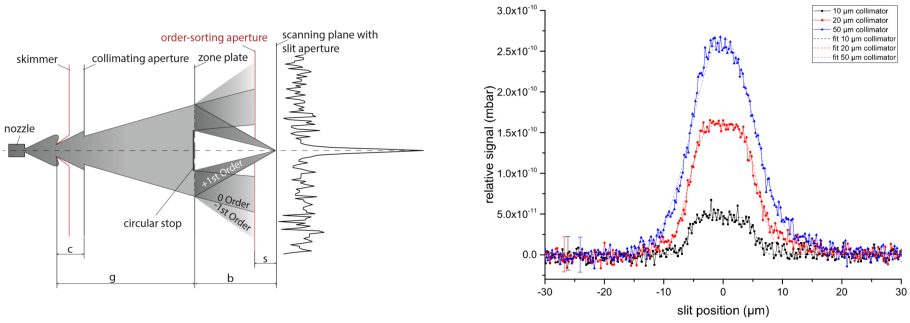

(a) (b)

Figure 1.13: (a) Illustration of the experimental set-up. The central part of the beam is selected by a 120 µm skimmer. The movable collimating apertures are placed as close as possible to the skimmer. The beam is focused onto the sample using a zone plate and an order-sorting aperture removes the zero-order part of the beam (and most of the higher orders). The focal spot is determined by scanning a 10 µm slit across the focal plane. (b) Line scans of the 10 µm slit over the different spot sizes originating from the various collimating apertures and associated error function fits. 50 μm aperture is represented as a blue line, 20 µm aperture shown in red, and finally 10 µm is the black line [76]

Chapter 2

Methods: Fabrication and Characterization

This chapter gives an introduction to the instruments and techniques used for fabricating the devices of this thesis work. Fabrication procedures are further discussed in the appendices.

2.1 Resist-based-lithography with charged particles

As mentioned in Chapter 1, in charged particle lithography a focused beam is scanned across a surface coated with a resist that change chemically upon exposure. In a positive resist, the exposed regions become more soluble (chain-scissoring) in a developer solution. In a negative resist, the exposed regions harden (cross-link), and the non-exposed regions are removed by the developer. The change induced in the resist, and hence the pattern resolution depends upon the properties of the exposing beam and the properties of the resist. The spatial distribution of energy loss by the beam in the resist, the so-called point spread function is the beam property of interest. Scattering in the resist and substrate is divided into three classes; forward scattering (scattering angle < 90 °), backscattering (scattering angle > 90 °) and the generation of secondary electrons [77]. The latter are typically considered being responsible for the resist exposure, and because their path length is short, they do not significantly contribute to proximity effects. The point spread function is typically modelled as a sum of Gaussian distributions, one attributed to the forward scattering of electrons and one describing the backscattering contribution. It should be noted, however, that only accounting for forward scattering and backscattering has been shown inadequate [78], and an accurate description of the point spread function is crucial for proximity effects corrections and hence for realizing high-density, high-resolution features [79]. The resist property of interest is the contrast, that is, the sensitivity of the resist in the developer solution relative to the beam dwell time at each pixel. A high-contrast resist produces features with nearly vertical sidewalls, whereas a low-contrast resist generates sloped-edge features. The beam dwell time relates to the dose as follows:

$$\text{Area dose}\,[\mu\text{C/cm}^2] = \frac{\text{Dwell time} \times \text{Beam current}}{(\text{Step size})^2} \tag{2.1}$$

$$\text{Line dose}\,[\text{pC/cm}] = \frac{\text{Dwell time} \times \text{Beam current}}{\text{Step size}} \tag{2.2}$$

$$\text{Dot dose}\,[\text{pC}] = \text{Dwell time} \times \text{Beam current} \tag{2.3}$$

The dwell time is typically in the micron - millisecond range and its lower limit is set by the clock-rate of the pattern generator. The beam current can vary from sub-1 pA to hundreds of nA. The minimum step size (or pixel size) is also determined by the pattern generator, and will be discussed in greater detail below. The optimum dose is typically found by iteration through the fabrication of dose matrices, an example is given in Figure 2.1.

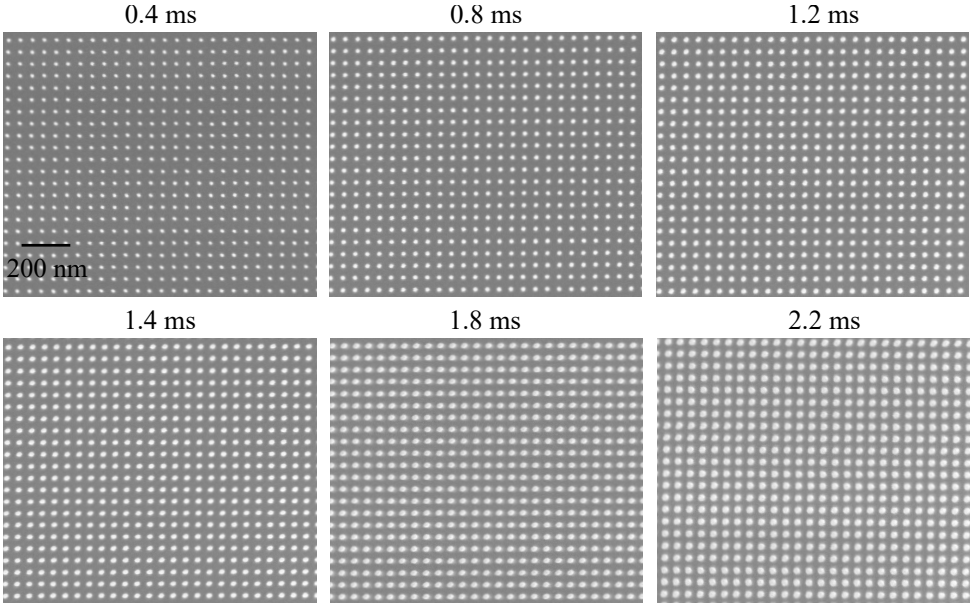

Figure 2.1: SEM images of dose matrices. The images are taken with 3 keV electrons, a 30 μm aperture and a working distance of 4.9 mm. The dot exposure is done in 30 nm HSQ using 30 keV helium ions, a beam current of 1 pA and a dwell time of 0.4 ms i.e. 0.4 fC ($\sim$ 2500 ions) to 2.2 ms i.e. 2.2 fC ($\sim$ 13750 ions). Note that 0.4 ms does not correspond to the dose-to-print in HSQ. However, for dwell times < 0.4 ms, the array was dominated by pattern collapse, likely due to the large aspect ratio. The smallest average diameter is 12 nm, while the largest is 26 nm (pitch = 50 nm in all cases).

In this thesis work two different high-resolution, high-contrast resists are used; poly(methyl methracrylate) (PMMA, 950 K) and hydrogen silsesquioxane (HSQ) [80, 81]. PMMA can be both a positive and a negative resist depending on the delivered dose, while HSQ is a negative resist. Isolated dots with a diameter of 1.7 nm has been produced in negative-tone PMMA, and pitches down to 10.7 nm has been realized [17]. This was done using an aberration corrected scanning transmission electron beam microscope for lithography, and is to this date the

smallest feature made using a conventional resist, and the densest pattern realized in PMMA. A similar tool achieved 2 nm isolated dots and 5 nm half-pitch in HSQ [79].

The (positive-tone) PMMA was developed in 1:3 MIBK:IPA (methyl 2-methylpropyl ketone:2-propanol) at room temperature for 1.5 minutes, rinsed with IPA and dried using pressurized nitrogen. Cold development of PMMA at zero degrees Celsius with a development time of 30 seconds was also used. Specifically, cold development was used to develop the atom sieve pattern presented in paper IV. This was done because cold development has been found to improve feature quality and resolution [82, 83]. Conventionally, HSQ is developed in 25 % wt tetramethyl ammonium hydroxide (TMAH). However, in this thesis work salty development consisting of 1 % wt NaOH (sodium hydroxide) and 4 % NaCl (sodium chloride) was used, which has been demonstrated to improve the contrast by a factor of three [81]. The sample was immersed in the salty developer for 4 minutes at room temperature, and then rinsed in deionized water for 1.5 minutes. Finally, the sample was rinsed in IPA and dried using pressurized nitrogen.

2.1.1 Electron beam lithography

The Raith e_Line at the Nanostructure laboratory at the University of Bergen is a low-voltage EBL tool ($\leq$ 30 kV). It is in principle an SEM (Gemini column (Zeiss)) to which a beam blanker, a high-precision sample stage with piezo-table movement and laser-interferometric position control, and a pattern generator has been added. The beam blanker electrostatically deflects the beam onto a beam stop with high speed, allowing precise dose control. The pattern generator translates the computer-aided-design (CAD)-file into deflection signals, and hence controls the beam blanker. The pattern generator operates with a clock-rate of 20 MHz, and is a 16-bit system. Large patterns are written by stitching together smaller fields via controlled stage movements. This is done because among others, deflecting the beam off-axis by large angles introduces additional aberrations. Hence, only the sub-fields, called write-fields, are written by beam deflection. The size of a write-field determines the minimum pixel size that can be addressed. For a 16-bit pattern generator and a 100 μm $\times$ 100 μm write-field the minimum pixel size is 2 nm (i.e. $\frac{100\mu m}{2^{16}}$). An alternative mode of patterning is fixed-beam-moving-stage where the beam remains stationary while the stage moves.

The Gemini column is equipped with a Schottky thermal field emitter. Electrons are extracted from the source by applying a high electric field allowing the electrons to overcome the potential barrier of the metal and escape into the vacuum through a tunneling effect. In a thermal field emitter this occurs at elevated temperatures, and by coating the metal, typically tungsten with zirconium dioxide, the potential barrier at the tungsten-tip surface is reduced. Such a Schottky thermal field emitter has a lower brightness than the cold field emission source (2 $\times$ 10^8 A/cm^{2}sr at 1800 K, 25 kV versus 5 $\times$ 10^8 A/cm^{2}sr - 1 $\times$ 10^9 A/cm^{2}sr at 25 kV [84]). However, because the emission current from the cold field emitter varies rapidly with time and

thermal field emitters produce a stable beam current, the latter is used in EBL tools. The beam current is controlled by the acceleration voltage and by the apertures of which there are six with diameters in the range 7.5 µm - 120 µm. There are two secondary electron detectors, an InLens detector and an Everthart Thornley detector, installed. As mentioned in Chapter 1, paper II is dedicated to the investigation of non-conductive materials in SEM. One important difference between the two detectors, in addition to the various SE-signals they detect, is their location in the chamber. The Everthart Thornley detector is located at an angle relative to the column and hence due to shadowing topological information can be extracted.

The Elionix at MIT is a 125 kV dedicated EBL tool with a 20 bit pattern generator (and hence have a higher pixel resolution than the Raith e_Line). It is also equipped with a Schottky thermal field emitter and produces beam currents in the range 5 pA to 100 nA. A higher energy electron beam penetrates deeper into the sample (i.e. resist and substrate), see Figure 2.2. At higher energies forward scattering is reduced within the resist, and hence as is the undercut profile. Generally, forward scattering can be reduced by using a thin resist. Backscattering of electrons are generally more pronounced for heavy atoms (large Z), and their range increase with increasing electron energy [77]. Secondary electrons generated by forward scattered electrons or from plasmon decay, are still responsible for most of the exposure [79, 85].

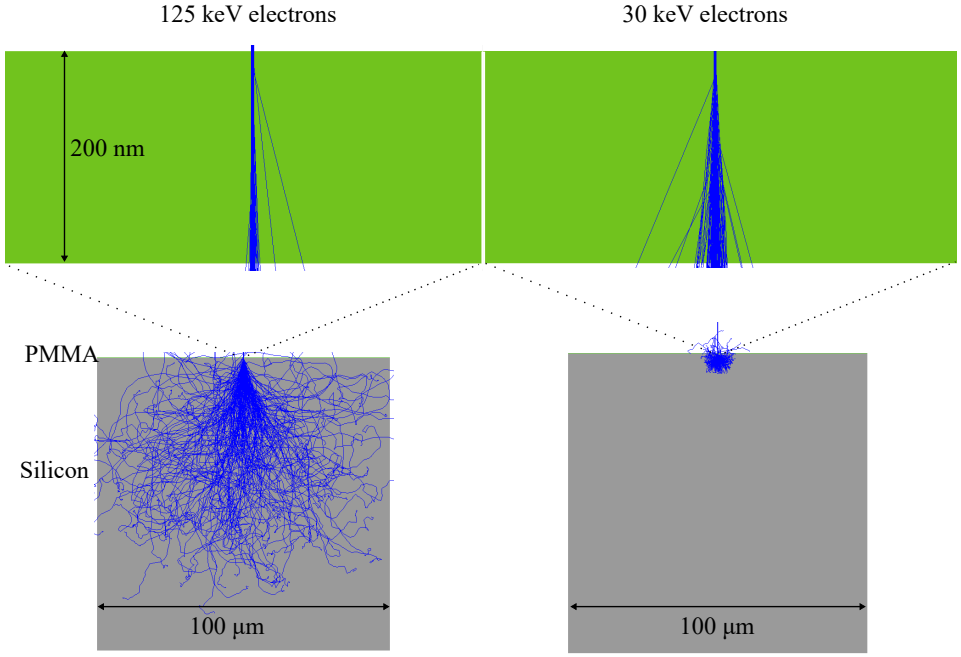

Figure 2.2: Electron trajectories into 200 nm PMMA on silicon calculated using 125 keV and 30 keV electrons. The calculations are done using the free software CASINO [20].

2.1.2 Helium ion beam lithography

The helium ion beam microscope (Orion, Zeiss) was commercialized in 2007. An important difference between an SEM (or an EBL instrument for that matter) and a helium ion beam microscope is the source. The helium ion microscope employs a gas field ion source. The source is placed in high vacuum under cryogenic temperatures (working temperature 60 - 90 K). The tungsten tip is positively biased relative to the extractor electrode. This sets up a large electric field that is used to select the emission sites, the trimer, by field evaporating tip-atoms. The trimer consists of three atoms and only one is selected for imaging (or lithography). Any helium atom gas near the trimer is ionized due to the large electric field (minimum 4.4 V/Å). The ion current appears to come from an atomic-sized volume and as such the brightness is high, up to 5×10^9 A/cm^{2}sr under optimized conditions. In the source chamber the base pressure (that is, the pressure in the absence of helium gas) is $< 4 \times 10^{-10}$ Torr. This is crucial to preserve the trimer and its surroundings, because adsorption of adatoms can steal current or cause the selected trimer-atom to be lost [86].

The properties of the gas field ion source, that is the high brightness, the low energy spread (less than 1 eV), a de Broglie wavelength in the femtometer-range and the atomic-sized virtual source size, influences the spot size. It should be mentioned that the small virtual source size implies that a relatively large column magnification is needed, making the helium ion beam microscope more sensitive to mechanical vibrations than an SEM [86]. That being said, an 0.24 nm 25-75 % edge resolution in a secondary-electron image has been demonstrated [87, 88]. Moreover, the helium ion beam microscope has an electron flood gun, enabling in principle high-resolution imaging of non-conductive materials.

The helium ion beam microscope at the Massachusetts Institute of Technology was in this work used for resist-based lithography. The microscope was equipped with a 16-bit pattern generation (Elphy multibeam), but has no laser-interferometric stage and hence the maximum area one can write is limited by the area written solely by beam deflection (write-field). Beam currents of about 1 pA was used to expose HSQ, with doses in the range 50 - 100 μC/cm^2. At this dose density range, the generation of re-coil atoms is assumed to be negligible [89].

One key feature about helium ion beam lithography, or lithography with other light ions, is the reduced proximity effect as the heavy ions backscatter less than electrons. As in EBL, the secondary electrons are responsible for most of the exposure, and as the stopping power for helium ions is greater than for electrons (see Figure 1.1), the number of secondary electrons generated per unit length is larger, leading to higher resist-sensitivity [22]. The potential in high-resolution lithography is motivated by the sub-1 nm spot size and the beam profile < 100 nm into the resist, however but as shown by Winston et al. [22] and by Scipioni et al. [23] currently the resolution is comparable to that of an EBL tool.

2.2 Pattern transfer

Planar nanofabrication typically consists of two steps; lithography and pattern transfer. Various methods of pattern transfer exists such as electroplating, deposition of functional material followed by lift-off, etching and implanting [84]. In this thesis work, pattern transfer was done using reactive ion etching or metal deposition followed by a lift-off procedure, as illustrated in Figure 2.3.

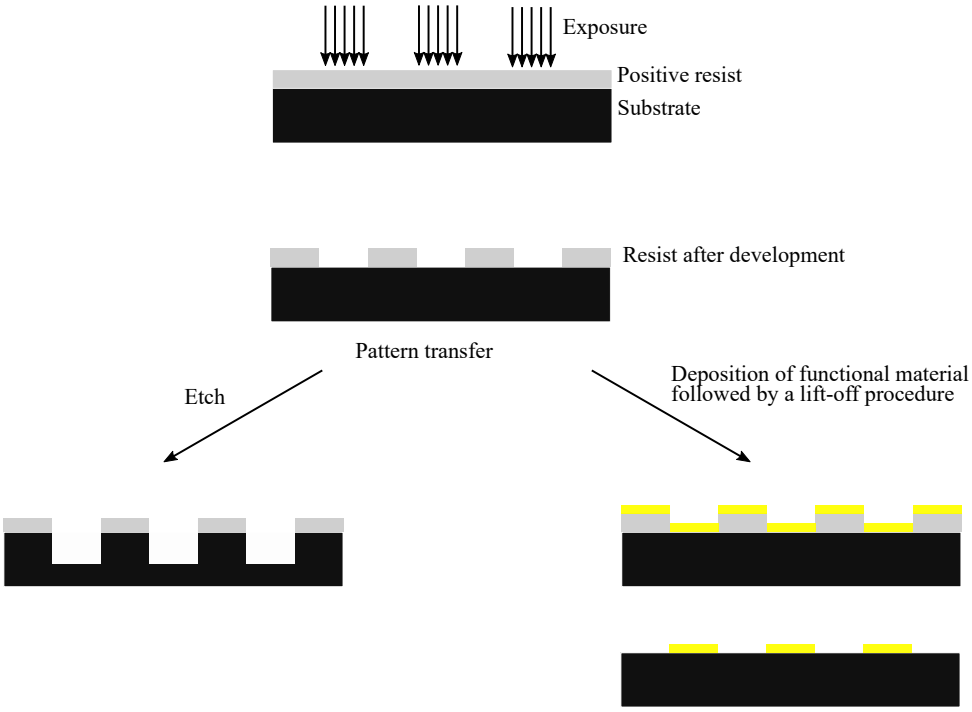

Figure 2.3: Illustration of (typical) fabrication procedures that were used in this thesis work. The resist, in this case a positive tone, is exposed with charged particles and developed in a developer solution. In the left panel the underlying substrate is etched. Etching may require an etch mask in addition to the resist. In the right panel a functional material is deposited on top of the resist. The resist and the surplus metal is removed in a sub-sequent lift-off procedure.

2.2.1 Electron beam evaporation and lift-off

Electron beam evaporation is a physical vapor deposition technique. The operation principle of the technique is illustrated in Figure 2.4. In short, during a deposition process the source material is locally heated to its boiling/sublimation point by the means of a high-energy electron beam. A shutter covers the sample before the desired deposition rate is reached. An oscillating quartz crystal monitors the rate of evaporation, which can be adjusted by changing the beam

current. Deposition rates can range from Å/s to µm/s. The process occurs in high vacuum and the vapor of the source material condenses onto the surface as a uniform film, as illustrated in Figure 2.4.

The electron beam evaporation tool at the University of Bergen (Temescal FC-2000) can be used to deposit metals and insulators. The latter is possible due to the electron beam sweep controller. The electron beam sweep controller controls the movement of electron beam and can be tuned to evenly heat the source material. For example, SiO_2 has a low thermal conductivity and evaporation using a stationary electron beam will relatively rapidly result in the evaporation of the crucible material.

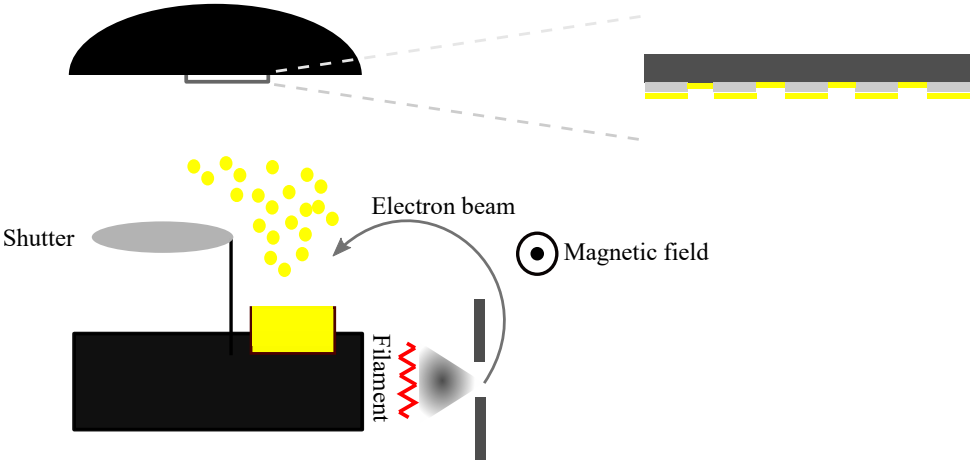

Figure 2.4: Illustration of the basic principle of electron beam evaporation. The electron beam is guided to the crucible containing the source material by a magnetic field and heats the source material so that it evaporates onto the sample as a uniform film.

Electron beam evaporation at normal incidence is used when lift-off is required. Positive-tone PMMA has an undercut profile due to electron scattering, as illustrated in Figure 2.5. A good rule of thumb for successful lift-off is that the ratio of metal-thickness to PMMA-thickness should be a minimum of 1:3. In a lift-off procedure, the sample is submerged in N-Methyl-2-pyrrolidone (NMP) heated to about 80° Celsius, and the sacrificial PMMA peel off along with the surplus metal.

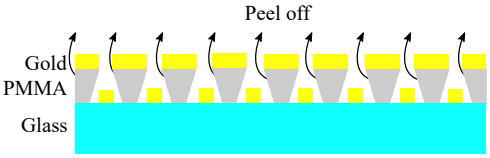

Figure 2.5: Illustration of the lift-off procedure. The sample is immersed in a heated NMP solution and the sacrifical PMMA peel off along with the surplus metal.

2.2.2 Reactive ion etching

Whereas metal deposition and lift-off is an additive process, etching is a subtractive process. Etching is divided into two categories: chemical wet-etching and dry etching. An isotropic etch removes the material in all directions with the same rate [10]. This is typically the case for chemical wet-etches, but there are exceptions e.g. potassium hydroxide (KOH) which is a partial anisotropic etch. KOH attacks silicon preferentially in the <100> direction and is discussed in greater detail in Appendix B. In contrast, dry etches often offer a higher degree of anisotropicity. That being said, dry-etching techniques typically have a lower selectivity to the material being etched so the finite etch rate of the mask needs to be taken into consideration. An important class of dry-etches is plasma-based etching. It can take various forms, but common for all is that volatile species are generated [1].

In this thesis work, reactive ion etching (RIE) was used. RIE employs both physical (momentum transfer) and chemical processes to etch a material [10]. As illustrated in Figure 2.6, the lower electrode is connected to a radio frequency (RF) power supply, while the upper electrode is connected to ground. A relatively stable gas is introduced into the vacuum. The gas is ionized and forms radicals and ionic species. Heavy ions cannot follow the RF oscillations, unlike the electrons, and this generates a self-bias, V_{dc}.

The reactive species adsorb on the surface of the material being etch. A reaction takes place and re-arrangement occurs to form a volatile product [90]. The process of re-arrangement is not well understood and is likely facilitated by ion bombardment [84]. Silicon or silicon compounds, such as SiO_2 or Si_3N_4, are etch using flurocarbons e.g. CF_4, CHF_3 or SF_6 and creates the volatile product SiF_4. The etch result is affected by RF power, the gas flow rate, the composition of the gases, the chamber pressure, substrate temperature, but also e.g. the presence of contaminants in the chamber [91]. As an example, SEM images of the etch-profile in Si_3N_4 using CF_4 as the etch gas is shown in Figure 2.7. The etch mask consists of antireflective coating (ARC, Brewster Science, XHRIC-11), SiO_2 and PMMA. The etch-parameters are discussed in greater detail in Appendix C, but note the high degree of directionality.

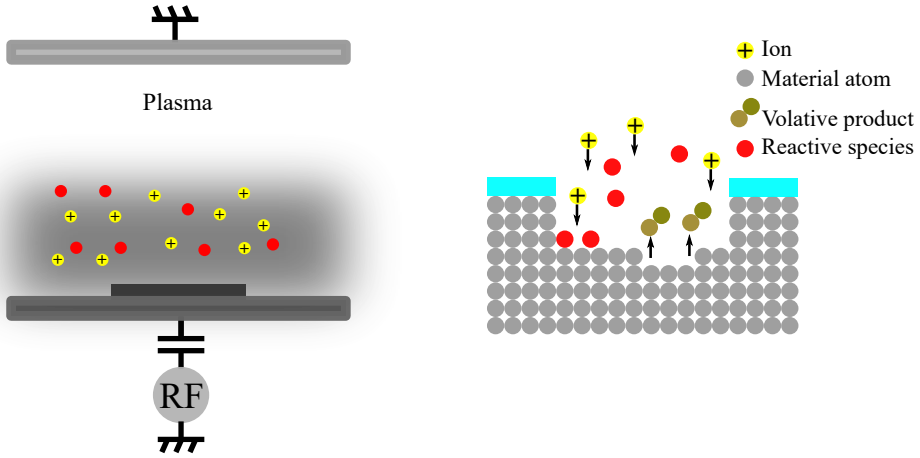

Figure 2.6: Illustration of the basic principle of RIE. A relatively stable gas is introduced to the vacuum. The gas is ionized and forms reactive species that is adsorbed to surface of the sample being etched. A reaction takes place, facilitated by ion bombardment, and rearrangement occurs to form a volatile product which is removed by the vacuum.

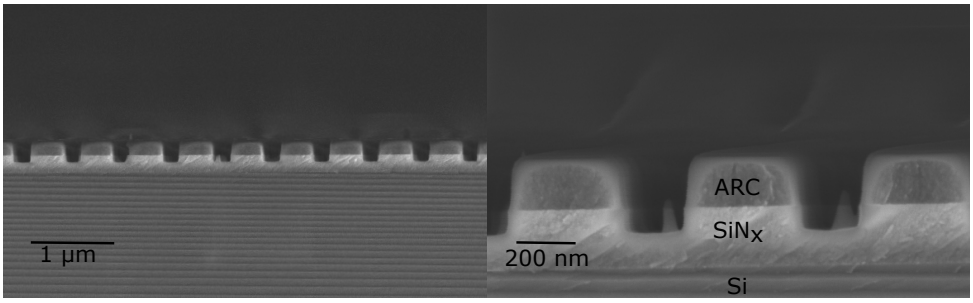

Figure 2.7: SEM images of the etch-profile in Si_3N_4 using CF_4 as the etch gas. The etch mask consists of antireflective coating (ARC, Brewster Science, XHRIC-11), SiO_2 and PMMA.

2.3 Optical characterization

2.3.1 Integrating spheres

Integrating spheres spatially measure the radiant flux of light by the means of integration. The inner surface of the sphere is covered with a highly reflective and diffuse material that scatters light in all spatial directions with equal amount (and as a result the light within the sphere is uniform). A description on how to find the absorption and scattering efficiencies based on the raw integrating sphere measurements are presented in Paper III and is described by Holm [92].

The set-up used in this thesis work consists of two spheres, one transmission sphere (Ocean Optics ISP-50-8-I) and one reflection sphere (Ocean Optics ISP-50-8-R-GT), as illustrated in

Figure 2.8. Light by a tungsten halogen light source (Ocean Optics HL-2000 380 nm – 2000 nm) enters the reflection sphere and generates a spot size at the sample port of approximately 3 mm. The incident angle is 8 ° relative to the surface normal. The reflection sphere is equipped with a gloss trap used to include or exclude specular reflection (specular reflection is included in the measurements in paper III). The spectrometer (Ocean Optics USB400-VIS-NIR ES) has a spectral resolution of $\sim$ 1.5 nm. One intrinsic source of error in integrating sphere measurements are the ports. The ports (entrance, sample and detector) are not coated with the diffusive material and information will be lost. As a rule of thumb, the total area of the port should be less than 5 % of the internal area of the spheres to minimize such errors [93].

In paper III, the light reflected off the sample and the light transmitted through the sample is measured. The light extinct by the sample are measured using another set-up. The spheres were calibrated based on reference spectra. The reference spectrum in the reflection sphere is obtained using a diffuse reflection standard (WS-1 Reflectance Standard), while an empty sphere (the light source) was used as reference spectrum for the transmission sphere. The nanoparticles are resting on glass and to extract the optical properties of the nanoparticles the contribution of the glass (measured in near proximity of the metal nanoparticles) was subtracted. Once the light being extinct by the nanoparticles is known, the light absorbed by the nanoparticles can be found via the principle of conservation of energy.

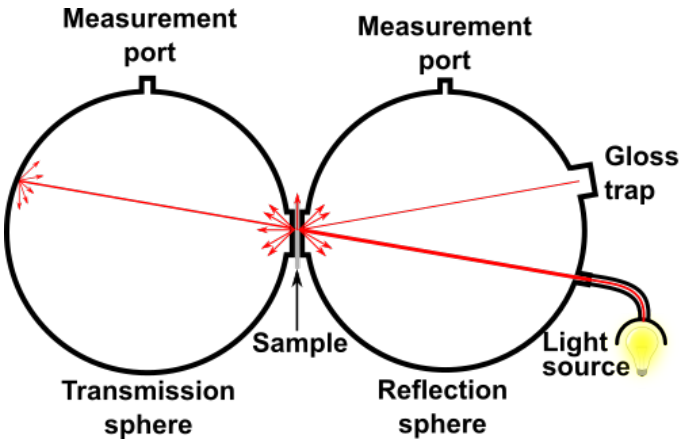

Figure 2.8: Illustration of the integrating sphere set-up. It consists of one reflection sphere and one transmission sphere. The light enters the reflection sphere, interacts with the sample and can be scattered multiple times of sphere walls. The figure is reproduced with the premission from [53].

2.4 The appendices

Suplimentary information and preliminary results are presented in the appendices. The appendices encloses:

- **Appendix A** presents an alternative neon-ion beam milling procedure for making an atom sieve. Preliminary results are included.
- **Appendix B** includes the experimental procedure for fabricating silicon nitride membranes.
- **Appendix C** discusses RIE for making free-standing structures. Two different etch-masks are examined (a) ARC, SiO_2 and PMMA and (b) PMMA.

Chapter 3

Conclusion and outlook

The work presented in this thesis is grounded in exploring charged particle lithography to develop new optical elements. Five papers, where the thesis defender is the first author (shared first-authorship in paper V), have been published in peer-reviewed journal. This chapter concludes and proposes further work.

3.1 Conclusion and outlook

In paper I resist-based lithography with helium ions was used to (a) fabricate high-density gratings over areas up to 100 μm × 100 μm and (b) pattern on a tilted surface to explore the large depth of field. The high-density gratings were intended for the generation of Smith-Purcell radiation spanning the visible to the UV regime, powered by a standard microscope beam. It has, however, not been tested during the course of this thesis work. Nevertheless, the idea was to deposit SiO_2 on top of the HSQ grating and thus have a dielectric grating and study how (or if) it interacts with the electron beam (for electron beam energies < 10 keV). Smith-Purcell is traditionally produced using conductive (or semi-conductive) gratings and light in the UV-regime have been produced see e.g. [37]. That being said, as metals typically have their plasma frequency in the EUV (around 10 eV) the screening charges in the metal may not respond fast enough to generate Smith-Purcell radiation at these wavelength and investigating other materials is thus important. In retrospect, the underlying substrate in the produced gratings is silicon, and silicon has strong cathodoluminescence signal in the visible (around 550 nm) [39], and hence is not ideal for Smith-Purcell generation. Thus, the fabricated grating would only work as a first test and optimization of material should be done. The second part of the paper I present the first experiment demonstrating resist-based helium ion lithography (HIL) on a tilted surface. To perform the same experiment using an electron beam would gain a direct comparison of the capabilities of HIL. This should also be done with a neon ion beam. Finally, the large depth of field could be used to pattern on a functional device e.g. an optical fiber or a lens. Spin-coating resists on curved surfaces is a challenge, but

with methods such as evaporation coating [94] and dip-coating [95] it is by all means possible.

Paper II presents a systematic investigation of the charging effect in SEM. Gold nanostructures on glass substrates are found to appear smaller than their real dimensions due to negative charging, comparable to a de-magnified image. During excessive imaging of the structure, the gold degraded and this degradation should be investigated in greater detail. A theoretical model could gain more information of the phenomena. Furthermore, investigating other non-conductive materials could be relevant. As a final note, doing the same experiment with a helium ion beam would be interesting on a fundamental level.

Paper III deals with the absorption and scattering of light by gold nanoparticles. The samples were fabricated using electron beam lithography followed by metal deposition and lift-off, and their optical response was compared to that of Langhammer et al. [54] who performed similar measurements on HCL fabricated samples. The EBL fabricated sample and HCL fabricated samples show similar optical response. However, the EBL samples were periodic arrays and diffraction effects are discussed as a potential reason for the splitting of the spectral position of the LSRP of the scattering and absorption efficiencies. Simulations were done using the software Lumerical which provides finite-difference time-domain (FDTD) solutions. Only single particles were simulated, but as diffraction was discussed, future work should include simulations of multiple particles to study this effect theoretically.

In paper IV a high-transmission atom sieve for focusing neutral helium atoms was fabricated by the means of EBL and reactive ion etching. The holes in the sieve were distributed along the Fresnel zones and the smallest hole has a diameter of 38 ± 4 nm. Additionally, smaller holes were made with a diameter down to 15 nm, showing that sub-10 nm focusing should in principle be possible. An attractive alternative one-step fabrication procedure is neon ion beam milling, which is described in Appendix A. Currently, making a full sieve using neon ion beam milling is challenging due to beam current fluctuations. Ultimately the goal will be to integrate the atom sieve in a new neutral helium atom microscope instrument. This development work is ongoing in the Nanophysics group.

Paper V demonstrates fast resolution change in NeMi by inserting collimating apertures of various diameters in the microscope. It allows us to change the microscope resolution without breaking the vacuum or changing the properties of the neutral helium beam (their de Broglie wavelength). The collimating apertures are already installed in the current neutral helium microscope at the University of Bergen. In the new design aiming for 10 nm resolution, smaller apertures must be made, and paper IV has shown that it is possible to make such holes.

Part II

Papers

Journal of Microscopy

Journal of Microscopy, Vol. 265, Issue 3 2017, pp. 287–297 doi: 10.1111/jmi.12497
Received 2 September 2015; accepted 2 October 2016

A systematic investigation of the charging effect in scanning electron microscopy for metal nanostructures on insulating substrates

R. FLATABØ*, A. COSTE† & M.M. GREVE*
**Department of Physics and Technology, University of Bergen, Bergen, Norway*
†École normale supérieure de Lyon, Lyon, France

Key words. Charging effect, measurement error, nanostructures, secondary electron detector, SEM.

Summary

Scanning electron microscopy is perhaps the most important method for investigating and characterizing nanostructures. A well-known challenge in scanning electron microscopy is the investigation of insulating materials. As insulating materials do not provide a path to ground they accumulate charge, evident as image drift and image distortions. In previous work, we have seen that sample charging in arrays of metal nanoparticles on glass substrates leads to a shrinkage effect, resulting in a measurement error in the nanoparticle dimension of up to 15% at 10 kV and a probe current of 80 ± 10 pA. In order to investigate this effect in detail, we have fabricated metal nanostructures on insulating borosilicate glass using electron beam lithography. Electron beam lithography allows us to tailor the design of our metal nanostructures and the area coverage. The measurements are carried out using two commonly available secondary electron detectors in scanning electron microscopes, namely, an InLens- and an Everhart–Thornley detector. We identify and discriminate several contributions to the effect by varying microscope settings, including the size of the aperture, the beam current, the working distance and the acceleration voltage. We image metal nanostructures of various sizes and geometries, investigating the influence of scan-direction of the electron beam and secondary electron detector used for imaging. The relative measurement error, which we measure as high as 20% for some settings, is found to depend on the acceleration voltage and the type of secondary electron detector used for imaging. In particular, the Everhart–Thornley detectors lower sensitivity to SE_1 electrons increase the magnitude of the shrinkage of up to 10% relative to the InLens measurements. Finally, a method for estimating charge balance in insulating samples is presented.

Correspondence to: Martin M. Greve, Allegaten 55, 5020 Bergen, Norway. Tel:+47 55 58 83 26; e-mail: martin.greve@uib.no

Introduction

Nanostructures of metallic, semiconducting and insulating materials have attracted a great deal of attention due to their novel physical and chemical properties (Rao & Cheetham, 2001). Thanks to progress in nanofabrication techniques and methods for characterization and manipulation, nanostructured devices hold great promise in, e.g. photonic-, optoelectronic-, catalytic-, environmental-, biomedical- and therapeutic applications (Daniel & Astruc, 2004; Baxter & Aydil, 2005; Cho *et al.*, 2008; Sanvicens & Marco, 2008; Sieb *et al.*, 2009; Talapin *et al.*, 2009).

Nanostructures can routinely be fabricated using a wide range of methods, including physical vapour deposition-based techniques, chemical synthesizing and lithography techniques (Hulteen & Van Duyne, 1995; Hyeon, 2003; Rechberger *et al.*, 2003; Sander & Tan, 2003; Langhammer *et al.*, 2007; Ferrando *et al.*, 2008). The various methods have different benefits and drawbacks, e.g. the ability to control size, the particle density (in solution or on substrates), the particle throughput and arrangement of particles (e.g. arrays) (Stepanova & Dew, 2011).

Independent of the fabrication method, characterization of nanostructures is of key importance as the physical and chemical properties strongly depend upon particle size. Transmission electron microscope (TEM), atomic force microscope (AFM) and scanning electron microscope (SEM) can be used for this purpose (Sun & Xia, 2002; Goldstein *et al.*, 2003; Rechberger *et al.*, 2003; Langhammer *et al.*, 2008; Greve *et al.*, 2013). SEM is, perhaps, the main characterization method due to the resolution, simplicity in operation, image quality and promptness of the microscope (Goldstein *et al.*, 2003).

The characterization of insulating materials is a well-known challenge in SEM (Cazaux, 1999; Joy & Joy, 1999; Thong *et al.*, 2001; Ose *et al.*, 2002; Goldstein *et al.*, 2003; Okai *et al.*, 2011; Okai & Sohda, 2012). Insulating samples do not provide a path to ground and therefore accumulate charge. As a result of the

accumulated charge, the path of the incident and emitted electrons are deflected, evident as image distortions (Jbara *et al.*, 2004; Okai *et al.*, 2011; Okai & Sohda, 2012).

In previous work, we fabricated large arrays of metal nanoparticles on insulating glass substrates using electron beam (EBL) lithography to study the optical properties of the arrays (Greve *et al.*, 2013). The size and shape of the metal nanoparticles were characterized by the means of SEM and AFM. During the SEM characterization, the measured dimensions were found to be smaller than the designed structures both with respect to particle size and interparticle spacing. The shapes corresponded well to the designed structures. Commonly in EBL, the input pattern must be shaped-biased to achieve the desired dimension of the structure, that is, the shape of the design parameters must be optimized to correct for, e.g. proximity effects (Misaka *et al.*, 1990). However, after sputter-coating a thin layer (approximately 4 nm) of gold palladium new SEM measurements were made. In this conductive environment, SEM measurements of the metal nanoparticle dimensions were found to correspond well with the designed structures. The metal nanoparticle diameter and the interparticle distance shrunk approximately 15% when investigated directly on the insulating glass substrate, using an acceleration voltage of 10 kV and a probe current of 80 ± 10 pA, with respect to the conductive sample coated with gold palladium.

In this work, we study the measurement error in the SEM for metal nanostructures of different shape and size on insulating glass substrates. The nanostructures are investigated under various conditions by varying the beam current, aperture size, acceleration voltage, working distance, scan-direction of the electron beam, grid bias of the ET detector, as well as the size and the geometry of the nanostructures. The measurements are carried out using commonly available secondary electron (SE) detectors, namely, an Everhart–Thornley (ET) and an InLens detector. Using two different detectors allows us to identify several contributions to the measurement error.

Charging effect

A SEM image is formed by raster-scanning a focused electron beam across a sample. The incident electrons interact with the sample and generate signals that can be detected (Goldstein *et al.*, 2003). Secondary electrons (SEs) are of main interest in imaging. SEs are generated via inelastic interactions and have energies below 50 eV (Goldstein *et al.*, 2003). Interactions between an incident electron, a so-called primary electron, and a sample electron generates SE_1. SE_2 is generated via interactions between a backscattered electron (BSE) and a sample electron (see Fig. 1 A). A BSE is a primary electron that has undergone large angle scattering (scattering angle $> 90^\circ$) in the sample. BSEs that escape into the vacuum can impinge on the chamber walls or on the pole piece and generate SE_3. SE_1 and SE_2 are collected by the InLens detector. A positively biased ET detector additionally detects SE_3 (Everhart *et al.*, 1959).

Qualitatively, the charging effect in SEM is described as follows: as an insulator does not provide a path to ground, a fraction of the primary electrons get trapped in the material. The trapped electrons generate an electric surface potential. This potential can change the energy and trajectory of the subsequent primary electrons in two ways. For a negative (positive) potential, the primary beam is slowed down (accelerated) decreasing (increasing) the maximum penetration depth of the beam. As a consequence, the SE yield is increased (decreased) (see Fig. 1 B).

The primary electrons and emitted SEs are deflected causing magnification variations, image drift and abnormal contrast (Cazaux, 1999; Jbara *et al.*, 2004; Fakhfakh *et al.*, 2010; Okai *et al.*, 2011; Okai & Sohda, 2012). Trapped primary electrons contribute to negative charging, whereas the emission of SEs and BSEs give rise to positive charging of the sample (Cazaux, 1999). In principle, it is possible to establish a dynamic charge balance, that is, a state where the sum of the incident and emitted electron-yield equals unity. This is illustrated in Figure 1(B). As can be seen, there are two crossover energies, E_1 and E_2, were charge balance is obtained. Commonly, E_1 is in the range 50–200 eV which is too low for conventional SEM. However, E_2 is found between 500 eV and a few keV, suitable for SEM applications (Joy & Joy, 1999; Rau *et al.*, 2008).

The SE yield is defined as

$$\delta = \frac{n_{SE}}{n_B}, \tag{1}$$

where n_{SE} is the number of SEs emitted from a sample subjected to n_B primary electrons. δ depends upon the sample material, the topography of the sample and the incident beam-energy (Seiler, 1983; Joy *et al.*, 2004). In general, the SE-coefficient decreases with increasing primary energy, as the escape depth of SEs is shallow and higher energy primary electrons undergo less inelastic scattering (Seiler, 1983; Shih *et al.*, 1997). However, in the case of charging the negative surface potential increases the SE yield, as mentioned above and illustrated in Figure 1(B).

The BSE yield is defined as

$$\eta = \frac{n_{BSE}}{n_B}, \tag{2}$$

where n_{BSE} is the number of backscattered electrons. η increases with increasing atomic number (Z), whereas the dependency on acceleration voltage is minor in the range between 10 and 50 keV (less than 10%) (Reimer & Tollkamp, 1980; Lloyd, 1987; Goldstein *et al.*, 2003).

Design and preparation of nanostructure arrays

The metal nanostructures were fabricated on borosilicate glass cover slips (Menzel Gläzer, Thermo Scientific, Braunschweig, Germany). Bare cover slips were cleaned in two separate

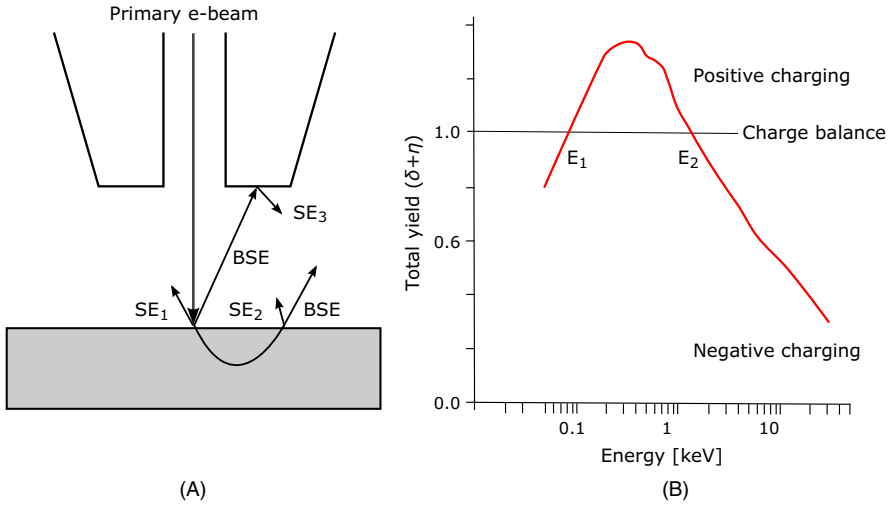

Fig. 1. (A) Schematics of where secondary electrons and backscattered electrons can be formed when an electron beam strikes a sample. Panel (B) shows the total emitted electron yield from an insulating material as a function of primary energy. At the crossover energies E_1 and E_2, charge balance is obtained. Whereas E_1 is too low for SEM applications (in the range 50–200 eV), E_2 is found to be between 500 eV and few keV. The figure has been adopted (to improve visibility) from Joy & Joy (1999). Note the log scale on the *x*-axis.

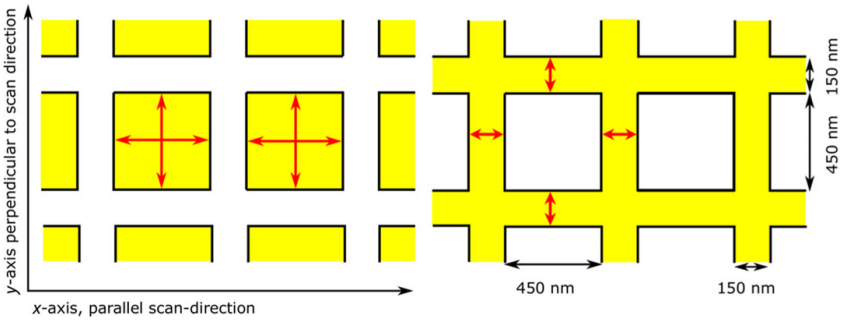

Fig. 2. Shows the general idea of the design used for fabricating the nanostructures. This design was repeated over a larger area. The metallized regions (Au) are shown in yellow, whereas the underlying substrate (borosilicate glass) is white. The sides of the gold squares are 450 nm and the spacing between each square is 150 nm in both directions. The inverse is true for the grid-lines. The structures were all measured at a magnification of 50 000 times, and the measurement points are shown with the red arrows. As can be seen, each measurement point consists of two independent measurements.

ultrasonic baths consisting of 2-propanone (acetone) (Emparta ACS, Merck KGaA, Darmstadt, Germany) and 2-propanol (isopropyl alcohol, IPA) (Emparta ACS, Merck KGaA), respectively, and dried using pressurized N_2. The cover slips were spin coated with a 180 ± 2-nm thick layer of poly(methyl methacrylate) (PMMA) (Ar-P672.08, Allresist GmbH, Strausberg, Germany). A 4 ± 1-nm thick layer of chrome was deposited on top using electron beam evaporation (Temescal FC 2000, Temescal Inc., Livermore, CA, USA). The chrome layer serves as a charge-dissipating layer eliminating drift during the lithography process. The design of the nanostructures patterned consisted of two inverse structures, namely, grid-lines and squares (see Fig. 2), and will be referred to as such in the remainder of this paper.

After patterning, the chrome layer was removed in a wet etch (Chromium Etchant 1020, Transene Company Inc., Danvers, MA, USA). Subsequently, the sample was soaked for 2 min in the developer; a 1:3 mixture of methyl-isobutyl-ketone (AR 600-56, Allresist GmbH) and 2-propanol. To stop the development process, the sample was rinsed with

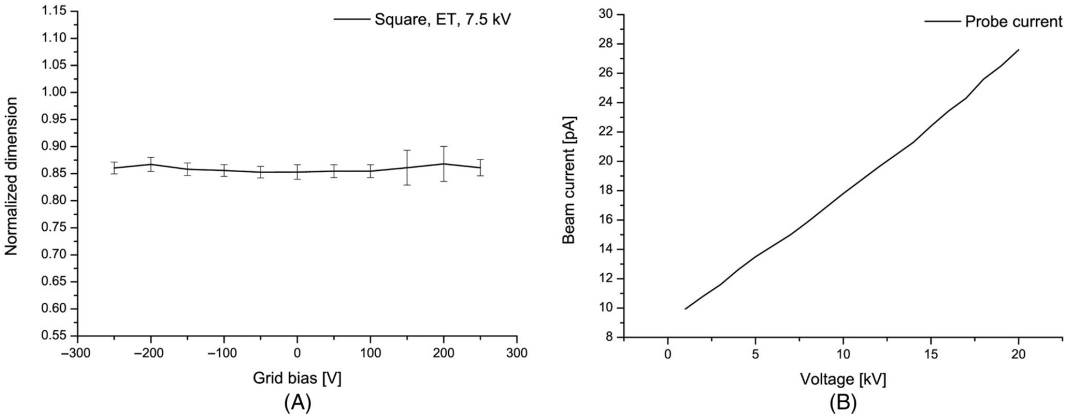

Fig. 3. (A) Normalized dimensions of squares using an aperture size of 10 μm and 7.5 kV acceleration voltage, resulting in identical charging conditions, whereas the ET detector grid bias was gradually decreased from 300 to −200 V. (B) Probe current versus acceleration voltage for the 10-μm aperture. The measurements are conducted using a Faraday cup.

2-propanol and dried using pressurized N_2. A 25 ± 1-nm gold layer was deposited onto the sample using electron beam evaporation, followed by a lift-off procedure by submerging the sample in n-methyl-2-pyrrolidone (BASF SE, Ludwigshafen, Germany) heated to 80°C. The lift-off peals of the PMMA with the surplus metal.

Finally, after measuring the dimensions of the nanostructures on the insulating substrate (see Section 'Measurement method'), the sample was coated with a 4 ± 1-nm thick layer of chrome by the means of electron beam evaporation. The real dimensions of the nanostructures were then verified in a conductive environment. Due to the nature of the electron beam evaporation with a long source-to-sample distance, small source, and relatively high vacuum ($\approx 1 \times 10^{-6}$ mbar) metal is mainly deposited perpendicular to the sample plane and hence minimizing any increase/decrease in lateral sample dimensions. In order to verify that this added material did not influence the measurement, an atomic force microscope scan was made of the samples with and without the chrome layer. We could not measure any difference in lateral dimension before and after deposition, and this effect is therefore neglected.

Measurement method

SEM images are obtained using a combined electron beam lithography and SEM system (Raith eLINE, Raith GmbH, Dortmund, Germany). The chamber pressure was approximately 8×10^{-7} mbar. Two different SE detectors, namely, an InLens and a positively biased (300 V) ET detector was used to perform the measurements. A positively biased ET detector was chosen to attract SEs (Goldstein *et al.*, 2003).

For both detectors, measurements were conducted using a working distance of 10.7 mm and 5.7 mm. The latter is the minimum working distance for a flat sample in the system, and because physical building up the sample could potentially change the sample conductivity, the working distance was not decreased beyond this.

In Figure 3(A), the ET detector grid bias has been gradually decreased from 300 V to −200 V. Beyond −50 eV, the ET detector is essentially a BSE detector. The SE_2 and the BSE are generated by electrons emerging from exactly the same sample volume when the ET detector is turned to 'BSE-mode'. This indicates that the build-up of electrical charge affects the shrinkage of SE_2 and BSE to the same degree. Furthermore, the electrical field induced in the sample does not cause additional image distortions for the lower energy SE_2.

As the SEM used in this work did not have a rotatable stage, the electron beam scan-direction was rotated from 0° to 180° in steps of 45° (see Fig. 4) to simulate a moving detector. Obviously, it is not the same as physically changing the position of the detector. Nevertheless, it shows that the sequence of which the pixels are exposed does not significantly affect the measured dimensions.

The acceleration voltage was systematically increased from 2.5 kV to 20 kV, in steps of 2.5 kV. Using the ET detector, we also conducted low-voltage measurements ranging from 1 kV to 2.5 kV. The InLens data fluctuate significantly at low voltages due to a shadowing effect in the SEM images. For this reason, these low-voltage measurements are discussed separately.

To investigate how the aperture size, and hence the probe current, affects the measured dimensions one measurement set using (2.5, 10, 20) kV were performed for each of the apertures (7.5, 10, 20, 30) μm. Increasing the size of the aperture

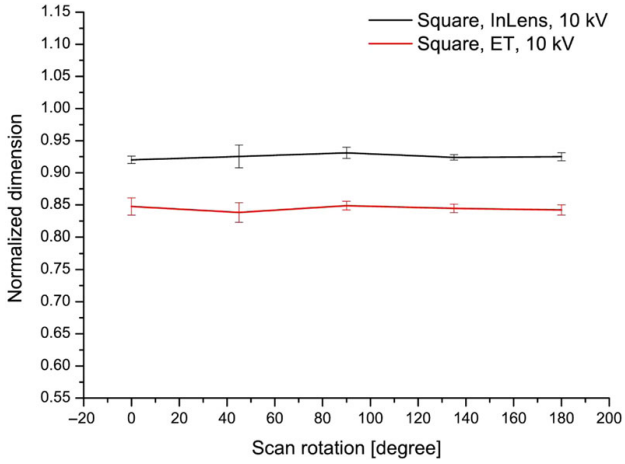

Fig. 4. Normalized dimensions of squares for various scan rotations using the InLens (black) detector and the ET detector (red).

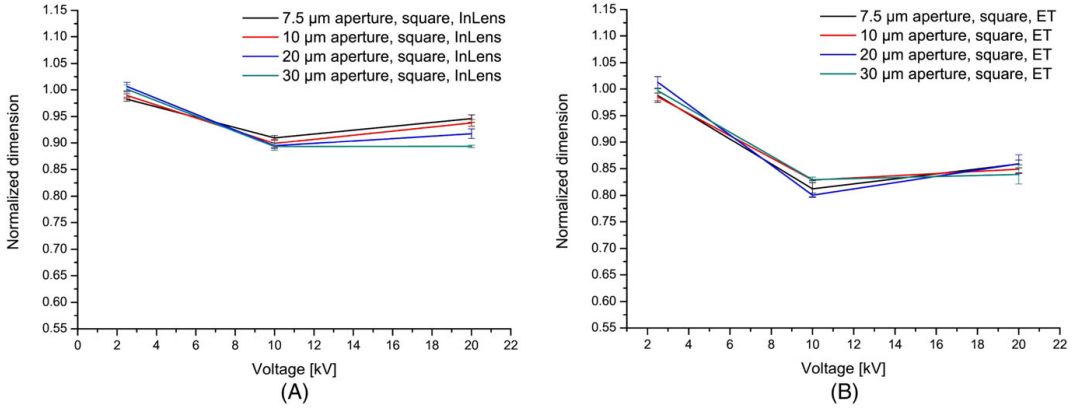

Fig. 5. Normalized dimensions of squares using (A) the InLens detector and (B) the ET detector for various aperture sizes (probe currents).

has a minor effect on the shrinkage effect (see Figs. 5 A and B). Therefore, only measurements obtained using an aperture of 10 µm is presented in the remainder of this paper (see Section 'Image optimization' for further discussion). The associated beam currents are given in Figure 3(B). The beam-probe size was estimated to be 10 ± 5 nm for all measurements. It should be noted that there might be a minor effect of increasing the probe current, elucidating itself for the InLens detector at high voltages (see 20 kV measurement points in Fig. 5 B). This effect has not been investigated further as it was only seen for the most extreme voltage used in this study.

The nanostructures, i.e. grid-lines and squares, are schematically depicted in Fig. 2 and SEM images are presented in Fig. 6. All measurements are obtained using a beam dwell time of 26.6 µs/pixel and a magnification of 50 000 times. The area within the SEM image at this magnification defines one field of view. For the grid-lines, the dimension of the lines along the x- and y-axis is measured three times per voltage step. In principle, the two lines along the x-axis (i.e. parallel to the scan-direction of the electron beam) and the two lines along the y-axis (i.e. perpendicular to scan-direction of the electron beam) have identical surroundings. Therefore, one measurement point is the average of six individual measurements. In the remainder of this paper, one measurement set defines six individual measurements per voltage step. In a similar manner, the measured length (x-axis) and width (y-axis) of the

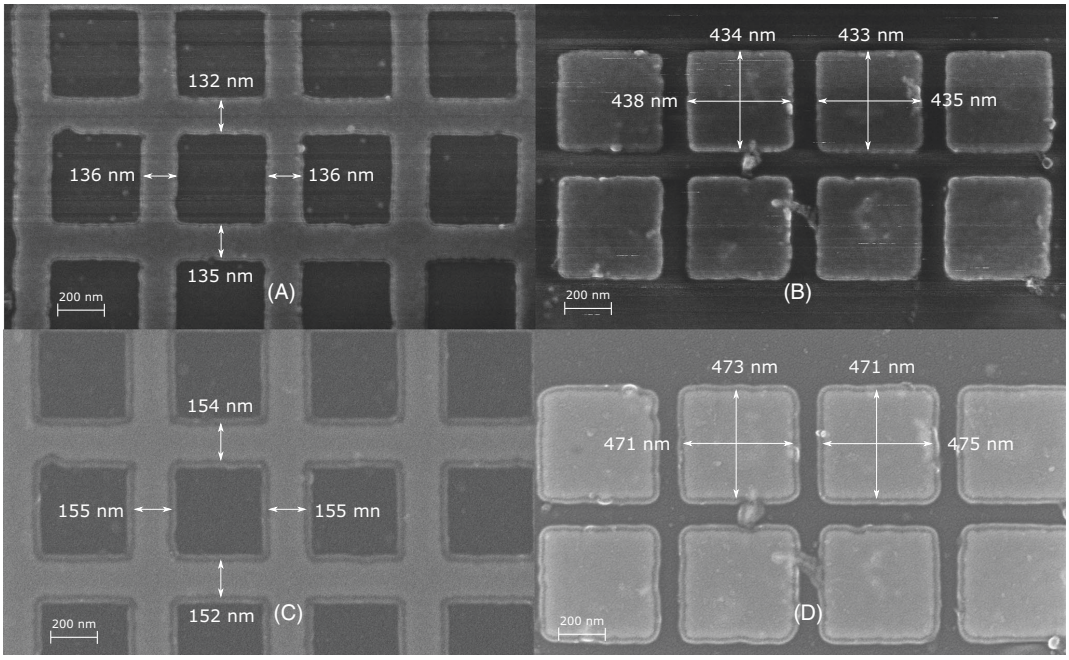

Fig. 6. (A, B) SEM images of grid-lines and squares under charging conditions. The images were taken at 15 kV and an aperture size of 10 μm using the InLens detector. (C, D) SEM images of grid-lines and squares when coated with thin layer of chrome. Note the additional edge visible around the structures, a reoccurring issue for samples exposed by the electron beam for longer periods of time (extensive imaging).

squares consist of six measurement points, again defining one set, for each voltage step.

Image processing and data analysis

The normalized dimensions of the nanostructures, that is, the ratio of the uncoated dimensions to the coated dimensions are plotted in Figures 7–11 (all plots have the same *x*- and *y*- range allowing a direct comparison). The data are normalized to the coated dimensions measured in the SEM to accommodate any size variations between different samples. If not otherwise specified, the presented data are the average of three measurement sets. Such averaging clearly smoothen the data, and it should be noted that this can suppress crucial information. Extensive measurements on a single field of view were not possible due to loss in contrast, caused by the energetic electron beam 'contaminating' the sample. The effect can be seen in Fig. 6 where an additional edge manifest itself around the structures. This sample contamination evolves as a function of time, and has been taken into account and eliminated as much as possible in all the presented data. Similar sample contamination has been observed by others (Kubby & Siegel, 1986), and introduces an additional level of difficulty to these measurements. This effect underlines the importance of presenting normalized data points.

Results and discussion

Image optimization

A SEM image with acceptable focus and minimal image artefacts is highly dependent on precise alignment of the microscope, and even more so when investigating insulating materials. It was found that the direction of the image drift coincides with the scan-direction of the electron beam. This is in contrast to previous assumptions stating independence of the two (Okai & Sohda, 2012). The image drift can in fact be completely eliminated for any image/structure by carefully aligning the objective aperture and the stigmation of the beam, resulting in a still image similar to that of a conductive sample. We speculate that the drift can be due to a slightly misaligned and stigmatic beam. This will result in a larger than expected spot size, which in turn introduces charge to the neighbouring pixel which has not yet been exposed. When the beam is moved from one pixel to the next it will be slightly repelled by the already injected and trapped electrons,

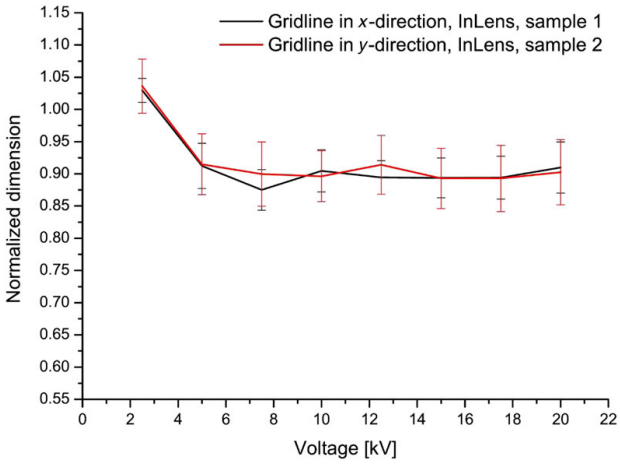

Fig. 7. Normalized dimensions of two different samples, named sample 1 and sample 2, measured under identical conditions by the means of the InLens detector. The reproducibility of the measurements as well as the shrinkage attributed to the charging effect is found to coincide. Each line is based on the average of three measurement sets, i.e. 18 measurements per voltage step obtained from three different field of views.

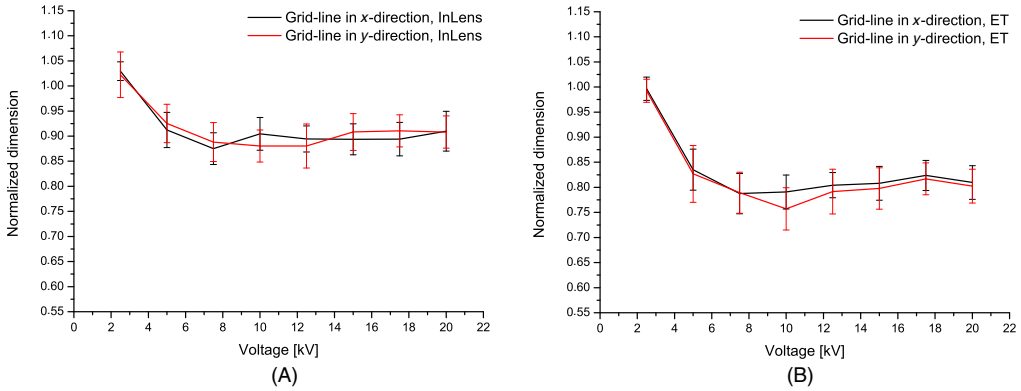

Fig. 8. Normalized dimensions of grid-line and squares measured using (A) the InLens detector and (B) the ET detector. No significant difference between the two scan-directions were found. This suggests that the observed shrinkage and therefore the distortions induced by the charging are independent of the scan-direction of the electron beam. The plots are based on the average of three measurement sets.

and hence the image will be pushed a tiny amount to the right (given that the beam is scanning from left to right) causing the drift. In the vertical direction, the time between the exposures of neighbouring pixels is much longer. Hence, some of the trapped charge has time to dissipate, weakening the effect which in turn minimize the vertical drift. This is supported by observations in the SEM; if a drifting image is recorded and the scan-direction is rotated 180°, the direction of the image drift is reversed.

Not surprisingly, a gradual loss in contrast emerges as the acceleration voltage is raised, which is accompanied by gradual increase of brightness. By manually increasing the contrast while reducing the brightness this loss is reduced. It should be noted that an acceptable contrast also depends upon the size of the aperture, as the area of the aperture is proportional to the beam current. An aperture size of 10 μm was found to give the best trade-off, providing the best contrast as well as an adequate signal-to-noise level. The use of a larger aperture greatly enhances the charging effects as the beam current is raised, whereas use of smaller apertures is challenging at lower voltages due to the decreasing signal-to-noise ratio.

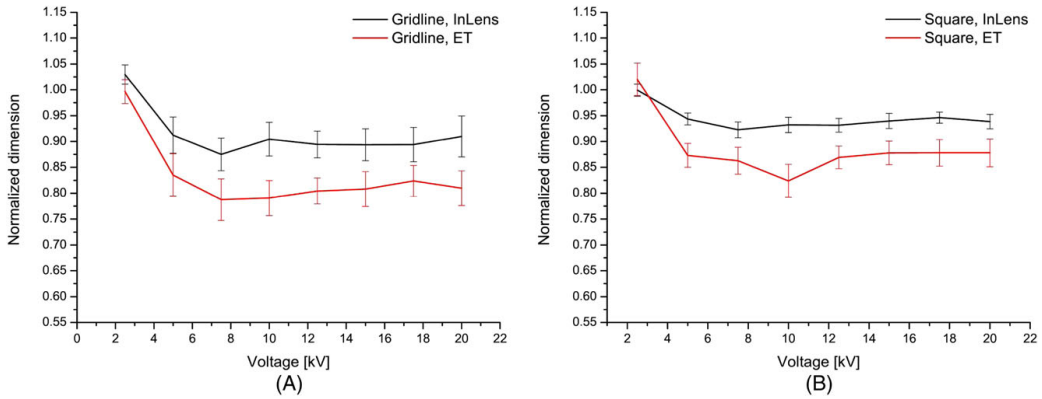

Fig. 9. Normalized dimensions of grid-lines (A) and sqaures (B) using the InLens and the ET detector. The discrepancy between the InLens and the ET detector is attributed to the low sensitivity of the ET detector to SE_1 electrons.

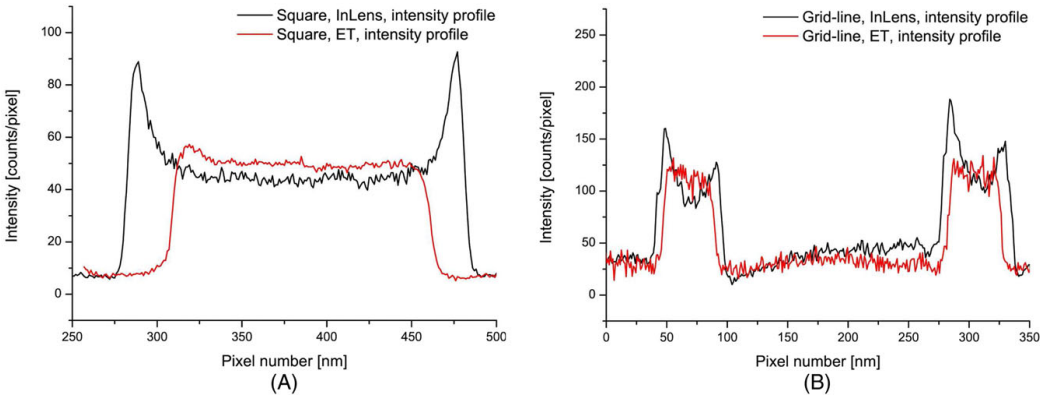

Fig. 10. (A) Intensity profile of two squares measured using the InLens- (black line) and the ET (red line) detector, an acceleration voltage of 12.5 kV and a working distance of 10.7 mm. Note that the large difference in the measured sizes is due to the high acceleration voltage. (B) Pitch and feature dimension of grid-lines measured using the InLens (black line) and the ET (red line) detector.

Analysing the SEM images

To test the reproducibility of the measurements, two independent samples were fabricated (following the design in Fig. 2) and investigated independently under identical conditions. The result is plotted in Fig. 7 and shows good agreement.

The dimension of the grid-lines and squares were measured along the *x*- and *y*-axis (see Fig. 2), and no significant difference between the two scan-directions were found, as can be seen in Fig. 8(A) and (B). This suggests that the observed shrinkage and therefore the distortion induced by the charging is independent of the scan-direction of the electron beam. Due to this independence of scan-direction, for simplicity, only measurements conducted along the *x*-axis will be presented hereinafter.

In Fig. 9, measurements of grid-lines and squares obtained using the InLens and the ET detector are compared. The ET line falls below the InLens line at all voltages beyond 2.5 kV independent of the coverage in the field of view. As mentioned, the InLens detector only collects SE_1 and SE_2, whereas the ET detector additionally detects SE_3 (see Fig. 1). SE_2 and SE_3 are generated by BSE and therefore follow the characteristics of the BSE yield. Above 10 keV for a given element, the BSE yield is almost independent of energy(Reimer & Tollkamp, 1980). Due to this independency, the ET data in Figures 8, 9 and 11

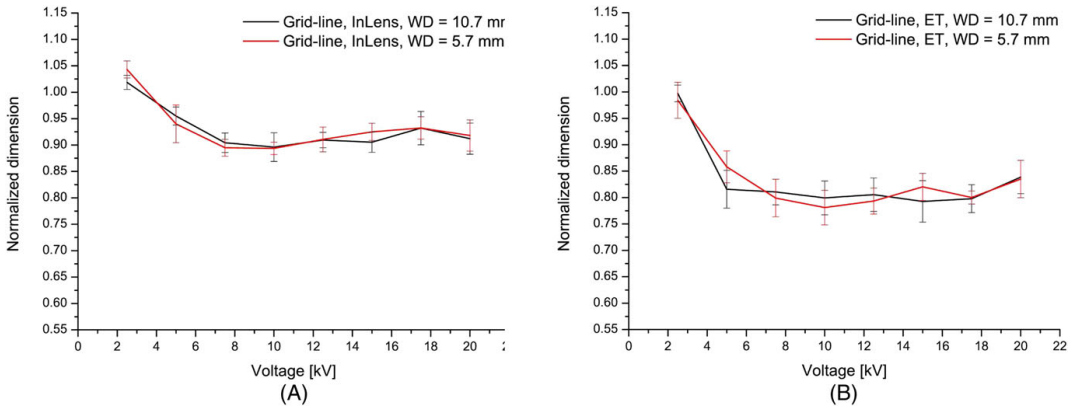

Fig. 11. Normalized dimensions of one measurement set obtained using different working distances for (A) the InLens detector and (B) the ET detector. The plots overlap, thus reducing the working distance does not affect the measurement error.

approximates a horizontal line above 10 kV. The dominating signal in the InLens detector is likely SE_1 (Griffin, 2011), which is a "true" SE-signal, and thus the data do not exhibit the same trend. As such, the discrepancy between the InLens and the ET detector is attributed to the low sensitivity of the ET detector to SE_1 electrons. Moreover, the detector quantum efficiencies for the InLens- and ET detector is ~0.6 and ~0.1 to 0.05, respectively, providing a better Signal-to-noise-ratio (SNR) for the former (Joy & Joy, 1996; Griffin, 2011).

Intensity profiles assessed from SEM images of squares obtained at a voltage of 12.5 kV are shown in Figure 10(A). The InLens- and ET-profiles are aligned so that the centres of the squares coincide. The InLens profile features an intensity increase, seen as a tip, at the border of the structure attributed to the collection of SE_1 (Joy, 1991; Griffin, 2011). This tip is not present in the ET profile. This can be explained by the ET detectors significantly lower sensitivity towards SE_1 and its ability to detect SE_3 (Goldstein *et al.*, 2003; Griffin, 2011). Bear in mind that this extreme size discrepancy seen in Figure 10 is due to the relatively high acceleration voltage used, deliberately chosen to clearly visualize and underline the effect. Also note that at the brightness and contrast settings are at their extremes, challenging the borderline between a real and a fictive signal (i.e. noise). In Figure 10(B), the pitch and the feature dimensions at 7.5 kV is presented. As can be seen, the pitch is the same, only the width of the grid-line profiles is different. The characteristic peaks of the SE_1 signal (seen for the InLens) is still absent for the ET.

The influence of the working distance on the measured dimensions is presented in Figure 11. Measurements were carried out using the InLens detector (A) and the ET detector (B), and a working distance of 10.7 mm (black line) and repeated for a working distance of 5.7 mm (red line). Both plots are the average of six individual measurements per voltage step, i.e. one measurement set within one field of view. The plots overlap to a degree indicating that a reduction in working distance does not affect the magnitude of the shrinkage effect for working distances of relevance in this work.

The build-up of negative charge in the sample is seen as a systematic shrinkage effect, manifesting itself as a demagnified image (Okai *et al.*, 2011). Positive sample charging would result in an overmagnified image, evident as an 'expansion effect'. At the second-cross over for charge balance, the normalized dimensions should equal 1. In the case of polycrystalline-SiO_2 and soda-lime glass, Rau *et al.* estimates it to be in the range of 1.5–2.7 keV depending on the model used for the calculations (Rau *et al.*, 2008). Here, charge balance is obtained at ~2.5 kV independent of the detector used to conduct the measurements.

Additional measurements were conducted for the ET detector in the voltage ranges 1.0 kV – 2.5 kV to investigate the region of positive charging. Figure 12 presents the normalized dimensions of grid-lines and squares. The sample charges positively throughout this voltage range, evident as an overmagnified image. Note that the x-axis is plotted as log-scale.

The total electron emission yield (see Fig. 1 B) is exponentially dependent on the acceleration voltage (Joy & Joy, 1999). It should therefore, in principle, be possible to fit three (or more) data points to an exponential function of the form $y = A\exp(\frac{-x}{t}) + y$ where A, t and y are constants, to estimate the second crossover. Determining this second crossover using the normalized dimensions of the nanostructures (uncoated/coated) is important as it reveals the substrate-dependent charge balance. Knowledge about the crossover allows arbitrary structure dimensions to be extracted under any charging condition by a three-point measurement and fitting of an exponential function in a similar manner as described above.

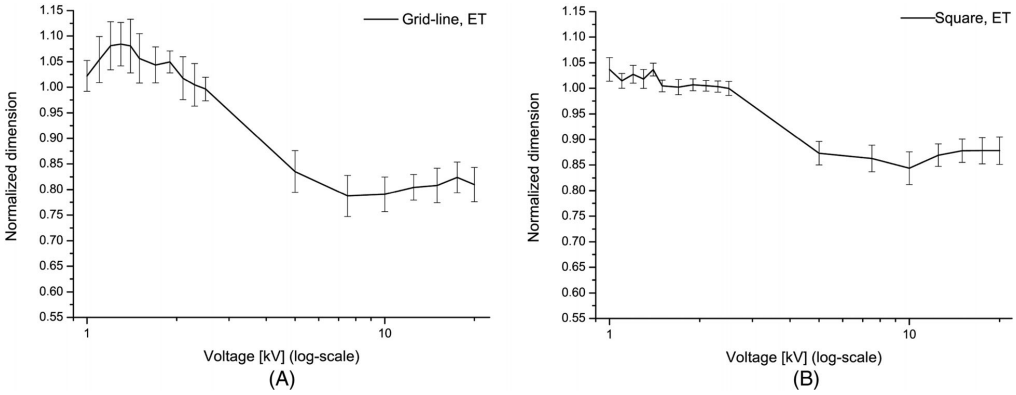

Fig. 12. Normalized dimensions of grid-lines (A) and squares (B) obtained using the ET detector. The normalized dimension reach 1 at approximately 2.5 kV indicating that charge balance is obtained and sound measurements can be made. The measurements are the average of three measurement sets. The *x*-axis is plotted on a log-scale.

Conclusion

We have investigated sample charging for gold nanostructures on glass substrates. The nanostructures have been imaged using commonly available SE detectors in an SEM. The shape and appearance of the nanostructures corresponds well to the designed structures. The measured dimension of the structures appears smaller than identical measurements in a conductive environment. This is caused by the build-up of negative charge in the sample and is comparable to a demagnified image. The magnitude of this shrinkage effect is found to be dependent on the type of SE detector, and the acceleration voltage. It is found to be independent of the working distance, probe current and scan-direction of the electron beam. A discrepancy in the dimensions measured by the two detectors has also been shown, where the InLens detectors ability to detect SE_1 leads to a smaller measurement error. A method for estimating the second crossover for charge balance in insulating materials, thereby allowing a measurement estimation of the real dimensions has been suggested. If imaging at charge balance is not possible, we recommend observation of charging samples in the SEM to be done at low voltage (<5 kV), using a 10-μm aperture in order to minimize the measurement error and to achieve the optimal contrast. To obtain an image of acceptable sharpness, we advise to reduce the brightness while increasing the contrast settings in the microscope. Finally, an image without drift is attainable by a precise alignment of the objective aperture and by eliminating stigmation.

Acknowledgements

The authors would like to thank Bergen Research Foundation for supporting this work. We thank Ørjan S. Handegård and Vårin R. A. Holm for help with atomic force microscope imaging. We also thank Bodil Holst for fruitful discussions and comments to the manuscript. This work was carried out using the facilities of the Bergen Nanostructures Laboratory.

References

Baxter, J. & Aydil, E. (2005) Nanowire-based dye-sensitized solar cells. *Appl. Phys. Lett.* **86**, 053114.

Cazaux, J. (1999) Some considerations on the secondary electron emission, δ, from e- irradiated insulators. *J. Appl. Phys.* **85**, 1137–1147.

Cho, K., Wang, X., Nie, S., Shin, D., Chen, Z. & Dong, M. (2008) Therapeutic nanoparticles for drug delivery in cancer. *Clin. Cancer Res.* **14**, 1310–1316.

Daniel, M. & Astruc, D. (2004). Gold nanoparticles: assembly, supramolecular chemistry, quantum-size-related properties, and applications toward biology, catalysis, and nanotechnology. *Chem Rev.* **104**, 293–346.

Everhart, T., Wells, O. & Oatley, C. (1959) Factors affecting contrast and resolution in the scanning electron microscope. *Int. J. Electron.* **7**, 97–111.

Fakhfakh, S., Jbara, O., Rondot, S., Hadjadj, A., Patat, J. & Fakhfakh, Z. (2010) Analysis of electrical charging and discharging kinetics of different glasses under electron irradiation in a scanning electron microscope. *J. Appl. Phys.* **108**, 093705-1–093705-10.

Ferrando, R., Jellinek, J. & Johnston, R.L. (2008) Nanoalloys: from theory to applications of alloy clusters and nanoparticles. *Chem. Rev.* **108**, 845–910.

Goldstein, J., Newbury, D., Joy, D., Lyman, C., Eclin, P., Lifshin, E., Sawyer, L. & Michael, J. (2003) *Scanning Electron Microscopy and X-ray Microanalysis*. 3rd edn. Springer, New York, USA.

Greve, M.M., Håvardstun, T.O. & Holst, B. (2013) Measuring the localized surface plasmon resonance effect on large arrays (5 mm x 5 mm) of gold and aluminum nanoparticles on borosilicate glass substrates, fabricated by electron beam lithography. *J. Vac. Sci. Technol. B Microelectron. Nanometer Struct.* **31**, 06F410.

Griffin, B. (2011) A comparison of conventional Everhart-Thornley style and in-lens secondary electron detector: a further variable in scanning electron microscopy. *Scanning* **33**, 162–173.

Hyeon, T. (2003) Chemical synthesis of magnetic nanoparticles. *Chem. Commun.* 927–934.

Hulteen, J.C. & Van Duyne, R.P. (1995) Nanosphere lithography: a materials general fabrication process for periodic particle array surfaces. *J. Vac. Sci. Technol. A* **13**, 1553–1558.

Jbara, O., Fakhfakh, S., Belhaj, M. & Rondot, S. (2004) Charge implantation measurement on electron-irradiated insulating materials by means of a SEM technique. *Microsc. Microanal.* **10**, 697–710.

Joy, D. (1991) Contrast in high-resolution scanning electron microscope images. *J. Microsc.* **161**, 343–355.

Joy, D. & Joy, C. (1996) Low voltage scanning electron microscopy. *Micron* **27**, 247–263.

Joy, D., Prasad, M. & Meyer, H. (2004) Experimental secondary electron spectra under SEM conditions. *J. Microsc.* **215**, 77–85.

Joy, D.C. & Joy, C.S. (1999) Study of the dependence of E2 energies on sample chemistry. *Microsc. Microanal.* **4**, 475–480.

Kubby, J. & Siegel, B. (1986) SEM and TEM observations of first and second order sputter-induced topography. *Nucl. Instrum. Methods Phys. Res. B* **13**, 319–323.

Langhammer, C., Kasemo, B. & Zorić, I. (2007) Absorption and scattering of light by Pt, Pd, Ag, and Au nanodisks: absolute cross sections and branching ratios. *J. Chem. Phys.* **126**, 194702-1–194702-11.

Langhammer, C., Schwind, M., Kasemo, B. & Zoric, I. (2008) Localized surface plasmon resonances in aluminum nanodisks. *Nano Lett.* **8**, 1461–1471.

Lloyd, G.E. (1987) Atomic number and crystallographic contrast images with the SEM: a review of backscattered electron techniques. *Mineral. Mag.* **51**, 3–19.

Misaka, A., Harafuji, K. & Nomura, N. (1990) Determination of proximity effect parameters in electron-beam lithography. *J. Appl. Phys.* **68**, 6472–6479.

Okai, N. & Sohda, Y. (2012) study on image drift induced by charging during observation by scanning electron microscope. *Jpn. J. Appl. Phys.* **51**, 06FB11.

Okai, N., Yano, T. & Sohda, Y. (2011) Charge modeling for metal layer on insulating substrate. *Ipn. J. Appl. Phys.* **50**, 06GC01.

Ose, Y., Ezumi, M., Ishijima, T., Todokoro, H. & Nagai, K. (2002) Correction method for high-precision CD-measurements on electrostatically charged wafers. In *SPIE's 27th Annual International Symposium on Microlithography* **4689**, 128–137.

Rao, C. & Cheetham, A. (2001) Science and technology of nanomaterials: current status and future prospects. *J. Mater. Chem.* **11**, 2887–2894.

Rau, E., Fakhfakh, S., Andrianov, M., Evstafeva, E., Jbara, O., Rondot, S. & Mouze, D. (2008) Second crossover energy of insulating materials using stationary electron beam under normal incidence. *Nucl. Instrum. Methods Phys. Res. B* **266**, 719–729.

Rechberger, W., Hohenau, A., Leitner, A., Krenn, J., Lamprecht, B. & Aussenegg, F. (2003) Optical properties of two interacting gold nanoparticles. *Opt. Commun.* **220**, 137–141.

Reimer, L. & Tollkamp, C. (1980) Measuring the backscattering coefficient and secondary electron yield inside a scanning electron microscope. *Scanning* **3**, 35–39.

Sander, M. & Tan, L. (2003) Nanoparticle arrays on surfaces fabricated using anodic alumina films as templates. *Adv. Funct. Mater.* **13**, 393–397.

Sanvicens, N. & Marco, M.P. (2008) Multifunctional nanoparticles–properties and prospects for their use in human medicine. *Trends Biotechnol.* **26**, 425–433.

Seiler, H. (1983) Secondary electron emission in the scanning electron microscope. *J. Appl. Phys.* **54**, R1–R18.

Shih, A., Yater, J., Hor, C. & Abrams, R. (1997) Secondary electron emission studies. *Appl. Surf. Sci.* **111**, 251–258.

Sieb, N., Wu, N., Majidi, E., Kukreja, R., Branda, N. & Gates, B. (2009) Hollow metal nanorods with tunable dimensions, porosity, and photonic properties. *ACS Nano* **3**, 1365–1372.

Stepanova, M. & Dew, S., eds. (2011) *Nanofabrication: Techniques and Principles*. Springer Science & Business Media, New York, USA.

Sun, Y. & Xia, Y. (2002) Shape-controlled synthesis of gold and silver nanoparticles. *Science* **298**, 2176–2179.

Talapin, D., Lee, J., Kovalenko, M. & Shevchenko, E. (2009) Prospects of colloidal nanocrystals for electronic and optoelectronic applications. *Chem. Rev.* **110**, 389–458.

Thong, J., Lee, K. & Wong, W. (2001) Reduction of charging effects using vector scanning in the scanning electron microscope. *Scanning* **23**, 395–402.

Light absorption and scattering of 40–170 nm gold nanoparticles on glass substrates

Ranveig Flatabø, Vårin R. A. Holm, Håkon Eidsvåg, Bodil Holst, and Martin M. Greve[a)]
Department of Physics and Technology, University of Bergen, Allégaten 55, 5007 Bergen, Norway

(Received 4 July 2017; accepted 31 October 2017; published 21 November 2017)

The localized surface plasmon resonance (LSPR) effect in metal nanoparticles is important for many applications ranging from detectors and sensors to photovoltaic devices. The LSPR wavelength is sensitive to the shape, size, surface condition, and surrounding environment. Therefore, it is important to compare the optical properties of metal nanoparticles of nominally similar dimensions and external conditions, but fabricated with different techniques. Here, a systematic study of the optical properties of large, periodic arrays (3×3 mm) of cylindrical, gold nanoparticles with diameters ranging from 39 ± 4 nm to 167 ± 5 nm and a height of 25 ± 1 nm is presented. The large arrays allow us to investigate the optical properties using an integrating sphere setup collecting the light scattered and absorbed by the nanoparticles. To the best of our knowledge, such a setup has not been used previously for electron beam lithography (EBL) fabricated samples mainly due the large sample area required. The authors compare our results with relevant literature and find a good agreement, which confirms the expected reproducibility of EBL. Further, the authors compare our absorption and scattering measurements with previous absorption and scattering measurements on large arrays of gold nanoparticles prepared on glass using hole-mask colloidal lithography. Finally, a comparison with simulations using a finite difference time domain software package (Lumerical, Inc.) is presented. The simulation results matches well with experimental results and are also supporting and detailing our comparison with published literature. The authors find a good agreement between the two fabrication methods. The small deviations found can be contributed to differences in the particle size and density distributions. *Published by the AVS.* https://doi.org/10.1116/1.4994113

I. INTRODUCTION

Over the last years, several studies have been carried out investigating the optical properties of metal nanoparticles.[1–3] The localized surface plasmon resonance (LSPR) effect can potentially be used in several applications ranging from detectors, sensors, and drugs to photovoltaic devices.[4–6] Several studies have revealed how minute differences in shape, surface condition, and surrounding environment can have a significant effect on the LSPR wavelength.[7,8] In this paper, we focus on gold nanoparticles prepared directly on glass substrates using lithography techniques.[9–11] The advantage of lithography is that the size of the nanoparticles, as well as the spacing between them on the substrate can be well controlled. The disadvantage, particularly for electron beam lithography (EBL), is that it takes a long time to prepare large samples.[12] For this reason, earlier studies of EBL fabricated metal nanoparticles have mostly been carried out on small ensembles, and the optical properties have mainly been investigated using optical microscopes in combination with a spectrophotometer, allowing the nanoparticle light extinction to be investigated. Such an investigation of gold nanoparticles can be found in Refs. 9–11 and 13–18. Furthermore, light scattered by metal nanoparticles can be studied using dark field spectroscopy, which in addition can allow changes in the polarization of light to be studied.[2,19–21]

Extinction is a measure for the light absorbed and scattered by the nanoparticles. For small particle sizes, absorption is dominant and the extinction spectrum thus gives a direct measure of the LSPR wavelength. However, for nanoparticle sizes above approximately 50 nm, light scattering becomes increasingly important. Hence, for nanoparticles larger than 50 nm, all the scattered light needs to be collected in order to obtain a proper absorption spectrum, that is, the LSPR wavelength. This has been done for gold nanoparticle arrays prepared on glass using hole-mask colloidal lithography (HCL),[11] but to our knowledge, up till now, not for EBL prepared arrays.

II. EXPERIMENT

A. Sample preparation

Large area arrays (3×3 mm) of gold nanoparticles were fabricated on glass using EBL (Raith e_Line). Gold is known to adhere quite badly on glass (dielectric materials). However, the use of an intermediate adhesive layer, such as commonly used thin film of titanium,[22] was not desirable as this affects the optical properties. We found that the nanoparticles stuck reasonably well to borosilicate glass microscope coverslips (Thermo Scientific). In order to realize the range of different nanoparticle sizes, a bilayer resist scheme was used. The bilayer scheme used in this work is carried out by first spin coating approximately 70 nm film of a high sensitivity PMMA resist [PMMA 495 K (Microchem 495 K PMMA)]. This was then baked at 175 °C for 5 min, followed

a)Electronic mail: martin.greve@uib.no

by another spin coating of a lower sensitivity PMMA resist [PMMA 950 K (Allresist AR-P 672.02)], and the sample was again baked at 175 °C for another 5 min. The higher sensitivity resist ensures a good undercut for the subsequent lift off, and the lower sensitivity a good EBL resolution. A charge dissipating 3 ± 1 nm film of chrome was deposited on top of the resist using electron beam evaporation (Temescal FC-2000). The resists were exposed using a 20 kV acceleration voltage, 20 μm aperture, a working distance of 10.5 mm, and an area dose of 120 μC/cm^2. For nanoparticle diameters of 72 nm and below, a dot exposure was used instead of area elements, using a dot dose of 0.0045 pC. The chrome layer was removed in a chrome wet etch, and the PMMA was developed by submerging the sample in a standard resist developer (Allresist AR 600-56) for 2 min. A 25 ± 1 nm gold film was deposited by means of electron beam evaporation (measured using an ellipsometer (Filmetrics F10-RT). Finally, the PMMA and the excess gold film was removed in a lift of step, by submerging the samples in *N*-methyl-2-pyrrolidone heated to 80 °C for about 30 min. The arrays were carefully rinsed using 2-propanol, and subsequently dried with compressed nitrogen gas. Nanoparticle arrays with diameters between 39 ± 4 and 167 ± 5 nm and a height of 25 ± 1 nm were fabricated. The arrays were arranged in a simple cubic pattern with lattice parameters greater than three times the nanoparticle diameter. A total of six arrays were prepared. Note that the SEM images were obtained without coating the samples with a conductive layer. Imaging of metal structures on insulating substrates can lead to distortion of the measured dimensions through substrate charging; however, by using specific settings in the SEM, true dimensions can be measured and relatively good still images acquired. This is discussed extensively in Ref. 23. The reason for not to coat the samples for SEM imaging is that the additional coating clearly would affect the optical properties, and it is desirable to keep the samples for future reference. To ensure reliable measurements, the SEM image settings used were a 2.5 kV beam with 10 μm aperture and a working distance of 10 mm.[23] Table I shows the sample overview presenting the actual versus targeted diameters, based on image analysis of on average 20 nanoparticles from each array. Note that the shape of the 167 nm nanoparticle (sample I) is found to be slightly elliptical, which causes the error bars to become relatively large.

TABLE I. Sample overview.

Sample	Nanoparticle size (nm)	Interparticle distance (nm)	Nanoparticle height (nm)	Surface coverage
A	39 ± 4	145 ± 2	25 ± 1	0.0568
C	72 ± 4	290 ± 2	25 ± 1	0.0559
E	80 ± 10	400 ± 2	25 ± 1	0.0314
G	125 ± 2	450 ± 2	25 ± 1	0.0606
I	167 ± 15	600 ± 2	25 ± 1	0.0608

B. Optical measurement setup

The large nanoparticle arrays fabricated in this work enabled us to investigate the optical properties using an integrating sphere setup (Ocean Optics ISP-50-8) and an extinction measurement setup (see Fig. 1). In the integrating sphere setup, the reflected and forward scattered light can be measured simultaneously over large solid angles. It consists of two spheres, with the sample sandwiched in between the spheres. The sphere walls are coated with a material yielding a Lambertian surface, having a reflectivity of greater than 98% for all wavelengths of interest. Light is incident upon the sample at 8°, and the uniform illumination (radiant flux) of the integrating spheres is measured using an optical fiber attached to the measurement port, yielding the spatial light– sample interaction. It should be noted that phase and polarization information is lost. To separately measure the sample extinction, a different setup using optical fibers for illuminating and collecting the signal is used [see Fig. 1(b)]. Since the incident angle of the light in the integrating spheres is not perpendicular to the sample surface, the sample is tilted 8° in the extinction setup so that the different measurements can be compared.

The extinction coefficient (E) can be written as

$$E = S + A, \tag{1}$$

where S is the scattering coefficient and A the absorption coefficient. The light reflected by the nanoparticles is detected in the reflection sphere, and we refer to this as S_R. In the transmission sphere, both the forward scattered light

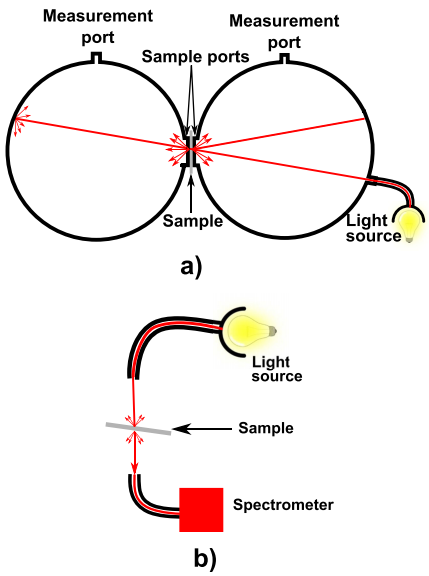

FIG. 1. (Color online) (a) Schematic illustration of the integrating sphere setup. The sample is sandwiched between the two spheres, and light is guided to, and collected from, the spheres using optical fibers. The acceptance angle of the measurement fiber is so low that there is no direct line of sight between the incident light and any first order reflections from the sphere walls. (b) Schematic illustration of the extinction measurement setup, used only for measuring the extinction separately. Note that the sample is tilted 8° relative to the incident beam, so that the different measurements can be compared.

and the directly transmitted (or extinct) light is detected. The forward scattered light by the nanoparticles, which we abbreviate S_T, can be calculated via the relation

$$S_T = E - T, \tag{2}$$

where T is the total amount of light detected in the transmission sphere. The light scattered by the sample in all spatial directions is then

$$S = S_R + S_T. \tag{3}$$

Combining this with Eq. (1) the light absorbed by the sample can be found. In order to extract the optical properties of the nanoparticles, the substrate (glass) was measured in the same manner, and its contribution subtracted. It should be noted that we discovered a notably variation in the optical properties between the individual substrates used for the nanoparticles arrays. Therefore, we found that it was crucial to measure the optical properties of the substrate close to the nanoparticle array on the same sample to achieve reliable results.

With the known nanoparticle absorption (A_{NP}) and (S_{NP}) constituting the overall nanoparticle scattering, the measurements are normalized to the real nanoparticle cross section, known as the scattering (Q_{sca}) and absorption efficiency (Q_{abs}),[24]

$$Q_{sca} = S_{NP}/(N\pi(d/2)^2), \tag{4}$$

$$Q_{abs} = A_{NP}/(N\pi(d/2)^2), \tag{5}$$

where N is the normalized unit cell coverage, and $\pi(d/2)^2$ is the cross-sectional area of a cylindrical shaped nanoparticle, where d is the nanoparticle diameter.

The center wavelength of the extinction peak is also important for comparison with the published literature (see Fig. 3).

C. Modeling

We used the FINITE DIFFERENCE TIME DOMAIN (FDTD) software package (Lumerical, Inc.) to model the absorption and scattering spectra. A $1200 \times 1200 \times 1200\,\text{nm}^3$ FDTD simulation space with perfectly matched layer (PML) boundaries is used as the simulation space. A 20, 25, or 50 nm high gold disk is placed on a SiO_2 glass substrate in the center of the space. The diameter of the disk is varied between 20 and 200 nm. A light source injects a plane wave from 25 nm above the disk and subtracted 25 nm after it has passed the disk, leaving only scattered light past these points. A scattering monitor is placed at 30 nm above and below the nanoparticle to study the near-field of the particle. The monitor is 270 nm wide to completely surround the nanoparticle. Similarly, an absorption monitor is placed between the light source and the nanoparticle, detecting incident light on one side and transmitted and scattered light on the other, giving

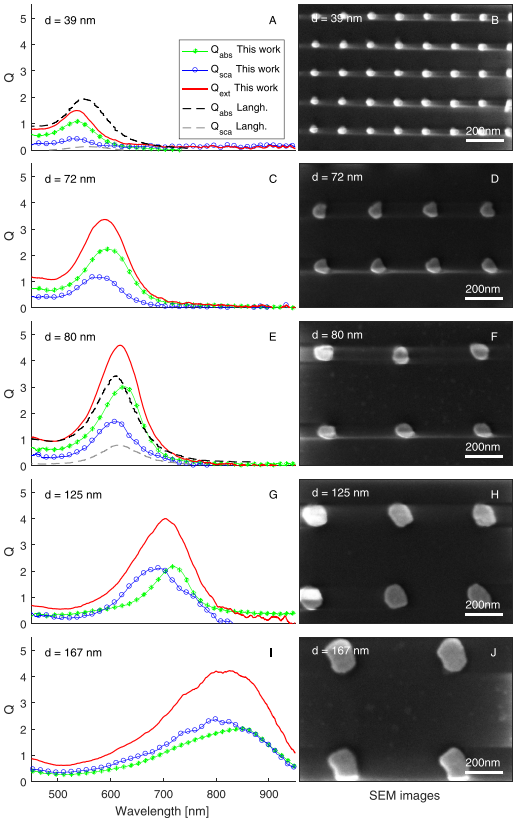

FIG. 2. (Color online) Measured extinction (red, solid line), absorption (green, asterisk marker) and scattering (blue, ring marker) efficiency of our fabricated arrays. For (a) and (e), measured values of gold nanoparticle arrays presented by Langhammer *et al.* (Ref. 11) is included for arrays of 38 and 76 nm (dashed black and gray lines). Those results are of relevance as the method of fabrication (HCL) is different, but the samples are also investigated using integrating spheres, measuring the scattering and absorption efficiency. In the right column, SEM images of a few of the nanoparticles from each sample are shown. Note that the images are captured under charging conditions, as we deliberately did not coat the samples.

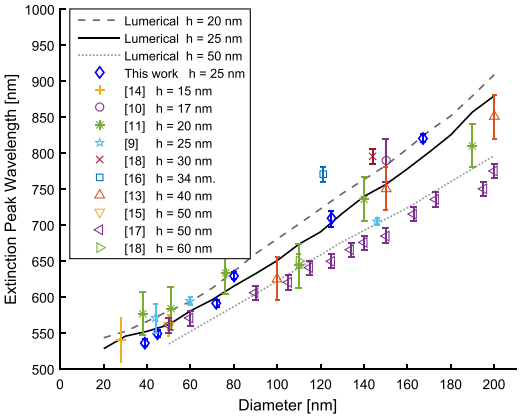

FIG. 3. (Color online) LSPR extinction peak resonance wavelength plotted against the gold nanoparticle diameter, for this experimental and theoretical work and several other sources in the literature (Refs. 11 and 13–18).

the net difference, i.e., the absorption. Reflection and transmission of the bare substrate is assumed to be negligible. The mesh size is set to be 3 nm for diameters 200–160 nm, 2 nm for the 150–90 nm diameter, 1.5 nm for 80 nm–60 nm, and 1 nm for 50–20 nm. The different mesh sizes are selected for efficient simulation time with sufficient accuracy. A field time monitor is included to record the time evolution of the electromagnetic fields, to ensure that the fields have enough time to decay before the maximum simulation time is reached. The light source covers wavelengths from 400– to 1050 nm. As no information about polarization can be extracted from the integrating sphere setup, the polarization is not considered in the simulation.

III. RESULTS AND DISCUSSION

A. Optical properties

In Figs. 2(a), 2(c), 2(e), 2(g), and 2(l), the measured extinction, scattering, and absorption of the nanoparticle arrays are presented. The contribution from the glass substrate has been removed by subtracting the corresponding spectrum measured on the same glass substrate, close to the nanoparticles (see Sec. II B). The nanoparticle extinction, scattering, and absorption efficiency spectra (Q_{ext}, Q_{sca}, and Q_{abs}) are plotted. For each fabricated array, a high magnification SEM image is included. All SEM images are acquired using the same magnification so that the area coverage and nanoparticle spacing can be easily evaluated. Note that the somewhat poor SEM image quality is due to the insulating nature of the substrate resulting in charging effects seen as brightness/contrast variation across the sample. In addition, data from the HCL gold nanoparticle samples presented by Langhammer *et al.*,[11] also studied using an integrating sphere, are included for comparison where a sufficient overlap in nanoparticle sizes are found. We will refer to this paper simply as Langhammer for the rest of this paper. The two samples of Langhammer having a diameter of 38 and 76 nm were sufficiently close to our 39 and 80 nm nanoparticle diameters. These four samples are presented together in Figs. 2(a) and 2(e). Comparing the results, it is seen that for the 38 nm nanoparticles, Langhammer measures an absorption efficiency which has a broader and slightly red-shifted center wavelength. Langhammer states that the standard deviation of the size distribution for the 38 nm nanoparticles is 20%, much larger than in our experiment, and hence the broader peak. The slight redshift can be explained as a coupling between some of the particles, which will give a shift toward higher wavelengths: To confirm this, we performed an image analysis of the SEM image provided by Langhammer (using the software ImageJ). We found an average particle diameter of 39 nm, a minimum size of 19 nm, and a maximum size of 54 nm. This is in good agreement with what Langhammer states. Based on the area coverage, the average distance between nanoparticles is 115 nm. This is about three times the particle diameter, sufficient to avoid near-field (interparticle) coupling. However, it should be noted that our image analysis revealed that some particles are only 80 nm apart, and for such closely spaced particles, interparticle coupling is expected.[10] The scattering efficiency of Langhammer similarly shows a redshift and is found to have a lower amplitude, as expected for coupled particles.[28]

For our 80 nm nanoparticles, we find that the peak is slightly narrower and shifted toward longer wavelengths compared to the 76 nm sample of Langhammer. This is considered a good agreement considering our slightly larger particle sizes, and that Langhammer uses a particle height of 20 nm compared to our height of 25 nm. The standard deviation of the size distribution for the 76 nm sample is stated to be less than 5%, which is slightly smaller than ours. Langhammer does not provide any SEM images of the larger gold nanoparticle samples, so we cannot check for any near-field coupling effects. However, the experiments do not indicate any. The scattering efficiency shows similar trends, but for our array, the scattering amplitude is higher. Also, we see slightly more scattering at shorter wavelengths.

Focusing on our samples 39, 72, and 80 nm [see Figs. 2(a), 2(c), 2(e)], it is found that the light absorption dominates over scattering. This is expected for particles smaller than 100 nm.[24] The minor rise in absorption efficiency at shorter wavelengths is attributed to interband transitions. Also, it can be seen that the scattering efficiency has some contribution at shorter wavelengths. This is somewhat unexpected as interband transition should only lead to absorption of light. Similar effects can be seen for Langhammer. It is however less pronounced which could be due to a lower signal. We speculate that the particles exhibit an increase scattering efficiency at shorter wavelengths, causing this effect. For the 125 and 167 nm nanoparticle samples [Figs. 2(g) and 2(i)], it is worth noting that the extinction efficiency is seen to broaden for the increasing particle size. The extinction peak wavelength is seen to red shift with increasing particle size as expected for a single particle.[17,25] The scattering efficiency can be seen to increase and finally becomes dominating. In an array of nanoparticles, near-field and far-field coupling must also be considered to contribute to the optical properties. The interparticle distance is equal to or greater than three times the particle diameter in all of the fabricated samples, which is sufficient to avoid near-field coupling.[10] However, as the particle diameter increases, so does the interparticle distances. For the increasing interparticle distances, far-field coupling will become increasingly evident. For such arrays, the scattered light of the nanoparticles will give rise to additional diffraction effects.[26,27] This far-field coupling has been shown to alter the measured extinction spectra by shifting the center peak position and its amplitude as a function of the nanoparticle periodicity.[27] For the 125 nm nanoparticle array, this is first of all seen as a broadening of the extinction efficiency. Measuring the nanoparticle absorption and scattering efficiency, this reveals, somewhat surprisingly, that the center wavelengths of the two does not coincide. We try to explain this as follows: first, we consider the absorption spectrum to mainly be a measure of the particle properties and near-field effects, whereas the scattering spectrum is affected by the far-field. The absorption spectrum will therefore exhibit single-particle-like optical properties, for these noninteracting nanoparticle arrays. The scattering spectrum on the other hand will contain the single

particle properties, strongly influenced by any far-field effects. This is evident as a blue shifted and broadened scattering spectrum, with respect to the absorption spectrum. Studying the extinction spectrum compares well with the findings of Lamprecht *et al.*[27] for a interparticle spacing of 450 nm.

Bearing the 125 nm sample in mind, one would expect a similar result for the 167 nm nanoparticle array, which turns out not to be the case. The center wavelength of the scattering and absorption spectra does not coincide. The scattering exhibits the expected broad shape, but the absorption is found to be much broader than expected from the above argument. This can likely be explained by the elliptical shape of the 167 nm nanoparticles which will give rise to the much broader absorption peak. Considering the extinction spectra, we can again see that an interparticle distance of about 600 nm should lead to a significant broadening of the LSPR due to far-field interaction.

Overall, the highest scattering and absorption efficiency is found for the 80 nm sample. For the largest diameters [125 and 167 nm, see Figs. 2(g) and 2(i)], both the scattering and absorption efficiency are seen to increasingly broaden. This is caused by the accumulative effect of (1) increasing particle diameter and size distribution and (2) far-field coupling, as discussed earlier.

B. Extinction peaks

As mentioned earlier, most investigations on lithography fabricated metal nanoparticles have been focused on measuring the extinction spectra to determine the center position of the extinction peak (the maximum position of the spectrum). In Fig. 3, we show the extinction peaks obtained in this work together with results previously published in the literature.[11,13–18] In addition, we have included new simulation results. The simulated peak position for gold nanoparticles ranging in diameters from 20 to 200 nm is presented for three nanoparticle heights, 20, 25, and 50 nm. Good agreement can be seen for all experimental data included in this work and our simulated results. We find a near linear relationship between the nanoparticle diameter and the LSPR wavelength for the fixed nanoparticle height, where the slope is depending on the nanoparticle height.

IV. SUMMARY AND CONCLUSION

In summary, we have fabricated large arrays of gold nanoparticles by means of EBL with diameters in the range 39 ± 4 to 167 ± 15 nm and interparticle distances equal to or greater than three times the particle diameter. The optical properties of the arrays were investigated using an integrating sphere setup, which allows us to measure the light absorption and scattering. We compare a set of samples with hole mask colloidal lithography fabricated nanoparticle samples where the optical properties were also studied using integrating spheres. We find a good agreement.

For the larger nanoparticle diameters (125 and 167 nm), the scattered light gives rise to additional diffraction effects due to the increased interparticle distances (grating period). These effects alter the measured optical properties significantly. However, measuring the absorption and scattering allow us to navigate these unexpected results. We can distinguish far-field effect from the absorption, which shows the expected optical properties of a noninteracting single nanoparticle. Using ordered arrays will give rise to such effects in the far-field, which can be avoided by using nonordered arrays achieved by, e.g., HCL.

Finally, we present extinction measurements as a function of the nanoparticle diameter, which we compare to results on EBL and HCL fabricated nanoparticle arrays already published in the literature. These plots are supported by simulations, which agree well with the experimental results.

ACKNOWLEDGMENT

Ranveig Flatabø gratefully acknowledges the support from the Bergen Research Foundation. The authors also thank the reviewers for their fruitful feedback.

[1]C. L. Haynes and R. P. Van Duyne, J. Phys. Chem. B **105**, 5599 (2001).
[2]C. L. Nehl, H. Liao, and J. H. Hafner, Nano Lett. **6**, 683 (2006).
[3]O. Nicoletti, F. Pena, R. K. Leary, D. J. Holland, C. Ducati, and P. A. Midgley, Nature **502**, 80 (2013).
[4]M. W. Knight, H. Sobhani, P. Nordlander, and N. J. Halas, Science **332**, 702 (2011).
[5]K. M. Mayer and J. H. Hafner, Chem. Rev. **111**, 3828 (2011).
[6]M. Tu, T. Sun, and K. Grattan, Sens. Actuator, B **164**, 43 (2012).
[7]V. R. A. Holm, M. M. Greve, and B. Holst, J. Vac. Sci. Technol., B **34**, 06K501 (2016).
[8]K. A. Willets and R. P. V. Duyne, Annu. Rev. Phys. Chem. **58**, 267 (2007).
[9]M. M. Greve, T. O. Håvardstun, and B. Holst, J. Vac. Sci. Technol., B **31**, 06F410 (2013).
[10]W. Rechberger, A. Hohenau, A. Leitner, J. Krenn, B. Lamprecht, and F. Aussenegg, Opt. Commun. **220**, 137 (2003).
[11]C. Langhammer, B. Kasemo, and I. Zorić, J. Chem. Phys. **126**, 194702 (2007).
[12]M. M. Greve and B. Holst, J. Vac. Sci. Technol., B **31**, 043202 (2013).
[13]T. Temple and D. Bagnall, J. Appl. Phys. **109**, 084343 (2011).
[14]G. Niklasson and H. Craighead, Thin Solid Films **125**, 165 (1985).
[15]X. Wang, P. Gogol, E. Cambril, and B. Palpant, J. Phys. Chem. C **116**, 24741 (2012).
[16]G. Bi, L. Wang, C. Cai, K. Ueno, H. Misawa, and J. Qiu, J. Mod. Opt. **61**, 1231 (2014).
[17]J. Grand, P.-M. Adam, A.-S. Grimault, A. Vial, M. Lamy de la Chapelle, J.-L. Bijeon, S. Kostcheev, and P. Royer, Plasmonics **1**, 135 (2006).
[18]N. Félidj, J. Aubard, G. Lévi, J. R. Krenn, M. Salerno, G. Schider, B. Lamprecht, A. Leitner, and F. R. Aussenegg, Phys. Rev. B **65**, 075419 (2002).
[19]E. Babich, S. Scherbak, F. Heisler, S. Chervinskii, A. Samusev, and A. Lipovskii, J. Phys.: Conf. Ser. **769**, 012040 (2016).
[20]T. Hoang, G. Akselrod, C. Argyropoulos, J. Huang, D. Smith, and M. Mikkelsen, Nat. Commun. **6**, 1 (2015).
[21]B. M. Reinhard, M. Siu, H. Agarwal, A. P. Alivisatos, and J. Liphardt, Nano Lett. **5**, 2246 (2005).
[22]B. Lahiri, R. Dylewicz, R. M. D. L. Rue, and N. P. Johnson, Opt. Express **18**, 11202 (2010).
[23]R. Flatabø, A. Coste, and M. Greve, J. Microsc. **265**, 287 (2017).
[24]C. F. Bohren and D. R. Huffman, *Absorption and Scattering of Light by Small Particles* (Wiley-VCH, Germany, 2007).
[25]A. Moroz, J. Opt. Soc. Am., B **26**, 517 (2009).
[26]M. Meier, A. Wokaun, and P. Liao, J. Opt. Soc. Am., B **2**, 931 (1985).
[27]B. Lamprecht, G. Schider, R. Lechner, H. Ditlbacher, J. Krenn, A. Leitner, and F. Aussenegg, Phys. Rev. Lett. **84**, 4721 (2000).
[28]J. R. Kenn, A. Dereux, J. C. Weeber, E. Bourillot, Y. Lacroute, and J. P. Goudonnet, Phys. Rev. Lett. **82**, 2590 (1999).

Atom sieve for nanometer resolution neutral helium microscopy

Ranveig Flatabø[a)]
Department of Physics and Technology, University of Bergen, Allegaten 55, 5007 Bergen, Norway and Research Laboratory of Electronics, Massachusetts Institute of Technology, Massachusetts 02139

Martin M. Greve and Sabrina D. Eder
Department of Physics and Technology, University of Bergen, Allegaten 55, 5007 Bergen, Norway

Matthias Kalläne
Institute for Experimental and Applied Physics, University of Kiel, Leibnizstrasse 19, 24098 Kiel, Germany and Ruprecht Haensel Laboratory, University of Kiel and DESY, 24118 Kiel, Germany

Adrià Salvador Palau
Department of Engineering, Institute for Manufacturing, University of Cambridge, Cambridge CB30FS, United Kingdom

Karl K. Berggren
Research Laboratory of Electronics, Massachusetts Institute of Technology, Massachusetts 02139

Bodil Holst[b)]
Department of Physics and Technology, University of Bergen, Allegaten 55, 5007 Bergen, Norway

(Received 5 July 2017; accepted 9 August 2017; published 24 August 2017)

Neutral helium microscopy is a new tool for imaging fragile and/or insulating structures as well as structures with large aspect ratios. In one configuration of the microscope, neutral helium atoms are focused as de Broglie matter waves using a Fresnel zone plate. The ultimate resolution is determined by the width of the outermost zone. Due to the low-energy beam (typically less than 0.1 eV), the neutral helium atoms do not penetrate solid materials and the Fresnel zone plate therefore has to be a free-standing structure. This creates particular fabrication challenges. The so-called Fresnel photon sieve structure is especially attractive in this context, as it consists merely of holes. Holes are easier to fabricate than the free-standing rings required in a standard Fresnel zone plate for helium microscopy, and the diameter of the outermost holes can be larger than the width of the zone that they cover. Recently, a photon sieve structure was used for the first time, as an atom sieve, to focus a beam of helium atoms down to a few micrometers. The holes were randomly distributed along the Fresnel zones to suppress higher order foci and side lobes. Here, the authors present a new atom sieve design with holes distributed along the Fresnel zones with a fixed gap. This design gives higher transmission and higher intensity in the first order focus. The authors present an alternative electron beam lithography fabrication procedure that can be used for making high transmission atom sieves with a very high resolution, potentially smaller than 10 nm. The atom sieves were patterned on a 35 nm or a 50 nm thick silicon nitride membrane. The smallest hole is 35 nm, and the largest hole is 376 nm. In a separate experiment, patterning micrometer-scale areas with hole sizes down to 15 nm is demonstrated. The smallest gap between neighboring holes in the atom sieves is 40 nm. They have 47011 holes each and are 23.58 μm in diameter. The opening ratio is 22.60%, and the Fresnel zone coverage of the innermost zones is as high as 0.68. This high-density pattern comes with certain fabrication challenges, which the authors discuss. © *2017 American Vacuum Society*. [http://dx.doi.org/10.1116/1.4994330]

I. INTRODUCTION

The first neutral helium microscopy images were published in 2008.[1] Several groups have worked on the technique.[2–6] In a neutral helium microscope, a beam of neutral helium atoms with narrow velocity (wavelength) distribution is used to image a sample. An image is obtained by measuring either the reflected or transmitted signal as the beam is scanned across the sample. The energy of the beam is less than 0.1 eV for a wavelength of 0.1 nm, which means that the atoms probe the outermost electron density distribution of the sample without penetrating into the solid material.[7] These properties make neutral helium microscopy particularly suitable for the investigation of fragile and/or insulating surfaces as well as high aspect ratio structures. Recently, it was shown that helium microscopy can distinguish between different metal films on an insulating substrate.[5] However, the big challenge is to create a high-resolution microscope, partly because the focusing element must be of the binary type with either completely transparent or completely opaque areas.

Helium-atom focusing with a binary Fresnel zone plate was first carried out by Carnal *et al.* using a beam of metastable helium atoms.[8] The first focusing of a neutral, ground state helium beam with a zone plate was carried out by

[a)]Electronic mail: ranveig.flatabo@uib.no
[b)]Electronic mail: bodil.holst@uib.no

Doak *et al.*[9,11] Currently, the best zone plates made for helium microscopy have a nominal outermost zone width of 50 nm.[10]

The Beynon–Gabor zone plate, which is also binary, has been suggested as an alternative candidate for focusing helium atoms.[12] The main advantage of the Beynon–Gabor zone plate is that it has no higher-order foci. Unfortunately, it is very challenging to fabricate. In 2015, a new optical diffraction element, the atom sieve, was introduced and used to focus helium atoms down to 3.6 μm.[13] The atom sieve is a direct analog to the photon sieve, which was invented in 2001 for applications with soft x-rays.[14] It consists of holes of varying diameters, arranged across the Fresnel zones in such a manner that it is possible to focus to a spot with a diameter smaller than the smallest hole. In addition, higher-order diffraction and secondary maxima can be suppressed. There are several advantages of the atom sieve. First, it is easier to fabricate free-standing holes than free-standing ring segments as no support structure is needed. Moreover, the design can be tuned so that the diameter of the outermost hole is larger than the width of the outermost zone that it covers. In contrast, the minimum structure size of a first order Fresnel zone plate is limited by the width of the outermost zone.[27] A higher resolution can be obtained by using higher order foci, but this comes with a significant reduction in intensity. For a standard Fresnel zone plate, 10.1 % of the incident beam goes into the first order focus and only 1.1% into the third order.[17] For an atom Fresnel zone plate, these numbers are further reduced due to the support rods needed to keep the zone plate ring structure together. Intensity is a big issue in helium microscopy,[15,16] and so this is a major limitation.

Here, we present a new high-transmission atom sieve design. This paper begins with an experimental section, where we first present the design requirements followed by the fabrication procedure. Then, the results and discussion section showing SEM images of the fabricated atom sieves and the first atom sieve transmission tests demonstrating that the structure is transparent to atoms is given. This paper finishes with the summary and conclusion.

II. EXPERIMENT

A. Atom sieve design considerations

In the original photon sieve work, suppression of higher order foci and side lobes was particularly important, and a Weber transmission window was used, giving holes randomly distributed along the zones.[14] This limits the number of holes and hence the open area ratio (total transmissivity). The first atom sieve used the original photon sieve design and had an opening ratio (total transmissivity) of 9.22% only, giving a transmissivity of 1.86% of the incident beam into the first order focus.[13] For the neutral helium microscope, it is crucial to ensure maximum intensity in the first order focus, as discussed in the introduction. For this reason, we changed the design of the atom sieve and used a transmission window similar to a rectangular shaped window, but with increasing transmission toward the center, to fit as many holes as possible in each zone based on a predefined minimum gap. The minimum gap is discussed below. By doing so, the opening ratio of the sieve (total transmissivity) increases to 22.60% and the intensity in the first order focus is 4.57%.

Another important decision was to determine the hole size that could realistically be patterned. This is important not only for the resolution but also for the transmissivity, as it determines how large a zone plate can be made for a given focal length. The focal length was chosen so that it corresponds to a microscope that can be constructed and further that the velocity spread of the beam does not cause chromatic aberrations (see Ref. 15). The hole size varies from 376 to 35 nm. The smallest holes that have ever been made using direct-write lithography are around 1 nm in size. They were made using helium ion beam lithography.[18] Direct-write ion lithography is in principle an attractive technique for atom sieve patterns, as one can pattern directly on the membrane, i.e., no resist is needed. This enables a one-step fabrication process where the result can be examined *in situ*. Moreover, the backscattering contribution to the lithographic point spread function of light ions, such as helium and neon, is shown to be minimal, and hence, dose modifications might not be needed.[19,20] However, these are relatively new techniques with low throughput, limited stability, and in the case of helium ions, low sputtering yields.[21] Electron beam lithography, followed by reactive ion etching, was chosen as the method of fabrication, and an atom sieve pattern with a minimum hole size of 35 nm was realized. To ensure maximum transmissivity, the diameter of the holes was chosen to be the same as the zone widths. As discussed in the Introduction, it is possible to design a transmission function enabling the hole diameter to be larger than its zone, but this comes at the cost of intensity.

The aim is eventually to install the atom sieve in a new helium microscope, currently being designed. This determined a focal length of approximately 10 mm for a helium atom with a de Broglie wavelength of approximately 0.1 nm for the sieve. With a minimum hole size and focal length given, the sieve diameter could be calculated (the sieve diameter is 23.58 μm).

Finally, the gap between adjacent holes was selected. This is essential for the transmission of the device since large values reduce the number of holes. The gap between neighboring holes varies from 53 to 40 nm, depending on how many holes one can fit into one zone. Hence, the zones in the atom sieve have a very high zone coverage (i.e., exposed area in one Fresnel zone divided by the total area of the corresponding zone). The zone coverage of the innermost zone is 0.68 (corresponding to a hole diameter of 376 nm and a gap of 53 nm), and it slowly decreases to 0.39 for the outermost zone (for a 35 nm Fresnel zone overlaid with holes of 35 nm and a gap of 40 nm). The minimum gap of 40 nm was chosen as a safe value, making sure that it was possible to pattern separate holes using electron beam lithography and transfer the pattern into the membrane.

The atom sieve design is shown in Fig. 1. Note that it is not rotationally symmetrical. The stripe in the horizontal direction exists as the positioning of the holes starts at the same angle on each zone. Each zone is filled with as many holes as possible (with the given minimum hole distance).

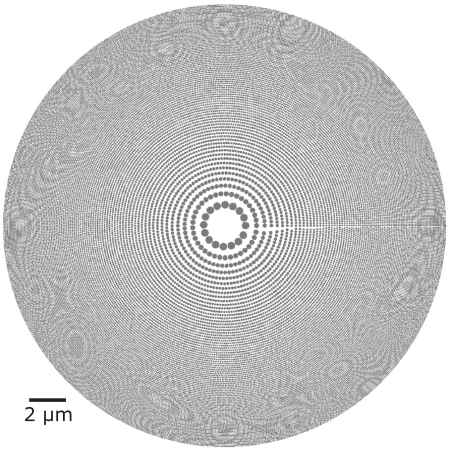

FIG. 1. Atom sieve design maximized for total transmissivity. The pattern is not symmetrical, which is discussed in the text. The central opaque area corresponds to the first zone, which is kept closed for stability reasons.

B. Fabrication procedure

The fabrication process is illustrated in Fig. 2. It shares some steps with the fabrication procedure used in Ref. 22, but with some modifications. In this work, we use 35 or 50 nm thick SiNx membranes with low stress (a low stress membrane was chosen to prevent the membrane from cracking). The membrane thicknesses were chosen to keep the aspect ratio of the etched holes adequate. However, it comes with the obvious trade-off of being more fragile than thicker membranes, which we discuss in Sec. III.

First, photolithography was used to pattern membrane windows on the backside of the SiNx/Si/SiNx wafer. To open the membrane windows, a dry etch step was performed using 15 SCCM (gas flow rate: standard cubic centimeters per minute) CF_4, 150 W, and 10 mTorr for 2 min. Then, the underlying silicon was etched using KOH (30% KOH in deionized water) at 80 °C, creating SiNx membranes.

As the resist, poly(methyl methacrylate) (PMMA) alone cannot withstand the reactive ion etching that creates free-standing holes, and the membrane was coated with an etch mask consisting of 110 nm antireflective coating (ARC), 10 nm SiO_x, and 60 nm PMMA (2% in anisole, 950 K). First, ARC was spin-coated onto the chip at 3000 rpm for 1 min and baked at 180 °C for 3 min. SiO_x of 10 nm was then deposited by means of electron beam evaporation. Finally, PMMA was spin-coated onto the sample at 3000 rpm for 1 min and baked at 180 °C for 3 min.

PMMA was exposed using 125 keV electrons (ELS-F125 Elionix), a current of 1 nA, and a step size of 2.5 nm. As the beam enters the resist, the electrons interact with the resist and the substrate and causes energy to be delivered to points different from the point of incidence, commonly known as proximity effects. Due to the high zone coverage of the atom sieve design (0.68–0.39), it is extremely sensitive to such unintended exposure, especially as the final structure needs to be free-standing. To find the correct dose (i.e., areal dose density), multiple atom sieves were patterned with a single exposure dose, analogous to the standard dose matrices. The innermost zones receive the largest dose per zone and get the largest amount of unintended exposure. This causes over-exposure. Therefore, the dose was linearly increased from 2.8 to 3.8 mC/cm^2 going from the innermost zone to the outermost zone (again using an electron beam of 125 keV, a current of 1 nA, and a step size of 2.5 nm). It should be noted that there are accurate and rigorous ways to calculate the correct dose needed in a pattern of high surface coverage.[23,28,29] However, a crucial part in this work is to transfer the pattern into the membrane, which also causes a minor hole broadening (discussed below), the correct doses were found by iteration.

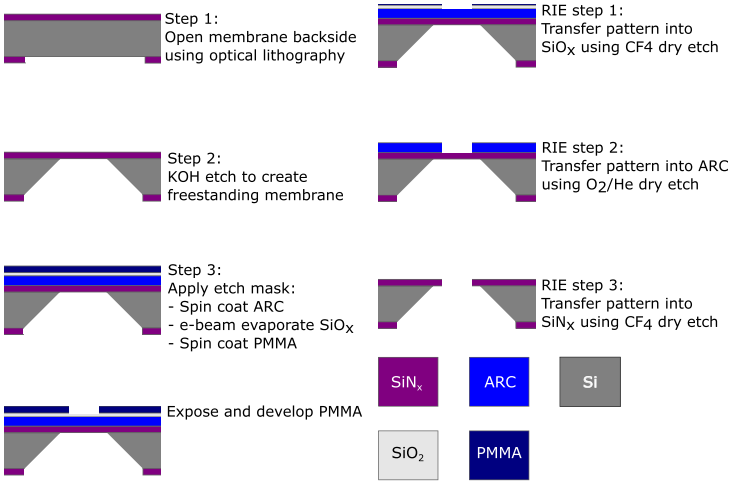

FIG. 2. (Color online) Step-by-step fabrication procedure for creating the free-standing membrane structure.

The sample was developed in 1:3 methyl isobutyl ketone:2-propanol at 0 °C for 30 s and dried using pressurized nitrogen. Cold development was chosen, as it has been found to improve feature quality and resolution.[24,25]

The pattern was transferred to the SiO_x-layer using 15 SCCM of CF_4 at 150 W and 10 mTorr. Pattern transfer into the ARC was done using 20 SCCM He and 10 SCCM of O_2 at 10 mTorr and 200 W. Finally, pattern transfer into the SiNx was done using 15 SCCM of CF_4 at 150 W and 10 mTorr. Reactive ion etching produces anisotropic etch profiles. Nevertheless, a broadening of about 5 nm in the diameter is found when comparing circles in an atom sieve that was not etched (i.e., atom sieve in PMMA) with holes in atom sieves. All SEM images are taken with an acceleration voltage of 3 kV, 3.9 mm working distance and 30 μm aperture, except for Fig. 7 where 10 kV, 10 mm working distance and an aperture of 30 μm was used.

III. RESULTS AND DISCUSSION

A. Atom sieve

Figure 3 shows an overview image of an atom sieve. The diameter of the sieve is 23.58 ± 0.01 μm, and it contains 47011 holes. Close-up SEM images are shown in Fig. 4. The holes of the innermost zone have a diameter of 378 ± 4 nm and the holes of the outermost zone 38 ± 4 nm. Both slightly too large and slightly too small holes will lead to a reduction in transmissivity into the first order focus because a too large hole will open up into the neighboring zone and give destructive interference. The overall deviation, taken for all holes, is so small that the reduction is likely to be negligible.[30] It is very important for the function of the atom sieve that the size of the holes and their position are correct to within a fraction of the Fresnel zone they cover since otherwise a hole will contribute with destructive interference.[30] In other words, the positioning of the small holes needs to be more accurate than the positioning of the big holes. In Fig. 5(a), the SEM image of the fabricated atom sieve (black holes) is superimposed with the design pattern (white "holes"). As can be seen, the positioning of even the smallest holes is accurate to within a fraction of the hole diameter.

The membrane thickness of 35 nm was chosen to keep the aspect ratio of the etched holes adequate. However, this comes with a trade-off of being more fragile than a thicker membrane. The 35-nm thick membranes easily broke due to handling or transport. An improvement in stability was seen when using a membrane thickness of 50 nm.

In a separate experiment, it was desirable to investigate the smallest diameter hole-sizes. A lower hole density and a random hole distribution were selected for these test experiments, as illustrated in Fig. 6. The diameter of the holes in the SEM image ranges from 25 to 15 nm.

B. Atom transmission tests

Ultimately, the atom sieve will be integrated in a new neutral helium atom microscope instrument. However, prior

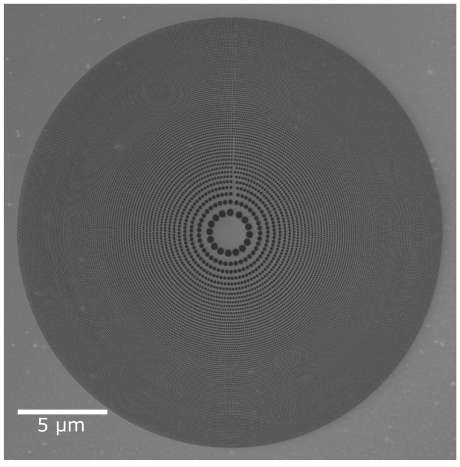

FIG. 3. Overview SEM image of the fabricated free-standing atom sieve.

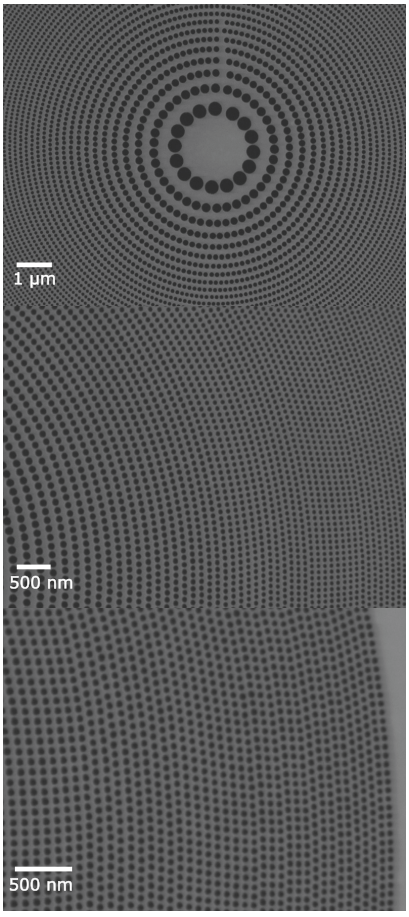

FIG. 4. Close-up SEM images of a free-standing atom sieve. The holes of the innermost zone have a diameter of 378 ± 4 nm, and the holes of the outermost zone have a diameter of 38 ± 4 nm.

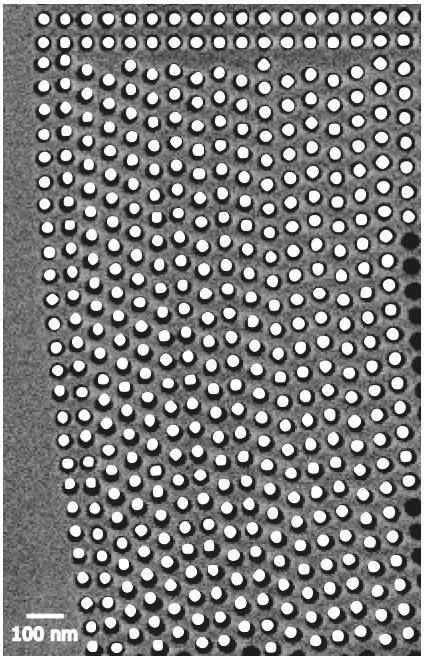

FIG. 5. Overview SEM image of the free-standing atom sieve where the design pattern is superimposed onto the image. The design-holes are white, while the underlying SEM image consists of black holes.

to that, we wanted to check if it is transmissive to atoms. This is crucial because in order to be a functional atom sieve, the holes must be free standing. It can be difficult to evaluate just by optical inspection or inspection in a SEM if all material has been removed. This is illustrated in Fig. 7, where a 20 μm circle on a SiNx membrane appears to be fully etched but in fact is not. For this reason, we installed the atom sieve as a sample in our existing helium microscope[26] and measured the overall transmissivity by sending a 20 μm helium beam onto the sample. At present, the minimum resolution in our helium microscope is only around 5 μm, and so, it was not possible to perform a detailed mapping. Figure 8 presents

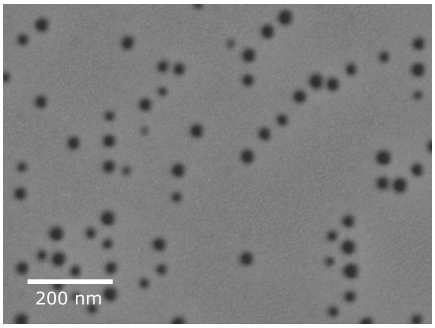

FIG. 6. Free-standing holes with a diameter ranging from 25 to 15 nm.

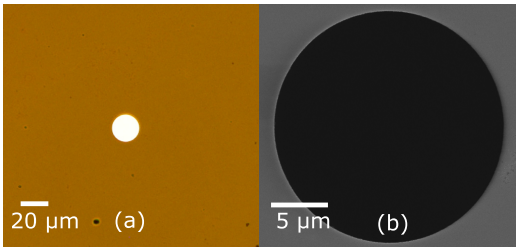

FIG. 7. (Color online) (a) Transmission optical microscopy image and (b) SEM image of a 20 μm circle in a 200 nm thick SiNx membrane that appears to be free-standing. However, transmission helium atom microscopy measurements revealed that the structure was not etched through.

a line scan of the sieve. The transmissivity is normalized to the intensity measured when no sample is present (i.e., 100% signal), and the background has been subtracted. The transmissivity of the sieve is found to be 23.8% $\pm$ 3%, in good agreement with the nominal transmissivity of 22.6%.

IV. SUMMARY AND CONCLUSION

We have fabricated atom sieves, with a smallest hole diameter of 35 nm. The atom sieves were designed for maximum transmission so that the diameter of the smallest hole corresponds to the width of the outermost zone. This means that we have fabricated a zone plate which can be used to perform neutral helium microscopy with the resolution in the range of 35 nm. In addition, we have demonstrated writing of micrometer-scale areas with holes down to 15 nm in diameter. By using a transmission window where the hole areas are reduced in the outer parts, e.g., a Weber window, it is possible to design an atom sieve with a resolution larger than the hole diameter. In a recent paper, Palau *et al.*[16] showed that with the velocity spread and intensity of present day beam sources and present day detector technology, the limiting factor for a realistic helium microscope design is the resolution of the optical element, determined by the width of the outermost zone. Thus,

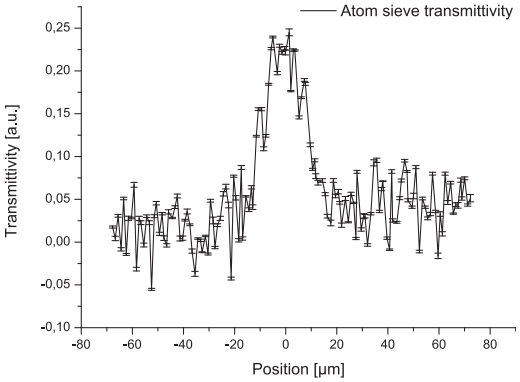

FIG. 8. Overall transmissivity of the atom sieve measured in the neutral helium microscope. The transmissivity of the sieve is found to be 23.8% $\pm$ 3%, in good agreement with the nominal transmissivity of 22.6%.

our work shows that helium microscopy with a resolution better than 15 nm should be possible.

ACKNOWLEDGMENTS

The authors thank M. Mondol, T. Savas, and J. Daley at the MIT Nanostructure Laboratory and B. Samelin at the University of Bergen Nanophysics Laboratory. This work was done at the MIT Nanostructure Laboratory and the MIT Scanning-Electron-Beam Lithography facility. The helium microscopy test was carried out at the University of Bergen, Nanophysics Laboratory. R. Flatabø gratefully acknowledges support from Bergen Research Foundation and the Norway-America Association through American-Scandinavian Foundation's Stolt-Nielsen Fund for education.

[1]M. Koch, S. Rehbein, G. Schmahl, T. Reisinger, G. Bracco, W. E. Ernst, and B. Holst, J. Microsc. **229**, 1 (2008).
[2]P. Witham and E. Sánchez, Rev. Sci. Instrum. **82**, 103705 (2011).
[3]P. Witham and E. Sánchez, Cryst. Res. Technol. **49**, 690 (2014).
[4]A. Fahy, M. Barr, J. Martens, and P. Dastoor, Rev. Sci. Instrum. **86**, 023704 (2015).
[5]M. Barr, A. Fahy, J. Martens, A. P. Jardine, D. J. Ward, J. Ellis, W. Allison, and P. C. Dastoor, Nat. Commun. **7**, 10189 (2016).
[6]P. Witham and E. Sánchez, J. Microsc. **248**, 223 (2012).
[7]G. Bracco and B. Holst, *Surface Science Techniques* (Springer Science & Business Media, Berlin, 2013).
[8]O. Carnal, M. Sigel, T. Sleator, H. Takuma, and J. Mlynek, Phys. Rev. Lett. **67**, 3231 (1991).
[9]R. B. Doak, R. E. Grisenti, S. Rehbein, G. Schmahl, J. P. Toennies, and C. Wöll, Phys. Rev. Lett. **83**, 4229 (1999).
[10]T. Reisinger, S. Eder, M. M. Greve, H. I. Smith, and B. Holst, Microelectron. Eng. **87**, 1011 (2010).
[11]R. Rehbein, J. Phys. IV France **104**, 207 (2003).
[12]M. M. Greve, A. Vial, J. Stamnes, and B. Holst, Opt. Express **21**, 28483 (2013).
[13]S. D. Eder, X. Guo, T. Kaltenbacher, M. M. Greve, M. Kalläne, L. Kipp, and B. Holst, Phys. Rev. A **91**, 043608 (2015).
[14]L. Kipp, M. Skibowski, R. L. Johnson, R. Berndt, R. Adelung, S. Harm, and R. Seemann, Nature **414**, 184 (2002).
[15]A. S. Palau, G. Bracco, and B. Holst, Phys. Rev A **95**, 013611 (2017).
[16]A. S. Palau, G. Bracco, and B. Holst, Phys. Rev A **94**, 063624 (2016).
[17]A. G. Michette, *Optical Systems for Soft X Rays* (Plenum, New York, 1986).
[18]D. A. Oulianov, R. A. Crowell, D. J. Gosztola, I. A. Shkrob, O. J. Korovyanko, and R. C. Rey-de-Castro, J. Appl. Phys. **101**, 053102 (2007).
[19]D. Winston *et al*., J. Vac. Sci. Technol., B **27**, 2702 (2009).
[20]D. Winston *et al*., Nano Lett. **11**, 4343 (2011).
[21]M. M. Marshall, J. Yang, and A. R. Hall, Scanning **34**, 101 (2012).
[22]J. O. Grepstad, M. M. Greve, T. Reisinger, and B. Holst, J. Vac. Sci. Technol., B **31**, 06F402 (2013).
[23]G. Owen, J. Vac. Sci. Technol., B **8**, 1889 (1990).
[24]W. Hu, K. Sarveswaran, M. Lieberman, and G. H. Bernstein, J. Vac. Sci. Technol., B **22**, 1711 (2004).
[25]B. Cord, J. Lutkenhaus, and K. K. Berggren, J. Vac. Sci. Technol., B **25**, 2013 (2007).
[26]S. D. Eder, A. K. Ravn, B. Samelin, G. Bracco, A. S. Palau, T. Reisinger, E. B. Knudsen, K. Lefmann, and B. Holst, Phys. Rev. A **95**, 023618 (2017).
[27]G. Schmahl, D. Rudolph, P. Guttman, and O. Chirst, "Zone plates for x-ray microscopy," in *X-Ray Microscopy*, Springer Series in Optical Sciences (Springer-Verlag, Berlin, 1984), Vol. 43.
[28]M. Peckerar, R. Bass, and K. W. Rhee, J. Vac. Sci. Technol., B **18**, 3143 (2000).
[29]M. Parikh, J. Appl. Phys. **50**, 4371 (1979).
[30]E. Hecht, *Optics*, 4th ed. (Addison-Wesley, San Francisco, 2001).

Fast resolution change in neutral helium atom microscopy

R. Flatabø,[1,a)] S. D. Eder,[1,b)] A. K. Ravn,[2] B. Samelin,[1] M. M. Greve,[1] T. Reisinger,[1,c)] and B. Holst[1]

[1]*Department of Physics and Technology, University of Bergen, Allégaten 55, 5007 Bergen, Norway*
[2]*Nanoscience Center, Niels Bohr Institute, University of Copenhagen, DK-2100 Copenhagen, Denmark*

(Received 13 March 2018; accepted 11 April 2018; published online 3 May 2018)

In neutral helium atom microscopy, a beam of atoms is scanned across a surface. Though still in its infancy, neutral helium microscopy has seen a rapid development over the last few years. The inertness and low energy of the helium atoms (less than 0.1 eV) combined with a very large depth of field and the fact that the helium atoms do not penetrate any solid material at low energies open the possibility for a non-destructive instrument that can measure topology on the nanoscale even on fragile and insulating surfaces. The resolution is determined by the beam spot size on the sample. Fast resolution change is an attractive property of a microscope because it allows different aspects of a sample to be investigated and makes it easier to identify specific features. However up till now it has not been possible to change the resolution of a helium microscope without breaking the vacuum and changing parts of the atom source. Here we present a modified source design, which allows fast, step wise resolution change. The basic design idea is to insert a moveable holder with a series of collimating apertures in front of the source, thus changing the effective source size of the beam and thereby the spot size on the surface and thus the microscope resolution. We demonstrate a design with 3 resolution steps. The number of resolution steps can easily be extended. *Published by AIP Publishing.*
https://doi.org/10.1063/1.5029385

I. INTRODUCTION

Thermal de Broglie matter wave beams created by supersonic expansions (free-jet expansions) have been used as a tool for surface science for several decades. Particularly helium has been used extensively in studies of surface diffraction and dynamics.[1–5] Due to helium's excellent properties, inertness and low energy (typically less than 0.1 eV) research has been ongoing in developing a new microscope using neutral helium atoms for imaging.[6–16] Currently the helium microscope exists in two configurations: In the pinhole microscope, the beam is collimated using a small pinhole and is scanned across the surface.[10] A theoretical treatment can be found in Ref. 17. In the second configuration, a zone plate is used to focus a helium beam. A theoretical treatment can be found in Ref. 18. The experiments presented here were all carried out using a zone plate helium microscope (Fig. 1).

For both helium microscope configurations, it has up till now not been possible to change the resolution without breaking the vacuum to exchange the collimating aperture (in the case of the pinhole microscope) or the skimmer (in the case of the zone plate microscope, see Fig. 1).

For the zone plate microscope, it is in principle possible to change the beam size on the sample by heating or cooling the beam. This changes the wavelength of the beam and hence the focal length of the zone plate.[19,20] Keeping the sample plane position fixed, this would result in a defocus and hence a larger spot size on the sample. The temperature of the source used in the experiments presented here can be changed from 110 K to 320 K,[21] corresponding to a wavelength change of around 0.4 Å and thereby a change in focal length of around 70 mm. However, by changing the wavelength, we also change the properties of the beam interacting with the surface and thereby potentially the imaging contrast. Furthermore it will typically take a minimum of several minutes to stabilize the beam at a new temperature. Therefore this is not a recommendable method.

II. THE DESIGN FOR FAST RESOLUTION CHANGE

In order to redesign our helium microscope for fast resolution change, we made an addition to the molecular beam source design described in detail in Ref. 21. The helium beam is created in a supersonic expansion from a reservoir through a nozzle into a vacuum. The central part of the beam is selected by a skimmer. For the experiments presented here, a reservoir pressure of $p_o = 61$ bars was used with a 5 ± 1 μm diameter nozzle and a 120 μm diameter skimmer, placed at 11.5 ± 0.5 mm from the nozzle. The beam was kept at a temperature of 310 K for all experiments. The beam is focused by a zone plate 192 μm in diameter with a 20 μm diameter central stop.[22] The zone plate is combined with an order-sorting aperture (20 μm diameter) as described in Ref. 23. The modified source design can be seen in Figs. 2 and 3. Instead of using a microskimmer which was used in previous focusing experiments,[23] a standard skimmer of 120 μm diameter (BEAM DYNAMICS, INC.) is used. This ensures that we get the beam flow expected from theoretical predictions for large skimmers, which is important as it was recently reported that the flow

a)R. Flatabø and S. D. Eder contributed equally to this work.
b)Author to whom correspondence should be addressed: sabrina.eder@uib.no
c)Present address: Karlsruhe Institute of Technology (KIT), Institute of Nanotechnology, Hermann-von-Helmholtz-Platz 1, 76344 Eggenstein-Leopoldshafen, Germany.

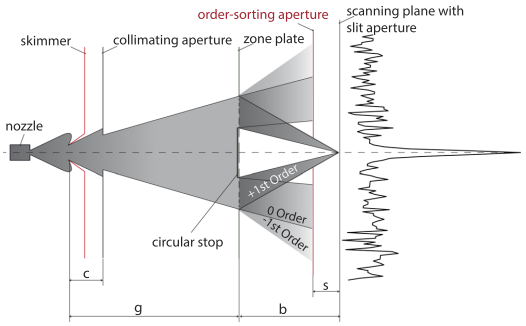

FIG. 1. Experimental setup: Following the free-jet beam expansion through a 5 μm diameter nozzle, the central part of the beam is selected by a 120 μm diameter skimmer. A movable collimating aperture holder located closely behind the skimmer collimates the beam further. With the *in situ* option of variable collimating aperture diameters (10 μm, 20 μm, and 50 μm), the effective source size of the beam can be adjusted without breaking the vacuum. The collimated beam is focused onto the sample by the zone plate (Fresnel type). An order-sorting aperture ensures that the zero-order part (and most of the higher orders) of the focused beam is filtered out. The focal spot size is determined by scanning a 10 μm slit aperture along the focal plane.

through microskimmers is reduced.[24] The source has been modified as follows: In front of the skimmer, two piezo electrical tables (Attocube, ANPx101/NUM/UHV) are placed on top of each other to provide x and y movements. On the top table, a 8 × 14 mm home made chip (see Fig. 2) with 3 collimating apertures in the sizes of 50.6 μm, 20.3 μm, and 10.2 μm is mounted. The apertures are placed as close to the skimmer as possible to maximize the flow without getting any reduction in intensity due to backscattering (distance from collimating aperture to skimmer opening is 28 ± 1 mm); see Figs. 2 and 3. Note how the mount for the collimating apertures is raised from the piezotable on a light construction (made of aluminium 6082-T6). This ensures a minimum heat transfer from the piezo tables which have an elevated temperature during operation (increased by the vacuum conditions) as well as a free expansion of the beam after it has passed through the collimating apertures. Figure 3 shows how the piezo tables are mounted in the chamber. The collimated beam is focused by the zone plate (see Fig. 1) onto the sample plane. For the experiments presented here, the beam was characterized by scanning a 10 ± 1 μm wide slit across the focused beam in 0.3 μm steps. The distance from the collimating aperture to the zone plate is 0.885 m [length (g)–(c) in Fig. 1] and the distance between the zone plate and the scanning plane is b = 0.207 m, giving a demagnification factor of M = 0.235 (see Fig. 1). The signal through the slit is measured using a so-called Pitot detector. In this type of accumulation detector, the pressure increase in a small volume is recorded with a sensitive cold cathode pressure measurement gauge (IKR-060 Pfeiffer). When the He-beam flow through a 1 mm diameter aperture into the detector accumulation volume is equal to the effusive flow back out of the accumulation volume, through the same entrance aperture, an equilibrium pressure can be measured. This equilibrium pressure can be directly related to the beam intensity.[21,23] The collimating apertures used here are between ca. 50 and 10 μm in diameter. These sizes were chosen to ensure that there is always enough signal in the Pitot detector to characterize the beam. With a more sensitive detector, smaller apertures can be used to obtain higher resolutions. We recently demonstrated that circular apertures down to 15 nm diameter can be made using electron beam lithography.[16] Apertures down to 1 nm have been made using helium ion lithography.[25] For the resolution limitation of helium microscopy see Refs. 17 and 18.

The apertures (holes) were fabricated on 200 nm thick silicon nitride membranes using electron beam lithography and reactive ion etching. The fabrication procedure is described in detail in Ref. 26. It is worth mentioning that the process was optimized slightly to ensure that the holes were etched through the SiN_x completely, using 15 SCCM CF_4 for 21 min at 10 mTorr and 100 W for the final etch step. The measured dimensions [scanning electron microscope (SEM)] were 50.6 μm, 20.3 μm, and 10.2 μm.

III. RESULTS

Figure 4 shows measurements of the focused beam for the 3 different collimating apertures. Note that the experimental

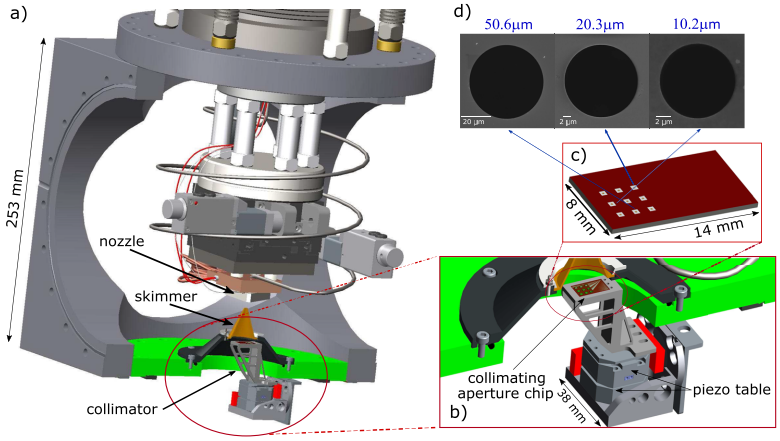

FIG. 2. CAD illustrations of the source setup with the variable collimating aperture element. (a) Overview showing the nozzle, skimmer, and collimating aperture arrangement. (b) Close up view illustrating the collimating aperture alignment: The two piezo tables placed on top of each other allow for x/y positioning of the collimating aperture chip. (c) 3D illustration of the collimating aperture chip. The chip has 9 different SiN_x membrane windows, each of them holding a different diameter collimating aperture. For this experiment, just three collimating apertures were used. (d) SEM images of the collimating apertures.

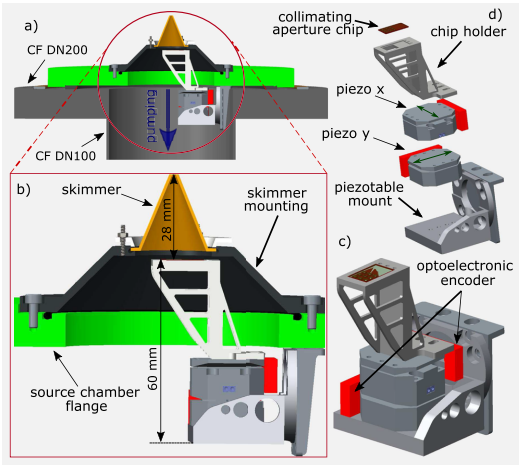

FIG. 3. CAD illustration of the collimating aperture mount. (a) Overview. (b) Close up view. The collimating aperture chip is mounted in a raised position. (c) 3D illustration of the collimating aperture chip arrangement showing the piezotable mount which holds the two piezo tables for x/y alignment of the collimating apertures as well as the mounting of the collimating aperture chip. (d) Explosion sketch of the collimating aperture chip arrangement.

data were recorded by scanning a 10 ± 1 μm slit aperture over the focus spot in the focal plane, and hence the measurements are a convolution of the real focus spot size with the 10 μm slit. To determine the measured focus spot diameters, an error function fit was performed.[12] The focus spot diameters are d_{c10} = 2.3 ± 0.5 μm, d_{c20} = 4.7 ± 0.5 μm and d_{c50} = 10.2 ± 0.5 μm. These values correspond to the expected focal spot diameters, given the demagnification factor of the instrument M = 0.235, and present a successful resolution change by a factor 4.4. There is a slight deviation for the 50 μm aperture where, according to the demagnification factor, one would expect

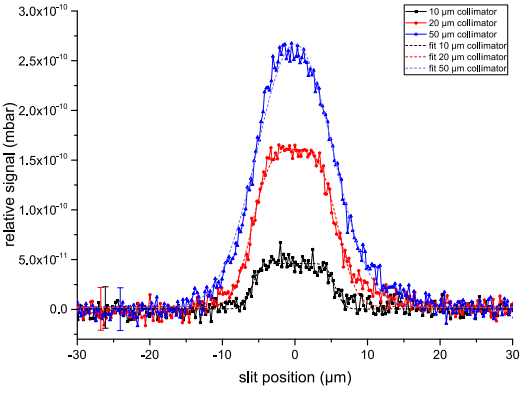

FIG. 4. Experimental scan results presenting line scans of a 10 μm slit aperture over the varying focal spot diameters from different collimating aperture sizes. Note: the focal spot diameter is convoluted with the 10 μm slit due to the measurement procedure. Error function fits to determine the real focus diameters from the measurements are presented as dashed lines. The focal spot diameters are d_{c10} = 2.3 ± 0.5 μm, d_{c20} = 4.7 ± 0.5 μm, and d_{c50} = 10.2 ± 0.5 μm in excellent agreement with a demagnification factor of 0.235.

11.7 μm. This is due to the fact that the supersonic expansion gives an intensity distribution that does not illuminate the 50 μm aperture uniformly. The intensity profiles in supersonic expansions have been investigated in a range of measurements; see for example, Refs. 27 and 28. Note that all measured curves have been background corrected. A final point to note is that the intensity in the focus from the 20 μm collimating aperture is exactly 4 times as high as for the focus from the 10 μm collimating aperture. This was measured in a separate experiment where the total transmitted focus intensity was recorded without a slit aperture. This indicates that for the beam parameters used here there is no beam attenuation due to backscattering from the collimator plate.

IV. SUMMARY AND CONCLUSION

In this paper we present a modified design of a supersonic helium source, which can be used in helium microscopes to provide fast, stepwise resolution change in analogy to the turret used for optical microscopy. We demonstrate three resolution steps with a factor 4.4 resolution change and with focused spot sizes ranging from 10.2 down to 2.3 μm. The design can easily be extended to include more resolution steps and yield smaller foci. In principle, foci (resolutions) down to the nanometer range are possible. In practice, the possible focus sizes will depend on factors such as the beam intensity, chromatic aberration, and detector efficiency.

ACKNOWLEDGMENTS

We gratefully acknowledge support from Bergen Research Foundation with Trond Mohn. S.D.E. has received funding from The Research Council of Norway through a FRIPRO (FRICON) Mobility Grant (Contract No. 250018/F20) which is co-funded by the European Union's Seventh Framework Programme for research, technological development, and demonstration under Marie Curie Grant Agreement (No. 608695).

[1]G. Bracco and B. Holst, *Surface Science Techniques* (Springer, 2013).
[2]S. D. Eder, K. Fladischer, S. R. Yeandel, A. Lelarge, S. C. Parker, E. Søndergård, and B. Holst, Sci. Rep. **5**, 14545 (2015).
[3]D. Farías, H. Tröger, and K. Rieder, Surf. Sci. **331-333**(Part A), 150 (1995).
[4]A. A. Taleb and D. Farías, J. Phys.: Condens. Matter **28**, 103005 (2016).
[5]R. D. Brown, Z. M. Hund, D. Campi, L. E. O'Leary, N. S. Lewis, M. Bernasconi, G. Benedek, and S. J. Sibener, J. Chem. Phys. **141**, 024702 (2014).
[6]R. B. Doak, R. E. Grisenti, S. Rehbein, G. Schmahl, J. P. Toennies, and Ch. Wöll, Phys. Rev. Lett. **83**, 4229 (1999).
[7]B. Holst and W. Allison, Nature **390**, 244 (1997).
[8]K. Fladischer, H. Reingruber, T. Reisinger, V. Mayrhofer, W. E. Ernst, A. E. Ross, D. A. MacLaren, W. Allison, D. Litwin, J. Galas, S. Sitarek, P. Nieto, D. Barredo, D. Farías, R. Miranda, B. Surma, A. Miros, B. Piatkowski, E. Søndergård, and B. Holst, New J. Phys. **12**, 033018 (2010).
[9]M. Barr, A. Fahy, J. Martens, A. P. Jardine, D. J. Ward, J. Ellis, W. Allison, and P. C. Dastoor, Nat. Commun. **7**, 10189 (2016).
[10]M. Barr, A. Fahy, A. Jardine, J. Ellis, D. Ward, D. MacLaren, W. Allison, and P. Dastoor, Nucl. Instrum. Methods Phys. Res., Sect. B **340**, 76 (2014).
[11]M. Koch, S. Rehbein, G. Schmahl, T. Reisinger, G. Bracco, W. E. Ernst, and B. Holst, J. Microsc. **229**, 1 (2008).
[12]S. D. Eder, T. Reisinger, M. M. Greve, G. Bracco, and B. Holst, New J. Phys. **14**, 073014 (2012).
[13]T. Reisinger and B. Holst, J. Vac. Sci. Technol., B **26**(6), 2374 (2008).
[14]P. Witham and E. Sánchez, Rev. Sci. Instrum. **82**, 103705 (2011).

[15]S. D. Eder, X. Guo, T. Kaltenbacher, M. M. Greve, M. Kalläne, L. Kipp, and B. Holst, Phys. Rev. A **91**, 043608 (2015).
[16]R. Flatabø, M. M. Greve, S. D. Eder, M. Kalläne, A. S. Palau, K. K. Berggren, and B. Holst, J. Vac. Sci. Technol., B **35**, 06G502 (2017).
[17]A. S. Palau, G. Bracco, and B. Holst, Phys. Rev. A **94**, 063624 (2016).
[18]A. Salvador Palau, G. Bracco, and B. Holst, Phys. Rev. A **95**, 013611 (2017).
[19]A. G. Michette, in *Optical Systems for Soft X Rays*, edited by A. Michette (Plenum Press, New York, 1968).
[20]O. Carnal and J. Mlynek, Phys. Rev. Lett. **66**, 2689 (1991).
[21]S. D. Eder, B. Samelin, G. Bracco, K. Ansperger, and B. Holst, Rev. Sci. Instrum. **84**, 093303 (2013).
[22]T. Reisinger, S. Eder, M. M. Greve, H. Smith, and B. Holst, Microelectron. Eng. **87**, 1011 (2010).
[23]S. D. Eder, A. K. Ravn, B. Samelin, G. Bracco, A. S. Palau, T. Reisinger, E. B. Knudsen, K. Lefmann, and B. Holst, Phys. Rev. A **95**, 023618 (2017).
[24]A. Salvador Palau, S. D. Eder, T. Andersen, A. K. Ravn, G. Bracco, and B. Holst, "Centre line intensity of a supersonic helium beam" (unpublished).
[25]D. Emmrich, A. Beyer, A. Nadzeyka, S. Bauerdick, J. C. Meyer, J. Kotakoski, and A. Gölzhäuser, Appl. Phys. Lett. **108**, 163103 (2016).
[26]J. O. Grepstad, M. M. Greve, T. Reisinger, and B. Holst, J. Vac. Sci. Technol., B **31**, 06F402 (2013).
[27]S. D. Eder, G. Bracco, T. Kaltenbacher, and B. Holst, J. Phys. Chem. A **118**, 4 (2014).
[28]T. Reisinger, G. Bracco, S. Rehbein, G. Schmahl, W. E. Ernst, and B. Holst, J. Phys. Chem. A **111**, 12620 (2007).

Part III

Appendices

Appendix A

Neon-ion-beam-milling for the fabrication of atom sieves

The atom sieves presented in paper IV were fabricated by the means of EBL and reactive ion etching. This is a process with multiple steps; coating the membrane with the etch mask and resist, patterning, development and reactive ion etching. Each step is correlated and the process requires careful optimization. In this appendix an alternative fabrication procedure using neon ion beam milling is described. Two different atom sieve designs were tested. The work was done at Carl Zeiss Microscopy, Peadbody, MA in collaboration with Lewis Stern, David Ferranti and Fouzia Khanom.

A.1 Why neon ions?

Direct-write lithography or milling is an attractive fabrication method for making free-standing structures. It is a one-step process and the result can be examined *in-situ*. The first idea was to mill the atom sieve in silicon nitride using helium ions. It was an optimistic idea, the sputtering yield of silicon nitride was found to be 0.07 atoms/ions in a TRIM calculation based on 34 keV helium ions (105 nm thick silicon nitride) [96], and the atom sieve design presented in Paper IV consists of 47011 holes with diameters ranging from 376 nm to 35 nm.

One alternative would be to mill the atom sieve using gallium ions. A. Nadzeyka et al. [97] used a gallium ion beam to mill a zone plate with a diameter of 100 μm and an outermost zone width of 100 nm. This was done in a 500 nm thick gold layer on a silicon nitride membrane (so this was not a free-standing structure). They developed a 15 h process to fabricate the zone plate which included automated drift correction on a mark outside the exposure area. An important difference between helium ion- and gallium ion milling is that helium ions impose less damage in and around the material being milled, which is crucial for milling high-density structures like the atom sieves. Moreover, gallium has a larger interaction volume close to the sample surface and is fundamentally not that well-suited for milling structures of high-density.

That being said, the liquid metal ion source can produce beam currents in the 100 nA range, and can hence provide the throughput needed for milling large areas. The second option is to use neon ions. Neon ions has been shown to exhibit similar resolution as helium ions for resist-based lithography [19], and have a higher sputtering yield than helium ions due to their larger mass and hence larger energy loss per unit path length [98]. As such, neon ion beam milling has a great potential in making functional free-standing structures of high density in thin membranes.

A.2 Atom sieve design 1

Atom sieve design 1 is shown in Figure A.1 ((ps_n84_Max_d10)). It consists of 61388 holes and has a radius of 11.755 μm. The largest hole-diameter is 275 nm with a gap of 50 nm. The smallest hole is 35 nm, with a gap of 20 nm. The characteristics of the neon ion beam is similar to that of the helium ion beam, so the challenge should not be to mill the smallest hole but to successfully mill the densest zones. Two pores (i.e. not free-standing holes) of increasing density were used to test how high-density features could be milled. Figure A.2 shows two pores in gold with a size of approximately 300 nm and a measured gap of 47 nm, roughly representing the densest zone of the sieve.

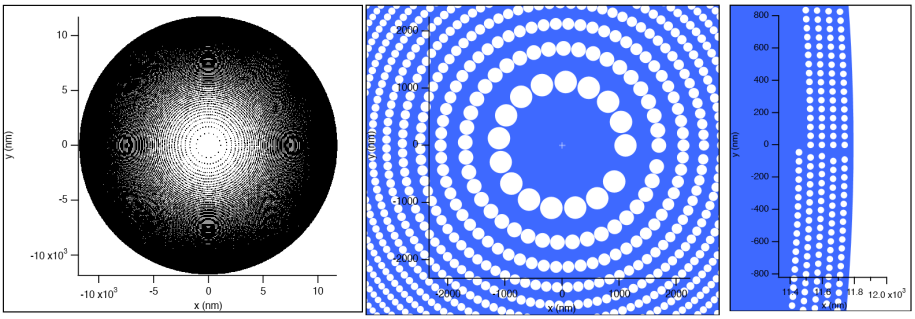

Figure A.1: Design used for milling with neon ions. The largest hole diameter is 275 nm with a gap of 50 nm, while smallest hole is 35 nm, with a gap of 20 nm.

Neon ion beam milling is still somewhat in its infancy. Neon has a lower ionization potential than helium and the beam current varies quite rapidly with time. As such, only about a quarter of the atom sieve was milled, a process that took about 30 minutes. It should be noted that compared to fabricating an atom sieve using electron beam lithography and reactive ion etching, this is a significant improvement. A quarter of the atom sieve can in principle still be used as an off-axis focusing element in the helium atom microsocpe. Figure A.3 shows a helium ion beam image of a quarter of this sieve, written with 30 keV neon ions in a 20 nm thick silicon nitride membrane. The write-field was 25 μm × 25 μm. The patterning parameters

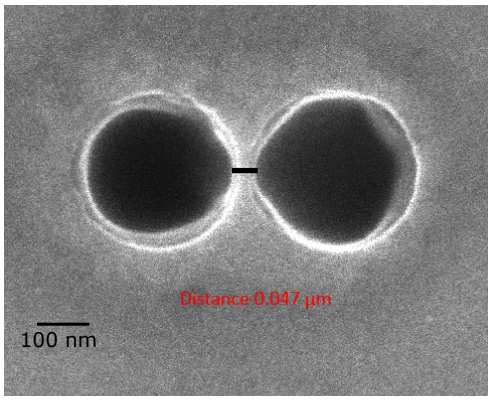

Figure A.2: Example of a dose matrix used to optimize the milling parameters for the atom sieve. Note that, this is two pores in gold not silicon nitride. The size of the pores is approximately 300 nm and the measured gap 47 nm. The images are taken using 30 keV helium ions and the conventional sample stage.

were as follows: a beam current of 4.193 pA, 1 nm stepsize, 0.06 ms dwell time and a dose of 1.6e17 ions/cm^2. The images are taken using a transmission stage where the beam transmitted through the membrane holes hits a polished metal surface before reaching the detector, and hence show opposite contrast to the conventional "reflection" image [99].

The membrane collapsed in the zones of highest density. The ion beam charges the membrane and this induces stress that has been shown to cause the membrane to break sporadically. Peltonen et al. [100] designed a metallic grid near the milling area to neutralize the charges. This could have been done as an attempt to reduce the stress induced in the membrane, and possibly prevent pattern collapse. Moreover, the atom sieve was milled by dwelling only once at each pixel. The stability of the membrane could depend on how the sieve is written, such that dwelling multiple times at each pixel would prevent the membrane from collapsing. Finally, the beam current was increased by decreasing the spot control number. This increases the spot size, and naturally decreases the resolution, which could cause a substantial overlap of neighboring point spread functions and hence the pattern collapse. To roughly test this, SRIM was used to estimate the beam profile. Figure A.4 shows the depth and lateral view of 1570 Ne^+ ions with a landing energy of 30 keV incident on 50 nm Si_3N_4 (density 3.2 g/cm^2). As indicated in Figure A.4(b) the full-width-at-half-maximum (FWHM) of the Gaussian beam profile was estimated to be 10 nm. This single Gaussian was used as the point spread function, and can at best only be considered as a rough estimate. The Gaussian was convolved with the pattern function, which is approximated as a step-function. The convolution of a 70 nm step and the point spread function is shown in Fig. A.5. The gap between the step function are 20 nm. The overlap is minor, even for a high density structure like this, indicating that this should not be the reason for membrane collapse. However, due to the inaccuracy of the estimation,

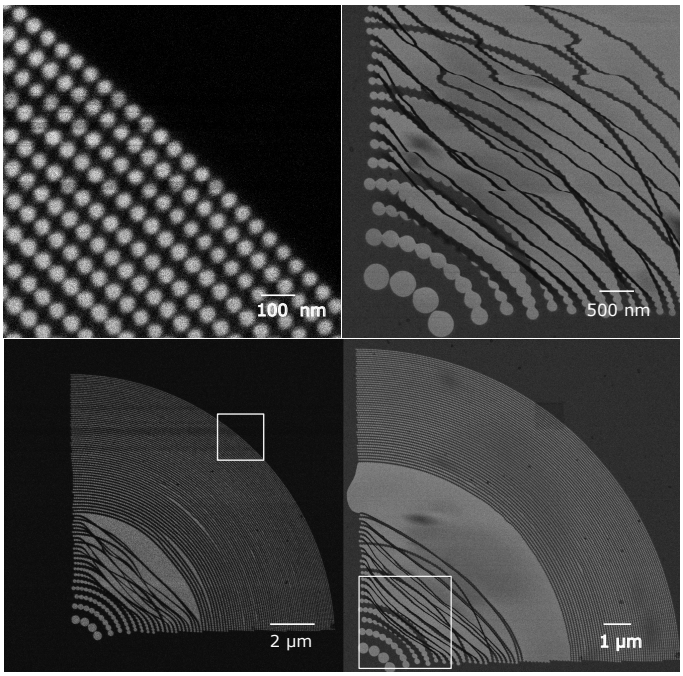

Figure A.3: Transmission helium ion beam images of the atom sieve milled in 20 nm thick Si_3N_4-membrane. The pattern collapse rapidly evolved, the lower images are the same atom sieve taken minutes apart. The squares indicate the regions where the higher magnification images are taken.

this should be studied in greater detail.

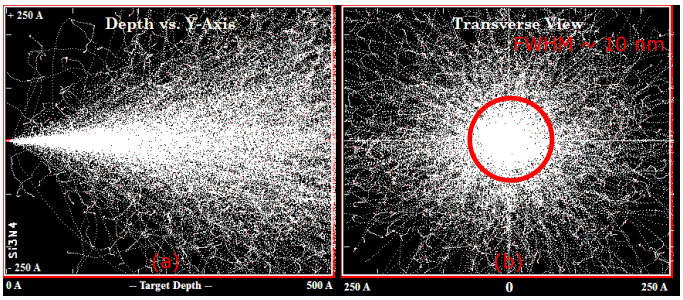

Figure A.4: SRIM calculation used for a rough estimation of the full-width-at-half-maximum (FWHM) of the point spread function of the neon ion beam, (a) Shows the trajectories of 30 keV neon ions into Si_3N_4. 1570 ions are simulated. (b) Shows the lateral view of the interaction volume which was used as an estimation of the FWHM of the point spread function.

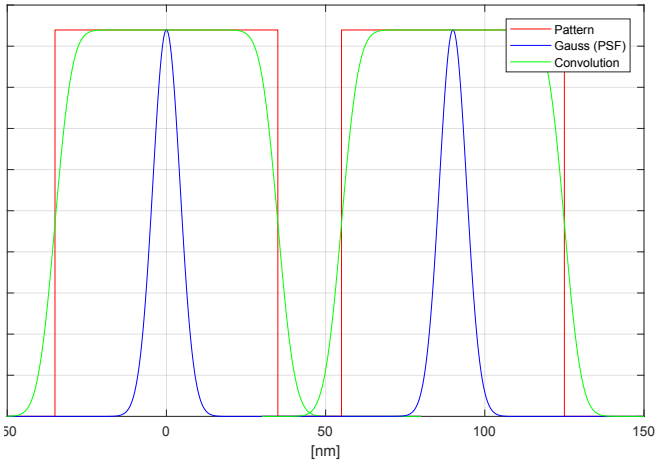

Figure A.5: Pattern file (red), estimated point-spread function (PSF, blue) and convolution of the two (green). The convolution is not significantly overlapping indicating that this is not the reason for pattern collapse.

A.3 Atom sieve design 2

As the first atom sieve design collapsed, another atom sieve design (ps_n84_Max_d20) was tested. This design is slightly less dense and is presented in paper IV. As mentioned, it consists of 47011 holes with diameter ranging from 376 nm to 35 nm (sieve diameter: 23.582 μm), see Figure 1.12. The gap between two neighboring holes in one zone ranges from 53 nm to 40 nm depending on how many holes it is possible to fit into one zone.

The sieve was milled in a 30 nm thick silicon nitride membrane using 30 keV neon ions, using the same dose as for atom sieve design 1. Again, the beam dwelled one time at each pixel, known as single pass, and the write-time was estimated to be 28 minutes. Four atom sieves were milled and in between each try a new trimer was built. Preliminary results are shown in Figure A.6. In the first three attempts, the beam current was lost, caused by adsorption of adatoms near the trimer atom, evident as a loss of contrast in the images. In theory it was stated that this should not reflect the stability of the source, so it is not fully understood why it happened. That being said, neon has a lower ionization potential than helium, and is therefore more sensitive to adatoms that "steal" the current. In the final run, the membrane collapsed around the densest part of the design. This could be caused by beam current fluctuations.

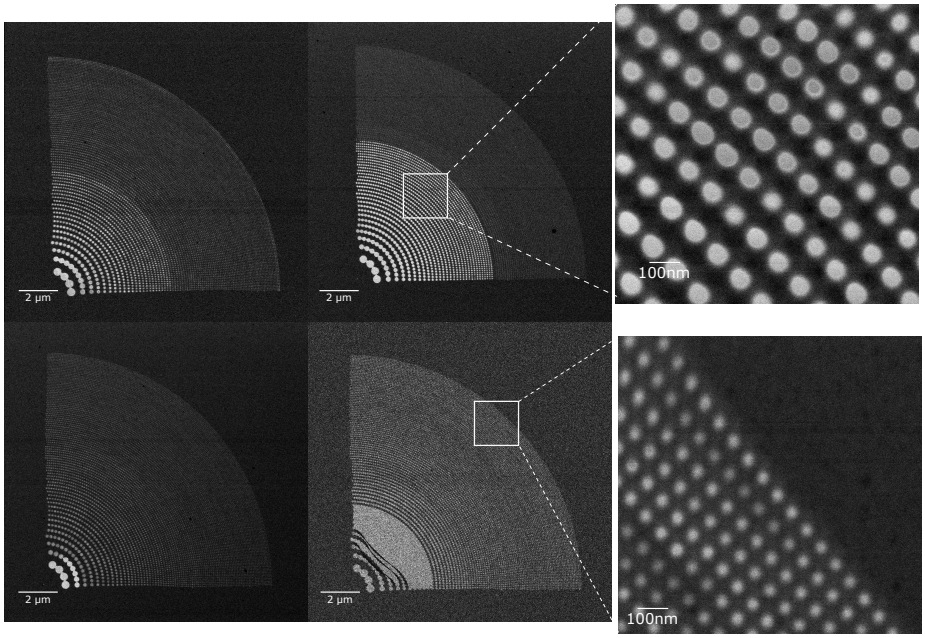

Figure A.6: Transmission neon ion beam images of the atom sieve design presented in Paper IV. In the first three attempts the beam current was lost, while in the final run the membrane collapsed.

Appendix B

Silicon nitride membrane fabrication procedure

This appendix describes the procedure for fabricating silicon nitride membranes at the Nanostructure Laboratory at University of Bergen. The procedure is described by Greve [53], but as some modifications to the procedure were made during this thesis work it is included here.

B.1 Step 1: Photolithography and pattern transfer

Low-stress silicon nitride (Si_3N_4) is deposited on silicon wafers by low pressure chemical vapor deposition. Deposition and polishing is done on both sides of the wafer. Note that the low-stress in the Si_3N_4 is found to significantly prevent the final membranes from breaking during reactive ion etching. For the work done at the Nanostructure Laboratory at UoB the thickness of the Si_3N_4 was 200 nm and the underlying 4-inch silicon wafer is 525 $\pm$ 25 μm thick. The wafers were ordered from MicroChemicals [1]or Si-Mat Silicon Materias [2].

The 4-inch wafer was spin-coated with photoresist on both sides. The front side, see Figure B.1, was coated to protect the surface. The resist (AR- P 3540 Allresist) was spun at 600 RPM for 18 seconds (pre-sin) and at 4000 RPM for 1 minute. Note that to ensure uniform coating the wafer must be centered properly on the spin-coater wafer-holder and the entire wafer should be covered with photoresist. The resist was then baked at 1 minute at 100° Celsius. According to the resist manufacturer, this should yield a thickness of about 1.4 μm.

The UV-lithography instrument at the Nanostructure Laboratory is homemade and consists of a light source and a simple vacuum arrangement to keep photomask film in place. Good vacuum is crucial to ensure good pattern transfer. The resist was exposed for one minute. The developer (AR 300-35 Allresist) was diluted in deionized water at a ratio 1:2 (developer : deionized water) and the solution was mixed by the means of magnetic stirring. To dissolve the exposed area, the wafer was left in the solution for about 45 seconds (it is clear by the naked eye when the development is completed). Then, the wafer was rinsed in de-ionized water and dried using pressurized nitrogen.

[1] www.microchemicals.com
[2] www.si-mat.com

The mask pattern was transferred to the underlying silicon by reactive ion etching. To fully open the silicon nitride two etch-steps is needed: (1) 15 SCCM flow of CF_4 at 10 mTorr, 100 W for 10 minutes and (2) to 45 SCCM of CF_4 and 5 SCCM of O_2, 350 W for 3 minutes. These parameters were established at the Nanostructure laboratory by Greve [53]. Finally, the front side of the wafer was exposed to UV-light and developed to remove any remaining photoresist.

B.2 Step 2: KOH-etch

KOH (potassium hydroxide) is a wet-etch that etches silicon preferentially in the <100> direction. This produces a partially anisotropic etch profile, see Figure B.1.The size of the window w on the front side of the membrane will thus be smaller than the size of the mask m

$$m = w + \frac{2t}{\tan\theta} \tag{B.1}$$

where t is the thickness of the wafer (525 μm in this case) and θ= 54.7°.

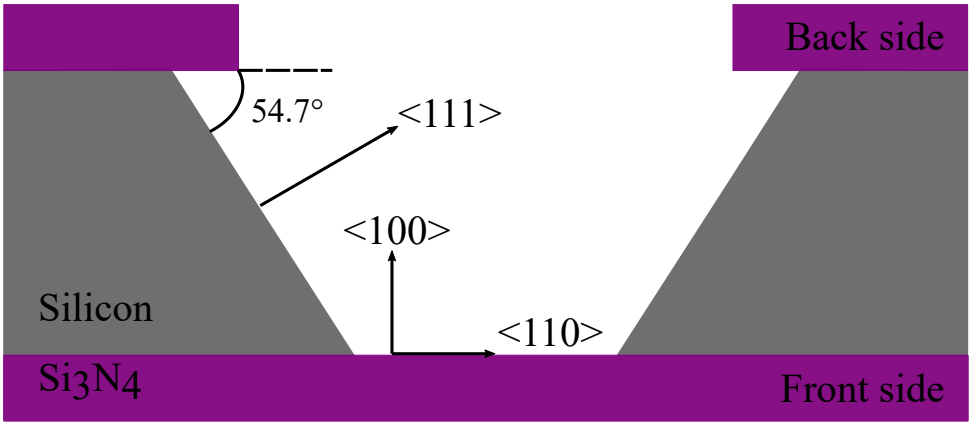

Figure B.1: Illustration of basic principle of a KOH etch. KOH favors the <100> direction, resulting in a partially anisotropic etch profile. The angle between the back side and <111> oritented sidewalls is 54.7°.

KOH does not etch Si_3N_4, but it does etch SiO_2 and hence quartz glassware needs to be used for this procedure. KOH was dissolved in de-ionized water. The etch rate of silicon depends on the concentration of KOH and the temperature[3]. Weight percent is defined as the weight of the solute (KOH) to the weight of the solution (KOH and water) and typically 30 % wt. was used in this thesis work. The KOH was heated to 80° Celsius and the sample was immersed into the solution. The concentration needs to be stable throughout the etch, and

[3]This website contains the etch rate along <100> and <110> for various concentrations and temperature: https://cleanroom.byu.edu/KOH.

therefore a glass condenser was used. Finally, the etched membranes were RCA cleaned, see [53]. A photograph of the front side of a nine-window membrane along with an SEM image of the backside of one window is shown in Figure B.2.

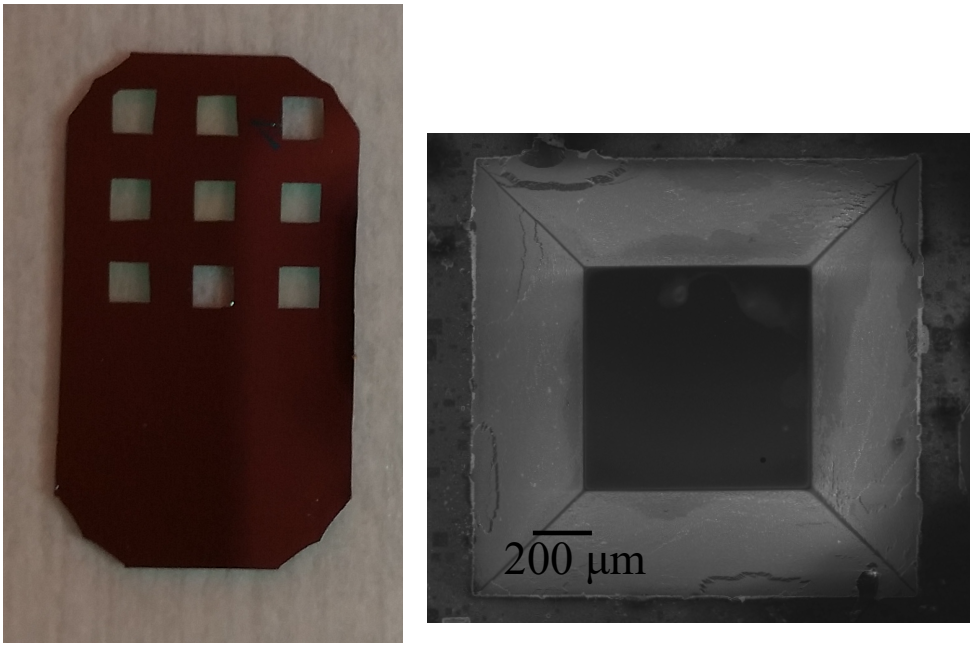

Figure B.2: Photograph of the front side of a nine-window membrane along with an SEM image of the backside of one window showing the KOH-etch profile. The hole in the lower right corner of the window is not a defect, but a patterned hole.

Additional notes to the procedure

- The adhesion between the photoresist and the silicon nitride can be improved by using an adhesion promoter, HDMS. The wafer is not ashed or cleaned prior to applying the adhesion promoter. HDMS is spun onto the wafer at a spin speed > 2000 RPM for 1 minute. The HDMS is not baked. Prior to spin-coating the photoresist, the HDMS should *settle* for a couple of minutes.
- During UV-exposure the resist outgasses (and hence loosens the vacuum). If the pattern transfer is poor, the exposure could be divided into sequences.
- To clean the back side of the wafer after pattern transfer by reactive ion etching, a final etch step in oxygen can be done.

Appendix C

Reactive ion etching for free-standing structures

An important part of this thesis work has been to fabricate atom optical elements. As mentioned in Chapter 1, the neutral helium atoms do not penetrate any solid material and hence the atom optical elements must be free-standing. It can be challenging to evaluate optically or by SEM imaging if all material has been removed by an etch procedure. An example is given in Figure C.1. The "hole" seems to be free-standing as no signals appears to be originating from the patterned area. However, the hole was not transmissive to helium atoms and hence all material was not removed in the final etch procedure [101]. This appendix describes the etch-parameters used based on (a) an etch-mask of ARC, SiO_2 and PMMA and (b) PMMA for making freestanding silicon nitride structures.

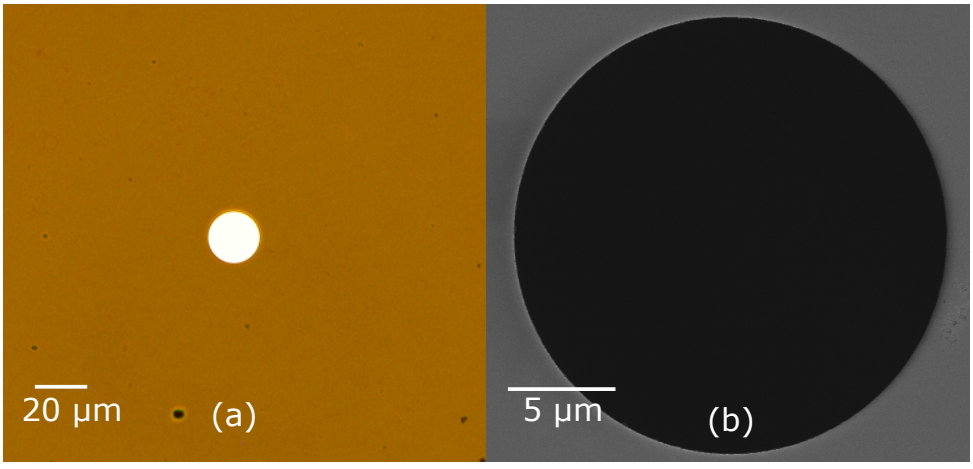

Figure C.1: (a) Optical microsocpy image and (b) SEM image of a 20 µm "hole". The hole appears to be free-standing, but it is not, because it was not transmissive to helium atoms [101].

C.1 Etch-mask 1: ARC, SiO_2, PMMA

The etch parameters (RF power, gas, gas flow rate, pressure) are based on the work of Greve [53]. The silicon nitride has a thickness of 200 nm, and the etch mask consist of antireflective coating (ARC, Brewster Science, XHRIC-11), SiO_2 and PMMA. Firstly, the ARC was spin-coated onto the membrane at 4000 RPM for 1 minute followed by a 2 minute bake at 150° Celsius, and the thickness was measured using a reflectrometer (although on a pure silicon wafer) to be 151 nm. This procedure was repeated, but the bake time was increased to 5 minute to ensure that the ARC cross-link. The final thickness of ARC was about 300 nm. The thickness of the ARC was chosen to be greater than the thickness of the Si_3N_4 due to poor selectivity of the reactive ion etching procedure i.e. the ability to remove only Si_3N_4. That being said successful etching using 150 nm ARC has been done at the Nanostructure laboratory [53]. Then, 20 nm SiO_2 was deposited by the means of electron beam evaporation. PMMA (950 K, diluted in anisole at a ratio PMMA:anisole, 2:3) was spin-coated at 4000 RPM and baked at 175 ° Celsius for 5 minutes. Finally, a 4 nm chrome layer was deposited using electron beam evaporation. The chrome served as a charge dissipating layer during the electron beam lithography procedure, see Figure C.2

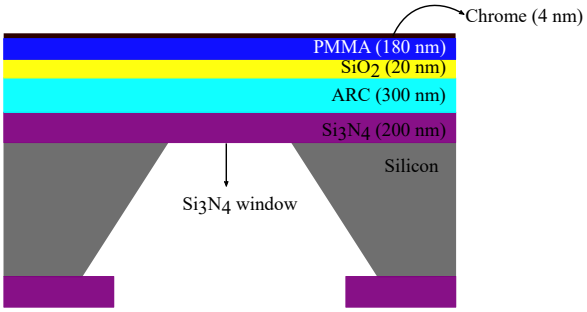

Figure C.2: Etch mask 1 used to fabricate free-standing structures. The etch mask consists of ARC, SiO_2 and PMMA. The chrome-film is removed prior to the reactive ion etching, and acts as a charge dissipating layer during the electron beam exposure.

A grating was exposed in PMMA using EBL. After exposure, the chrome was removed in a chemical etch (Transene company inc). The sample was immersed into the chrome etch for 25 seconds, based on the etch-rate found using a microscope slide (that turns transparent when the chrome is removed). The chrome etch is found not to interact or remove the PMMA, and hence over-etching should not be a problem. Then, PMMA was developed in a 1:3 MIBK:IPA (methyl 2-methylpropyl ketone:2-propanol) at room temperature for 1.5 minutes, rinsed with IPA and dried using pressurized nitrogen. The etch parameters are given in Table C.1. The pattern transfer into the SiO_2 was done using the parameters by Greve, and Grepstad et al. [53, 102]. Pattern transfer into the ARC layer was done using helium and oxygen. Figure C.3 shows a cross-section of the grating after etching the ARC for 7 minutes. There was about

35 nm of ARC left, which served as an estimation of the etch-rate ($\sim$ 37 nm/min). Pattern transfer into the Si_3N_4 was done using CF_4. After 9 minutes about 110 - 120 nm of Si_3N_4 was left, corresponding to an etch-rate of 8 - 10 mn/min. After another 15 minutes of etching, the pattern was transferred into the silicon substrate. The etch rate of ARC in CF_4 was estimated to 8 - 9 nm/min. As will be discussed in Section C.2, cyclic RIE processes where the cylces are separated by a N_2 flushing step has been shown to improve selectivity, change the etch-rates and the etch-directionality [103]. As such, breaking the vacuum could influence the etch-result. Moreover, etching membrane windows, as shown in Figure C.2, could also influence the etch-result, as there is no underlying silicon support and the window could in principle be etched from both sides. That being said, as a sanity check these parameters was used to etch a donut pattern in a silicon nitride window, and the resulting free-standing hole is shown in Figure C.4.

Table C.1: Etch-parameters used for etching SiO_2, ARC and Si_3N_4.

Material	SiO_2	ARC	Si_3N_4
Pressure [mTorr]	10	7	10
RF power [W]	100	100	100
Gas 1	CHF_3	He	CF_4
Flow [sccm]	15	10	15
Gas 2	-	O_2	-
Flow [sccm]	-	5	-
Estimated eth-rate [nm/min]	-	37	8 - 10
Duration [min]	3.5	8	9 + 15

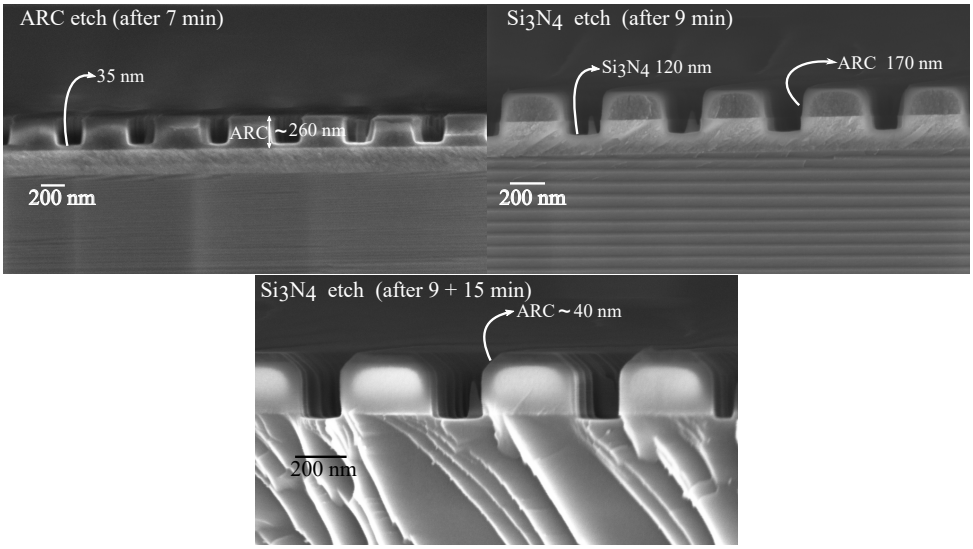

Figure C.3: Cross-section SEM images of the optimization process of using ARC, SiO_2 and PMMA as etch mask to fabricate free-standing structures.

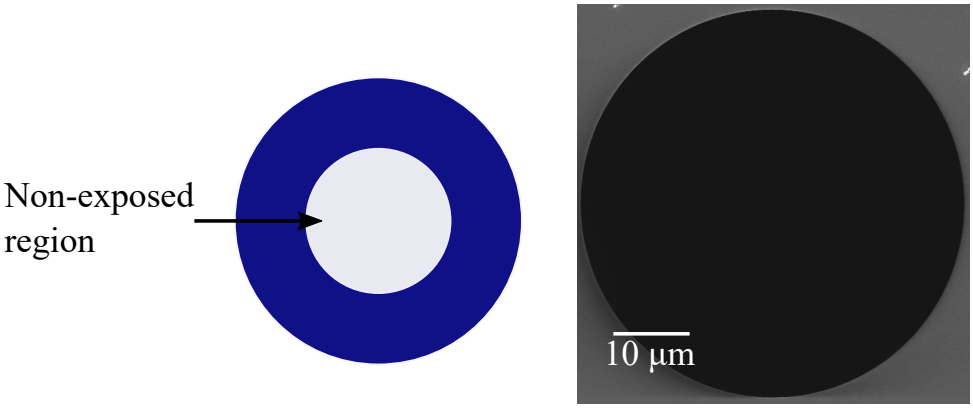

Figure C.4: SEM image of a donut pattern (left) etched using the parameters presented in Table C.1

C.2 Etch-mask 2 : PMMA

As briefly discussed above, cyclic RIE processes has been shown to improve selectivity, change the etch-rate and alter the anisotropicity [103]. Wüest et al [103] found that the cycling etching of SiN_x in CHF_3 and O_2 increased the etch rate of SiN_x with 15 %. PMMA was used as the etch mask. The increase in etch-rate of the SiN_x was attributed to the desorption of the CF_x layer during the N_2 flushing. To ensure low etch-rate of PMMA, temperature control

is important as PMMA melts at 160° Celsius and the increase in temperature is dominated by heat radiation (and not thermal conductance). Moreover, compared to an identical RIE without cycling, they found that the cyclic process improved the etch anisotropicity. Cyclic RIE was first tested by Selfors at the Nanostructure laboratory [104] inspired by the results of Wüest et al. [103].

PMMA was spin-coated onto the Si_3N_4. The thickness was measured using a reflectrometer and was found to be 171 nm. A grating was exposed using EBL. PMMA was developed in MIBK:IPA (1:3) for 1.5 minutes, then rinsed in IPA and dried using pressurized nitrogen. The RIE parameters are shown in Table C.2. Each cycle consisted of 1 minute etching followed by 1 minute flushing. An SEM image of the grating after 5 RIE cycles (i.e. 5 minutes of etching) is shown in Figure C.5(a). The contrast is rather poor, and imaging PMMA is equivalent to exposing PMMA. It was not possible to get a reliable number of the thickness of the remaining PMMA. The etch-rate of Si_3N_4 was estimated to be 18 nm/min, which is a significant improvement from 8 – 10 nm/min (see Table C.1). However, as the etch-parameters of the two procedures are different no direct comparison can be made. Also note that the etch directionality is reduced (Figure C.5(a) relative to Figure C.3).

Table C.2: Etch-parameters used for etching Si_3N_4 with PMMA as etch-mask.

Material	Si_3N_4
Pressure [mTorr]	10
RF power [W]	200
Gas 1	CF_4
Flow [sccm]	10
Estimated eth-rate [nm/min]	18
Total no of cycles	12
Duration [min]	12

To test the etch procedure, the parameters presented in Table C.2 were used to etch a rectangle (a slit) on a silicon nitride window. The size of the rectangle was large (300 μm × 100 μm) to ensure that optical imaging could be done in between the cycles (6 cycles, 4 cycles, 2 cycles = 12 cycles). After 12 cycles the inner region fell out, and a free-standing slit was produced, see Figure C.5(b). It looked as if the membrane was thinned during the procedure (by the naked eye). As a summary, the procedure described in Section C.1 is recommended for etching complex structures (e.g. an atom sieve). That being said, large structures such as the collimating apertures presented in Paper V, should easily be realized with a PMMA etch-mask.

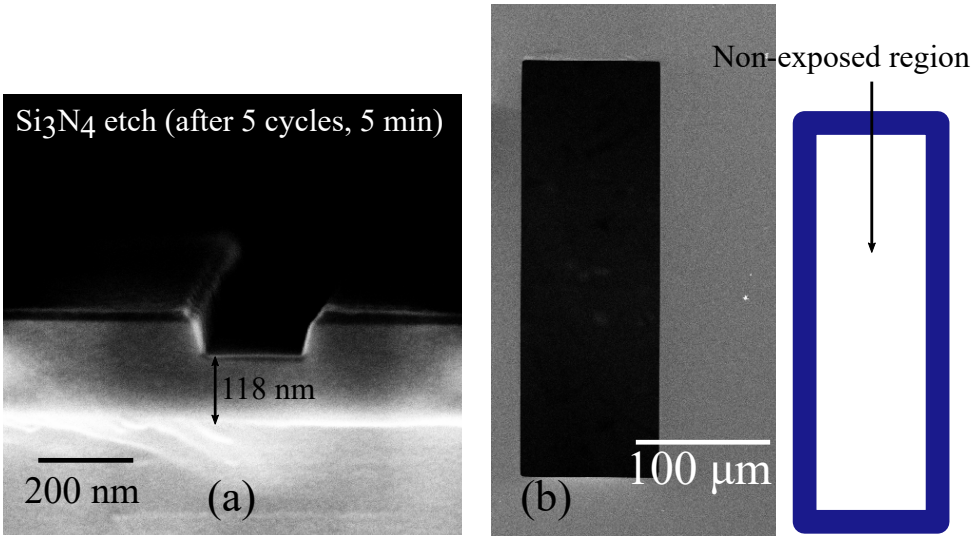

Figure C.5: (a) Cross-section SEM image of the optimization process on etching Si_3N_4 using PMMA as etch mask. (b) SEM image of a rectangle (left) etched using the parameters presented in Table C.2 after the inner region fell out. Note that the signal coming from the etched region is the underlying SEM sample holder.

Bibliography

[1] M Stepanova and S Dew, editors. *Nanofabrication: techniques and principles*. Springer Verlag, Springer Science & Business Media, Wien, 2012.

[2] G. E Moore. Cramming more components onto integrated circuits. *Electronics*, 38(8), 1965.

[3] G Hodes. When small is different: Some recent advances in concepts and applications of nanoscale phenomena. *Advanced Materials*, 19(5):639–655, 2007.

[4] D. T Thompson. Using gold nanoparticles for catalysis. *Nano Today*, 2(4):40–43, 2007.

[5] K. L Kelly, E Coronado, L. L Zhao, and G. C Schatz. The optical properties of metal nanoparticles: The influence of size, shape, and dielectric environment. *The Journal of Phsyical Chemistry B*, 107(3):668–677, 2003.

[6] A.E Danks, S.R Hall, and Z Schnepp. The evolution of 'sol–gel'chemistry as a technique for materials synthesis. *Materials Horizons*, 3(2):91–112, 2016.

[7] S. M George. Atomic layer deposition: An overview. *Chemical Reviews*, 110(1):111–131, 2010.

[8] G. M Whitesides and B Grzybowski. Self-assembly at all scales. *Science*, 295(5564): 2418–2421, 2002.

[9] A Tavakkoli K.G., K.W Gotrik, A.F Hannon, A Alexander-Katz, C.A Ross, and K.K Berggren. Templating three-dimensional self-assembled structures in bilayer block copolymer films. *Science*, 336(6086):1294–1298, 2012.

[10] B. Bhushan, editor. *Springer Handbook of Nanotechnology*. Springer-Verlag Berlin Heidelberg, 2004.

[11] R.D Piner, J. Zhu, F. Xu, S. Hong, and C.A Mirkin. "Dip-pen" nanolithography. *Science*, 283(5402):661–663, 1999.

[12] R.G Hobbs, N Petkov, and J. D Holmes. Semiconductor nanowire fabrication by bottom-up and top-down paradigms. *Chemistry of Materials*, 24(11):1975–1991, 2012.

[13] W.-D. Li, W Wu, and R. S Williams. Combined helium ion beam and nanoimprint lithography attains 4 nm half-pitch dense patterns. *Journal of Vacuum Science & Technology B, Nanotechnology and Microelectronics: Materials, Processing, Measurement, and Phenomena*, 30(6):06F304, 2012.

[14] M. K Oberthaler and T. Pfau. One-, two-and three-dimensional nanostructures with atom lithography. *Journal of Physics: Condensed Matter*, 15(6):R233–R255, 2003.

[15] J Fujita, M Morinaga, T Kishimoto, M Yasuda, S Matsui, and F Shimizu. Manipulation of an atomic beam by a computer-generated hologram. *Nature*, 380:691–694, 1996.

[16] T Nesse, I Simonsen, and B Holst. Nanometer resolution mask lithography with matter waves. *arXiv:1804.06910*, 2018.

[17] V.R Manfrinato, A Stein, L Zhang, C-Y. Nam, K.G Yager, E.A Stach, and C.T Black. Aberration-corrected electron beam lithography at the one nanometer length scale. *Nano Letters*, 17(8):4562–4567, 2017.

[18] J.K.W Yang, B Cord, H Duan, K.K Berggren, J Klingfus, S.-W Nam, K.-B Kim, and M.J Rooks. Understanding of hydrogen silsesquioxane electron resist for sub-5-nm-half-pitch lithography. *Journal of Vacuum Science & Technology B: Microelectronics and Nanometer Structures Processing, Measurement, and Phenomena*, 27(6):2622–2627, 2009.

[19] D Winston, V. R Manfrinato, S. M Nicaise, L. L Cheong, H Duan, D Ferranti, J Marshman, S McVey, L Stern, J Notte, and K.K Berggren. Neon ion beam lithography (NIBL). *Nano letters*, 11(10):4343–4347, 2011.

[20] D Drouin, A. R Couture, D Joly, X Tastet, V Aimez, and R Gauvin. Casino v2. 42—A fast and easy-to-use modeling tool for scanning electron microscopy and microanalysis users. *Scanning*, 29(3):92–101, 2007.

[21] J.F Ziegler, J.P Biersack, and M.D Ziegler. SRIM -The stopping and range of ions in matter. MD: SRIM Co., 2008.

[22] D Winston, B.M Cord, B Ming, D.C Bell, W.F DiNatale, L.A Stern, A.E Vladar, M.T Postek, M.K Mondol, J.K.W Yang, and K.K Berggren. Scanning-helium-ion-beam lithography with hydrogen silsesquioxane resist. *Journal of Vacuum Science & Technology B: Microelectronics and Nanometer Structures Processing, Measurement, and Phenomena*, 27(6):2702, 2009.

[23] V Sidorkin, E van Veldhoven, E van der Drift, P Alkemade, H Salemink, and D Maas. Sub-10-nm nanolithography with a scanning helium beam. *Journal of Vacuum Sci-*

ence & Technology B: Microelectronics and Nanometer Structures Processing, Measurement, and Phenomena, 27(4):L18–L20, 2009.

[24] M.S. Joens, C. Huynh, J.M. Kasuboski, D. Ferranti, Y.J. Sigal, F. Zeitvogel, M. Obst, C.J. Burkhardt, K.P. Curran, S.H. Chalasani, L.A. Stern, B Goetze, and J.A.J Fitzpatrick. Helium ion microscopy (HIM) for the imaging of biological samples at sub-nanometer resolution. *Scientific Reports*, 3:1–7, 2013.

[25] A. N Abbas, G Liu, B Liu, L Zhang, H Liu, D Ohlberg, W Wu, and C Zhou. Patterning, characterization, and chemical sensing applications of graphene nanoribbon arrays down to 5 nm using helium ion beam lithography. *ACS Nano*, 8(2):1538–1546, 2014.

[26] W.S Vanden Berg-Foels, L Scipioni, C Huynh, and X Wen. Helium ion microscopy for high-resolution visualization of the articular cartilage collagen network. *Journal of Microscopy*, 246(2):168–176, 2012.

[27] S.A Boden, Z Moktadir, D.M Bagnall, H Mizuta, and H.N Rutt. Focused helium ion beam milling and deposition. *Microelectronic Engineering*, 88(8):2452–2455, 2011.

[28] D.C Bell, M.C Lemme, L.A Stern, J.R Williams, and C.M Marcus. Precision cutting and patterning of graphene with helium ions. *Nanotechnology*, 20(45):455301, 2009.

[29] X. Shi, P. Prewett, E. Huq, D.M. Bagnall, A.P.G. Robinson, and S.A. Boden. Helium ion beam lithography on fullerene molecular resists for sub-10nm patterning. *Microelectronic Engineering*, 155:74–78, 2016.

[30] H Guo, H Itoh, C Wang, H Zhang, and D Fujita. Focal depth measurement of scanning helium ion microscope. *Applied Physics Letters*, 105(2):023105, 2014.

[31] Y Xie, Z Lu, and F Li. Fabrication of large diffractive optical elements in thick film on a concave lens surface. *Optics Express*, 11(9):992–995, 2003.

[32] J Zhang, B Shokouhi, and B Cui. Tilted nanostructure fabrication by electron beam lithography. *Journal of Vacuum Science & Technology B, Nanotechnology and Microelectronics: Materials, Processing, Measurement, and Phenomena*, 30(6):06F302, 2012.

[33] R Flatabø, A Agarwal, R Hobbs, M.M Greve, B Holst, and K.K Berggren. Exploring proximity effects and large depth of field in helium ion beam lithography: Large-area dense patterns and tilted surface exposure. *Nanotechnology*, 29(27):275301, 2018.

[34] S.J Smith and E.M Purcell. Visible light from localized surface charges moving across a grating. *Physical Review*, 92(4):1069, 1953.

[35] J Urata, M Goldstein, M.F Kimmitt, A Naumov, C Platt, and J.E Walsh. Superradiant Smith-Purcell emission. *Physical Review Letters*, 80(3):516–519, 1998.

[36] D. E Wortman, R. P Leavitt, H Dropkin, and C. A Morrison. Generation of millimeter-wave radiation by means of a Smith-Purcell free-electron laser. *Physical Review A*, 24 (2):1150, 1981.

[37] Y. Neo, H Shimawaki, T Matsumoto, and H Mimura. Smith-Purcell radiation from ultraviolet to infrared using a Si field emitter. *Journal of Vacuum Science & Technology B: Microelectronics and Nanometer Structures Processing, Measurement, and Phenomena*, 24(2):924–926, 2006.

[38] G Adamo, K.F MacDonald, Y.H Fu, C.M Wang, D.P Tsai, F.J Garcia de Abajo, and N.I Zheludev. Light well: A tunable free-electron light source on a chip. *Physical review letters*, 103(11):113901, 2009.

[39] A Massuda, C Roques-Carmes, Y Yang, S. E Kooi, Y Yang, C Murdia, K. K Berggren, I Kaminer, and M Soljačić. Smith-Purcell radiation from low-energy electrons. In *arXiv:1710.05358*, 2017.

[40] Y Leng. *Materials characterization: Introduction to microscopic and spectroscopic methods*. John Wiley & Sons (Asia) Pte Ltd, Singapore, 2008.

[41] J. Goldstein, D Newbury, D Joy, C Lyman, P Echlin, E Lifshin, L Sawyer, and Michael J. *Scanning electron microscopy and X-ray microanalysis (3rd edition)*. Springer Science + Business Media, New York, 2003.

[42] J Cazaux. Some considerations on the secondary electron emission, δ, from e- irradiated insulators. *Journal of Applied Physics*, 85(2):1137–1147, 1999.

[43] D. C Joy and C. S Joy. Study of the dependence of e2 energies on sample chemistry. *Microscopy and Microanalysis*, 4(5):475–480, 1998.

[44] N Okai and Y Sohda. Study on image drift induced by charging during observation by scanning electron microscope. *Japanese Journal of Applied Physics*, 51(6S):06FB11, 2012.

[45] O Jbara, S Fakhfakh, M Belhaj, and S Rondot. Charge implantation measurement on electron-irradiated insulating materials by means of a SEM technique. *Microscopy and Microanalysis*, 10(6):697–710, 2004.

[46] R Flatabø, A Coste, and M.M Greve. A systematic investigation of the charging effect in scanning electron microscopy for metal nanostructures on insulating substrates. *Journal of microscopy*, 265(3):287–297, 2017.

[47] A.D McFarland and R. P Van Duyne. Single silver nanoparticles as real-time optical sensors with zeptomole sensitivity. *Nano Letters*, 3(8):1057–1062, 2003.

[48] V.R.A Holm, B. Y Zheng, P. M Denby, B Holst, N. J Halas, and M. M Greve. Work function-driven hot electron extraction in a bimetallic plasmonic MIM device. *ACS Photonics*, 5(4):1202–1207, 2018.

[49] C Loo, A Lowery, N Halas, J West, and R Drezek. Immunotargeted nanoshells for integrated cancer imaging and therapy. *Nano Letters*, 5(4):709–711, 2005.

[50] S. A Maier. *Plasmonics: fundamentals and applications*. Springer Science & Business Media, New York, 2007.

[51] C.F Bohren and D. R Huffman. *Absorption and scattering of light by small particles*. Wiley - VCH Verlag GmbH & Co. KGaA, Weinheim, 1983.

[52] X Xu, M Stevens, and M.B Cortie. In situ precipitation of gold nanoparticles onto glass for potential architectural applications. *Chemistry of materials*, 16(11):2259–2266, 2004.

[53] M.M Greve. *Nanostructures for the manipulation of electromagnetic waves*. PhD thesis, University of Bergen, 2013.

[54] C Langhammer, B Kasemo, and I Zorić. Absorption and scattering of light by Pt, Pd, Ag, and Au nanodisks: Absolute cross sections and branching ratios. *The Journal of Chemical Physics*, 126(19):194702, 2007.

[55] H Fredriksson, Y Alaverdyan, A Dmitriev, C Langhammer, D S Sutherland, M Zäch, and B Kasemo. Hole–mask colloidal lithography. *Advanced Materials*, 19(23):4297–4302, 2007.

[56] R Flatabø, V.R.A Holm, H Eidsvåg, B Holst, and M. M Greve. Light absorption and scattering of 40–170 nm gold nanoparticles on glass substrates. *Journal of Vacuum Science & Technology B, Nanotechnology and Microelectronics: Materials, Processing, Measurement, and Phenomena*, 35(6):06G403, 2017.

[57] C. L Haynes, A. D McFarland, L Zhao, R. P Van Duyne, G. C Schatz, L Gunnarsson, J Prikulis, B Kasemo, and M Käll. Nanoparticle optics: The importance of radiative dipole coupling in two-dimensional nanoparticle arrays. *The Journal of Physical Chemistry B*, 107(30):7337–7342, 2003.

[58] B Lamprecht, G Schider, R.T Lechner, H Ditlbacher, J. R Krenn, A Leitner, and F. R Aussenegg. Metal nanoparticle gratings: Influence of dipolar particle interaction on the plasmon resonance. *Physical Review Letters*, 84(20):4721–4724, 2000.

[59] Sabrina Daniela Eder. *A neutral matter-wave microscope (NEMI): design and setup*. PhD thesis, University of Bergen, 2012.

[60] G Bracco and B Holst, editors. *Surface science techniques*. Springer-Verlag Berlin Heidelberg, 2013.

[61] S Koch, Mand Rehbein, G Schmahl, T Reisinger, G Bracco, W.E Ernst, and B Holst. Imaging with neutral atoms—A new matter-wave microscope. *Journal of Microscopy*, 229(1):1–5, 2007.

[62] M Barr, A Fahy, J Martens, A. P Jardine, D. J Ward, J Ellis, W Allison, and P.C Dastoor. Unlocking new contrast in a scanning helium microscope. *Nature Communications*, 7: 10189, 2016.

[63] R.B Doak, R.E Grisenti, S Rehbein, G Schmahl, J.P Toennies, and Ch Wöll. Towards realization of an atomic de Broglie microscope: Helium atom focusing using Fresnel zone plates. *Physical Review Letters*, 83(21):4229, 1999.

[64] B Holst and W Allison. An atom-focusing mirror. *Nature*, 390:244, 1997.

[65] H.C Schewe, B.S Zhao, G Meijer, and W Schöllkopf. Focusing a helium atom beam using a quantum-reflection mirror. *New Journal of Physics*, 11:113030, 2009.

[66] K Fladischer et al. An ellipsoidal mirror for focusing neutral atomic and molecular beams. *New journal of Physics*, 12:033018, 2010.

[67] T Reisinger and B Holst. Neutral atom and molecule focusing using a Fresnel zone plate. *Journal of Vacuum Science & Technology B: Microelectronics and Nanometer Structures Processing, Measurement, and Phenomena*, 26(6):2374–2379, 2008.

[68] S.D Eder, T Reisinger, M.M Greve, G Bracco, and B Holst. Focusing of a neutral helium beam below one micron. *New Journal of Physics*, 14:073014, 2012.

[69] E Hecht. *Optics Fourth Edition*. Pearson Education, Addison Wesley, 2002.

[70] A. G Michette. *Optical systems for soft X rays*. Plenum Press, New York, 1986.

[71] S.D Eder, A.K Ravn, B Samelin, G Bracco, A.S Palau, T Reisinger, E.B Knudsen, K Lefmann, and B Holst. Zero-order filter for diffractive focusing of de Broglie matter waves. *Physical Review A*, 95(2):023618, 2017.

[72] S Rehbein. *Entwicklung von freitagenden nanostrukturierten Zoneplatten zur fokussierung und Monochromatiserung thermischer Helium-Atomstrahlen*. PhD thesis, Georg-August Universität zu Göttingen, 2001.

[73] L Kipp, M Skibowski, R.L Johnson, R Berndt, R Adelung, S Harm, and R Seemann. Sharper images by focusing soft x-rays with photon sieves. *Nature*, 414:184–188, 2001.

[74] S.D Eder, X Guo, T Kaltenbacher, M.M Greve, M Kalläne, L Kipp, and B Holst. Focusing of a neutral helium beam with a photon-sieve structure. *Physical Review A*, 91 (4):043608, 2015.

[75] T Reisinger. *Free-standing, axially-symmetric diffraction gratings for neutral matter waves: experiments and fabrication*. PhD thesis, University of Bergen, 2011.

[76] R Flatabø, S.D Eder, A.K Ravn, B Samelin, M.M Greve, T Reisinger, and B Holst. Fast resolution change in neutral helium atom microscopy. *Review of Scientific Instruments*, 89(5):053702, 2018.

[77] M Wang, editor. *Lithography*. InTech, Rijeka, 2010.

[78] S.A Rishton and D.P Kern. Point exposure distribution measurements for proximity correction in electron beam lithography on a sub-100 nm scale. *Journal of Vacuum Science & Technology B: Microelectronics Processing and Phenomena*, 5(1):135–141, 1986.

[79] V. R Manfrinato, L Zhang, D Su, H Duan, R. G Hobbs, E. A Stach, and K. K Berggren. Resolution limits of electron-beam lithography toward the atomic scale. *Nano Letters*, 13(4):1555–1558, 2013.

[80] S Yasin, DG Hasko, and H Ahmed. Comparison of MIBK/IPA and water/IPA as PMMA developers for electron beam nanolithography. *Microelectronic engineering*, 61:745–753, 2002.

[81] J.K.W Yang and K. K Berggren. Using high-contrast salty development of hydrogen silsesquioxane for sub-10-nm half-pitch lithography. *Journal of Vacuum Science & Technology B: Microelectronics and Nanometer Structures Processing, Measurement, and Phenomena*, 25(6):2025–2029, 2007.

[82] W Hu, K Sarveswaran, M Lieberman, and G. H Bernstein. Sub-10 nm electron beam lithography using cold development of poly (methylmethacrylate). *Journal of Vacuum Science & Technology B: Microelectronics and Nanometer Structures Processing, Measurement, and Phenomena*, 22(4):1711–1716, 2004.

[83] B Cord, J Lutkenhaus, and K. K Berggren. Optimal temperature for development of poly (methylmethacrylate). *Journal of Vacuum Science & Technology B: Microelectronics and Nanometer Structures Processing, Measurement, and Phenomena*, 25(6): 2013–2016, 2007.

[84] K.K Berggren and H.I Smith. Nanostructure fabrication. Book Manuscript.

[85] A Raghunathan and J. G Hartley. Influence of secondary electrons in high-energy electron beam lithography. *Journal of Vacuum Science & Technology B, Nanotechnology and Microelectronics: Materials, Processing, Measurement, and Phenomena*, 31(1): 011605, 2013.

[86] H Gregor and A Gölzhäuser, editors. *Helium ion microscopy*. Springer International, Switzerland, 2016.

[87] L Scipioni, C.A Sanford, J Notte, B Thompson, and S McVey. Understanding imaging modes in the helium ion microscope. *Journal of Vacuum Science & Technology B: Microelectronics and Nanometer Structures Processing, Measurement, and Phenomena*, 27(6):3250–3255, 2009.

[88] Microscopy and analysis. `http://microscopy-analysis.com/news/zeiss-smt-Orion-recordresolution`. Online; accessed 01 December 2017.

[89] R Livengood, S Tan, Y Greenzweig, J Notte, and S McVey. Subsurface damage from helium ions as a function of dose, beam energy, and dose rate. *Journal of Vacuum Science & Technology B: Microelectronics and Nanometer Structures Processing, Measurement, and Phenomena*, 27(6):3244–3249, 2009.

[90] K Nojiri. *Dry etching technology for semiconductors*. Springer International Switzerland, 2015.

[91] H.V Jansen, H.G.E Gardeniers, M.J de Boer, M.C Elwenspoek, and J.H.J Fluitman. A survey on the reactive ion etching of silicon in microtechnology. *Journal of Micromechanics and Microengineering*, 6(1):14–28, 1996.

[92] V.R.A Holm. *Nanostructured materials for solar energy applications*. PhD thesis, University of Bergen, 2018.

[93] Labsphere. Integrating sphere theory and applications - Technical guide.

[94] J Zhang, C Con, and B Cui. Electron beam lithography on irregular surfaces using an evaporated resist. *ACS nano*, 8(4):3483–3489, 2014.

[95] L.E Scriven. Physics and applications of dip coating and spin coating. *MRS Online Proceedings Library Archive*, 121, 1988.

[96] M.M Marshall, J Yang, and A. R Hall. Direct and transmission milling of suspended silicon nitride membranes with a focused helium ion beam. *Scanning*, 34(2):101–106, 2012.

[97] A Nadzeyka, L Peto, S Bauerdick, M Mayer, K Keskinbora, C Grévent, M Weigand, M Hirscher, and G Schütz. Ion beam lithography for direct patterning of high accuracy large area x-ray elements in gold on membranes. *Microelectronic Engineering*, 98: 198–201, 2012.

[98] R Timilsina and P. D Rack. Monte Carlo simulations of nanoscale focused neon ion beam sputtering. *Nanotechnology*, 24(49):495303, 2013.

[99] A. R Hall. In situ thickness assessment during ion milling of a free-standing membrane using transmission helium ion microscopy. *Microscopy and Microanalysis*, 19(3):740–744, 2013.

[100] A Peltonen, H.Q Nguyen, J. T Muhonen, and J P Pekola. Milling a silicon nitride membrane by focused ion beam. *Journal of Vacuum Science & Technology B, Nanotechnology and Microelectronics: Materials, Processing, Measurement, and Phenomena*, 34 (6):062201, 2016.

[101] R Flatabø, M. M Greve, S. D Eder, M Kalläne, A. S Palau, K. K Berggren, and B Holst. Atom sieve for nanometer resolution neutral helium microscopy. *Journal of Vacuum Science & Technology B, Nanotechnology and Microelectronics: Materials, Processing, Measurement, and Phenomena*, 35(6):06G502, 2017.

[102] J.O Grepstad, M. M Greve, T Reisinger, and B Holst. Nanostructuring of free-standing, dielectric membranes using electron-beam lithography. *Journal of Vacuum Science & Technology B, Nanotechnology and Microelectronics: Materials, Processing, Measurement, and Phenomena*, 31(6):06F402–1, 2013.

[103] R Wüest, P Strasser, F Robin, D Erni, and H Jäckel. Fabrication of a hard mask for inp based photonic crystals: increasing the plasma-etch selectivity of poly (methyl methacrylate) versus sio2 and sinx. *Journal of Vacuum Science & Technology B: Microelectronics and Nanometer Structures Processing, Measurement, and Phenomena*, 23(6):3197–3201, 2005.

[104] E Selfors. *Fabrication of large free-standing nanostructured zone plates for focusing a Bose Einstein condensate*, Master Thesis, University of Bergen, 2017.

Grafisk design: Kommunikasjonsavdelingen, UiB / Trykk: Skipnes Kommunikasjon AS

uib.no

ISBN: 978-82-308-3686-6